8-1-2022

Clay Beds Preserved in High-Energy Gravel Deposits on Crowley's Ridge, Northeastern Arkansas, U.S.A.--Origin and Significance from a Lithofacies and Mineralogical Perspective

Trevor John Dempsey

Recommended Citation

Dempsey, Trevor John, "Clay Beds Preserved in High-Energy Gravel Deposits on Crowley's Ridge, Northeastern Arkansas, U.S.A.--Origin and Significance from a Lithofacies and Mineralogical Perspective" (2022). *Electronic Theses and Dissertations*. 2366.
https://egrove.olemiss.edu/etd/2366

CLAY BEDS PRESERVED IN HIGH-ENERGY GRAVEL DEPOSITS ON CROWLEY'S RIDGE, NORTHEASTERN ARKANSAS, U.S.A.—ORIGIN AND SIGNIFICANCE FROM A LITHOFACIES AND MINERALOGICAL PERSPECTIVE

A Thesis
presented in partial fulfillment of requirements
for the degree of Master of Engineering
in the Department of Geology and Geologic Engineering
The University of Mississippi

By
TREVOR J. DEMPSEY
August 2022

Abstract

The Upland Complex (UC) on the southern half of Crowley's Ridge in Northeastern Arkansas is a 2.6 to 0.2 Ma high-energy, braided sand and gravel containing two thin zones of clay preserved near the top of the UC. Minimum age of the clay was acquired from overlying Brown and Foreman (2012) thermoluminescence ages and maximum age was acquired from Odom et al. (2019) Al/Be age of the basal UC. This project aims to discern if these clay layers formed from pyroclastic material and if so, what the provenance of the parent material is. The investigation of the clay layers included a lithofacies analyses coupled with X-ray diffraction (XRD) and Scanning Electron Microscopy-Energy Dispersive X-ray spectroscopy (SEM-EDS). SEM-EDS analysis of the clay identified igneous minerals such as sanidine, volcanic glass, albite, leucite, and pumice grains. XRD analysis indicated that kaolinite content in the gravels and sands was higher than in the clay, which is interpreted as an in-situ weathering product. This is in contrast to the clay rich layers which are dominated by illite-smectite, indicating an igneous origin. The presence of igneous components and the occurrence of montmorillonite and altered volcanic glass indicates the clay has a pyroclastic origin. Igneous components identified in SEM-EDS were not limited to clay layers, but were also present in the clay fraction of sands and gravels.

The lithofacies analysis identified nine lithofacies organized into four architectural elements. The gravel and sand lithofacies were organized into gravel bars and bedform architectural elements interpreted as braided ancestral Mississippi River deposits. Clay layers were assigned an abandoned channel architectural element and interpreted as abandoned barchute deposits. In this instance, ash fall layers were deposited in a high energy fresh water environment and then altered into smectite. The alteration of smectite to illite-smectite likely occurred through K-fixation induced by repetitive wetting and drying cycles.

Potential sources of the igneous material include the Valles Caldera, Yellowstone Caldera, Acoculco Caldera, and Long Valley Caldera, however the Yellowstone eruptions seem most probable because of their explosive and voluminous eruptions.

List of Abbreviations

1. Lithofacies Analysis – LA
2. X-Ray Diffraction — XRD
3. Scanning Electron Microscopy-Energy Dispersive X-ray spectroscopy — SEM-EDS
4. Upland Complex — UC
5. Crowley’s Ridge — CR
6. Mississippi Embayment — MSE
7. Mississippi Valley Graben – MVG
8. Texas Tech University – TTU
9. Air-dried — AD
10. Ethlyene glycol — EG
11. Energy Dispersive Spectrometer — EDS
12. Kaolinite – Kln
13. Quartz – Qtz
14. K-feldspar – Kfs
15. Bishop Tuff — BT
16. Lava Creek Tuff — LCT
17. Huckleberry Ridge Tuff – HRT
18. Mesa Falls Tuff — MFT

Acknowledgments

I would like to acknowledge the many contributors to this project without who this endeavor would not be possible. In alphabetical order I would like to thank:

The Arkansas Geologic Survey, for funding and help with this project. I would especially like to thank Scott Ausbrook and Bill prior for their help in the field and correspondence.

Dr. Branimir Šegvić from Texas Tech who was a critical part of this project, allowing me to use his labs as well as the guidance and instruction given that made this project possible. I also greatly appreciate the countless revisions made to every section as well as the input and feedback given that enhanced the overall quality of the paper as a whole.

The Clay Mineral Society for the funding that made this entire project possible. The funding from CMS provided help with materials, travel, lodging, and analytical methods.

Doctoral candidate Luka Badurina from Texas Tech, for all of the lab work and time put into helping me in the lab and analyzing my samples. As well as instructing me and aidint me in the creation of figures and graphs.

The Arkansas Geologic Survey, for funding and help with this project. I would especially like to thank Scott Ausbrook and Bill prior for their help in the field and correspondence

Mississippi Mineral Resource Institute for funding provided for lodging and travel done in completing field work. I would especially like to mention Dr. Gregg Easson for his guidance and Jaclyn Montoria for all the help with paperwork and logistics.

I would like to thank my advisor Dr. Ron Counts for help in the field and academic guidance in pushing me to get the funding and support for this thesis and his introduction to Dr. Warren Huff whoes guidance shaped the outcome of this project.

Table of Contents

List of Tables

List of Figures

Chapter 1

Introduction

Crowley's Ridge (CR) is a topographic ridge within the northern Mississippi River Valley of northeastern Arkansas and southern Missouri (Figure 1). The clay rich horizons were found in numerous gravel and sand layers known as the Upland Complex (UC) a ~3.0 Ma ancestral Mississippi River alluvium found on Crowley's Ridge (Odom et al., 2020). The clay layers were discovered by my advisor Dr. Ron Counts while conducting research on the UC in Crowley's Ridge. These gravels typically represent high energy environments and clays indicate low-energy settings, the close association between these two lithofacies prompted a reevaluation of the UC system.

An investigation of these clay rich horizons was conducted at Drum Pit in the southern portion of CR, ~25 km south of Jonesboro and ~6 km north of Harrisburg (Figure 2). This study builds on a preliminary X-ray diffraction (XRD) analysis of the clay, performed at the University of Cincinnati, which revealed that the clay included smectite (Warren Huff, personal communication), a clay mineral that has the potential to form from the alteration of pyroclastic material (Southard & Miller 1966; Denton et al., 2009; Huff, 2016; Badurina et al., 2021).

This reseach tests the hypothesis that the clay-rich layers present in the Drum pit formed from the weathering of pyroclastic material that accumulated in a fluvial system and was later deposited in an abandoned channel. The objective of this project is to use lithofacies analysis (LA) to investigate the depositional environments and the mechanisms that transported the clay.

In addition to LA and XRD, Scanning Electron Microscopy-Energy Dispersive X-ray spectroscopy (SEM-EDS) was utilized to study the global and clay fraction mineralogy, and phase chemistry in order to determine clay mineralogy, microtexture and likely provenance.

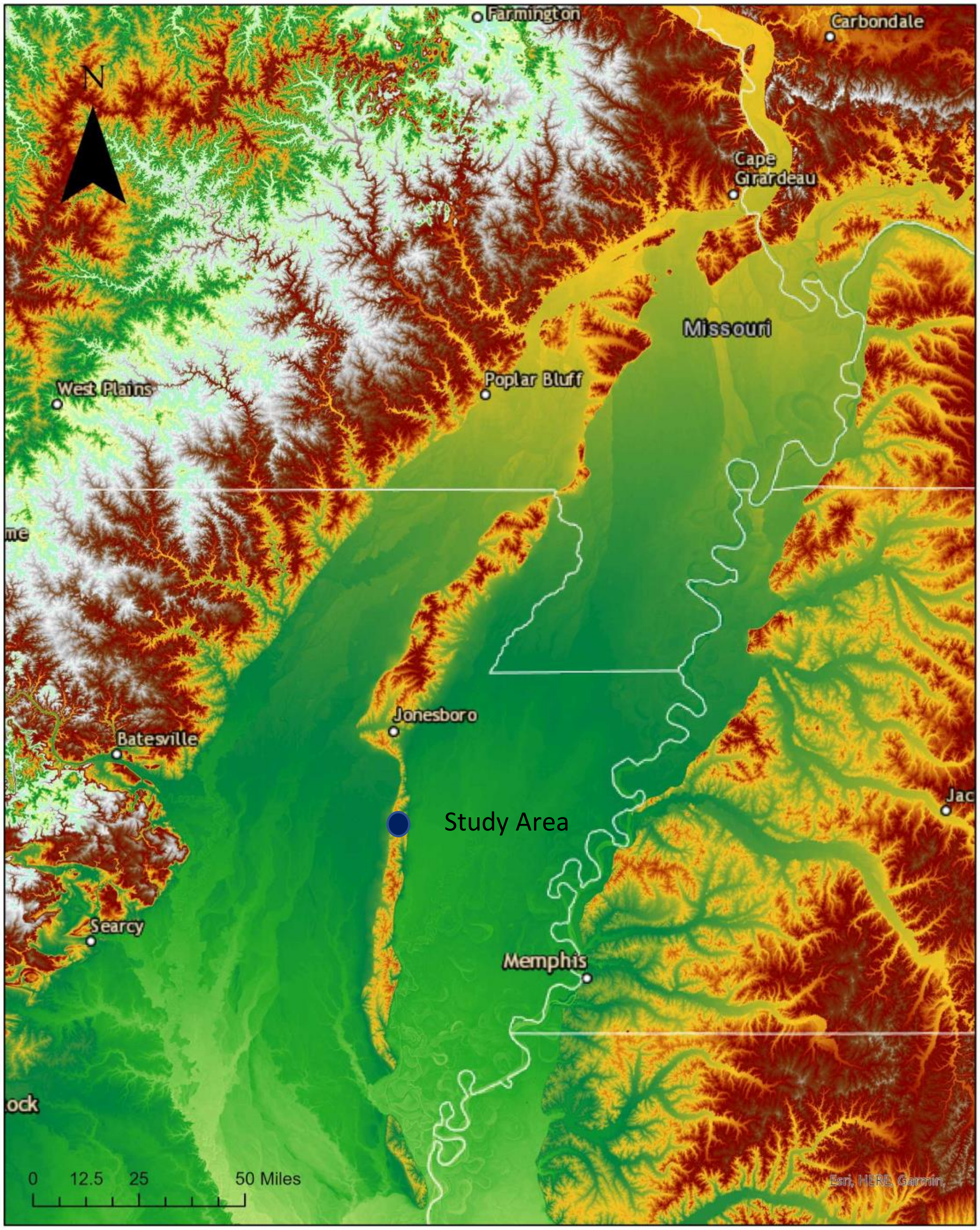

Figure 1. Digital Elevation Model of Crowley's Ridge. White line is the modern Mississippi River Channel. The blue dot is the study area.

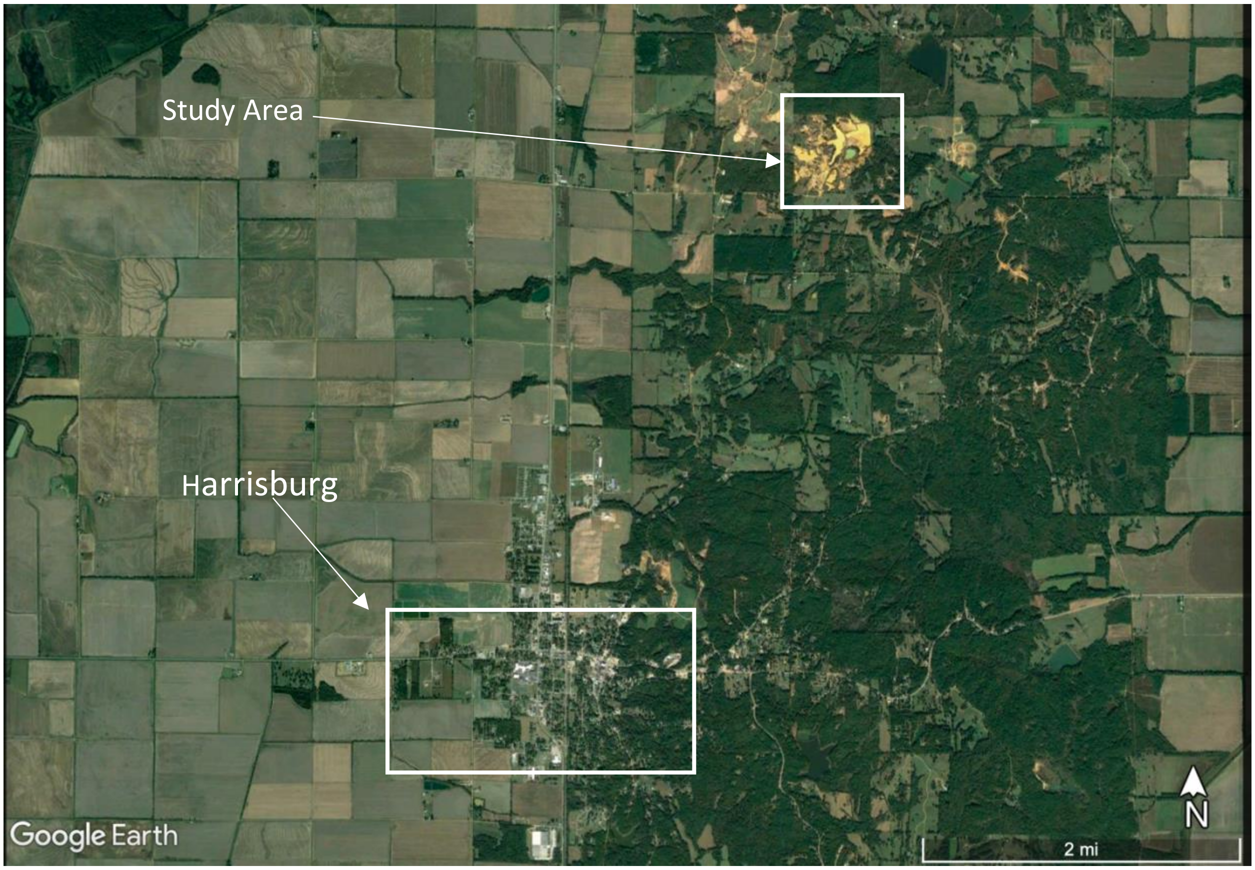

Figure 2. Study Area relative to Harrisburg, AR.

Chapter 2

Geologic Background

2.1 Mississippi Embayment

2.1.1 Formation of the Mississippi Embayment

The Mississippi Embayment (MSE) is a structural trough extending northward along the axis of the Mississippi River from the Gulf of Mexico into southern Illinois (Dockery & Thompson, 2016) (Figure 3). The MSE is a Late Cretaceous and early Tertiary sedimentary basin that forms a northward excursion of the Gulf of Mexico and is an extension of the coastal plain (Stearns, 1957). This feature became an active basin in the Late Cretaceous and early Paleocene and is a part of the larger Gulf of Mexico Basin Region (Dockery & Thompson, 2016).

The MSE lies within the failed arm of a late Precambrian triple junction associated with rifting and the opening of the Gulf of Mexico (Burke & Dewey, 1973; Ervin & McGinnis, 1975; Stein et al., 2022). Geophysical research using seismic refraction (Mooney *et al.,* 1983) reinforced the idea that the MSE is the site of a Late Precambrian continental rift that was reactivated in the Mesozoic. The seismic refraction survey revealed that the crust of the MSE includes two layers that represent departures from the standard continental crust and suggest sediment was deposited in the graben after rifting, and the lower crust has been altered by injection of mantle material (Mooney et al., 1983).

The exact mechanisms that caused the failed rifting beneath the MSE debated. The first theory attributes the formation of the MSE to isostatic disequilibrium due to the intrusion of high-density rocks, prompting renewed subsidence (Ervin & McGinnis, 1975). A second theory hypothesizes that the MSE formed from the Mississippi Valley graben (MVG) passing over the Bermuda hotspot ~90 Ma (Braile et al., 1986; Cox & Van Arsdale, 1997). The graben was perturbed by passage over the Bermuda hotspot, which caused uplift of the fault blocks, and intrusion of magma along fault planes and decreased lithospheric strength (Cox & Van Arsdale, 1997). Following the thermal doming from passage of rifted crust over a mantle hotspot, subsidence and erosion of the graben ensued (Cox & Van Arsdale, 2002).

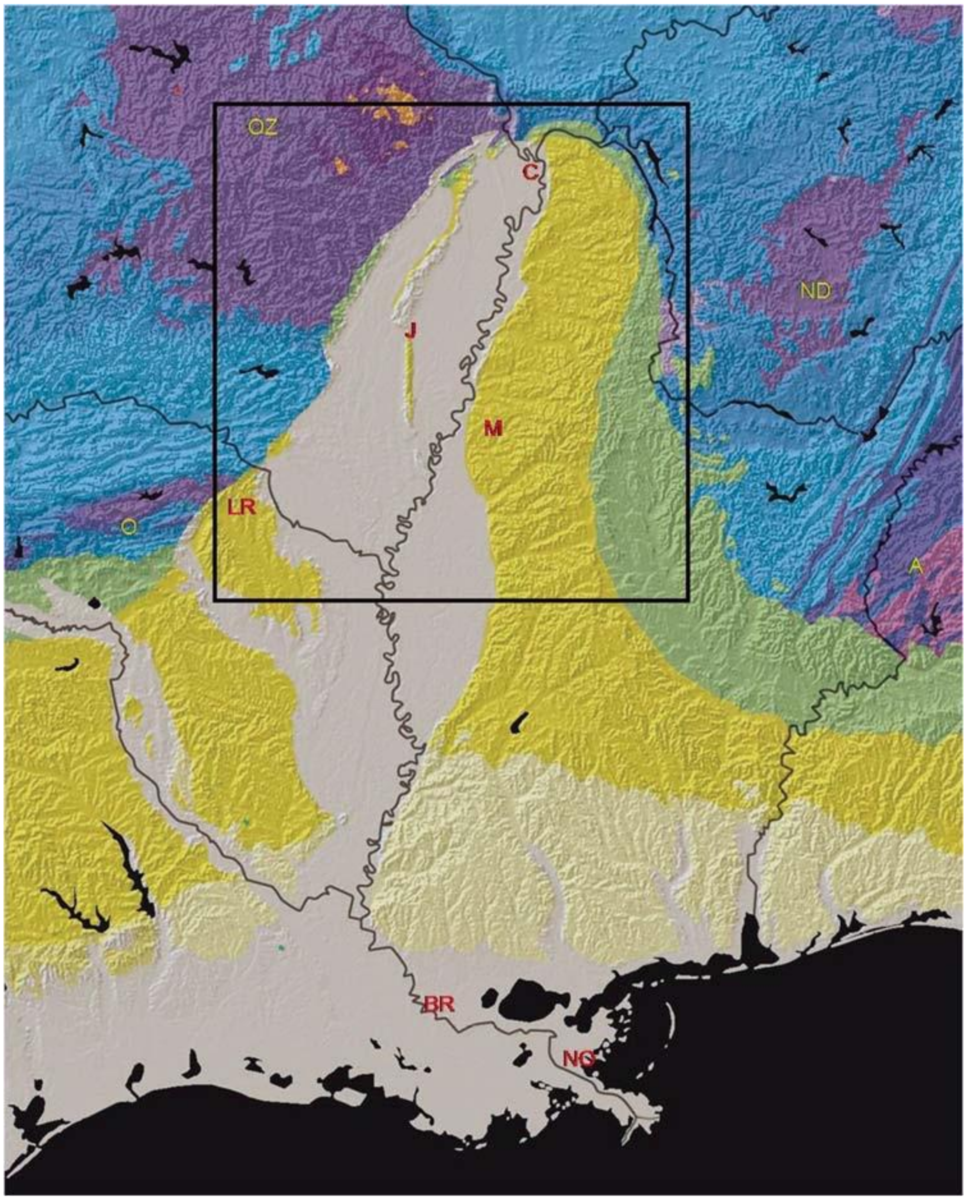

Figure 3. DEM of the Mississippi Embayment (R. Van Arsdale, 2009). The Mississippi Embayment in green and yellow; Mississippi River Valley in gray. C— Cairo, Illinois; M—Memphis, Tennessee; BR—Baton Rouge, Louisiana; OZ—Ozark Mountains; A—Appalachian Mountains; O—Ouachita Mountains; LR—Little Rock, Arkansas; NO—New Orleans, Louisiana; ND—Nashville dome (modified from the U.S. Geological Survey). Central Mississippi River Valley is shown in box. Crowley's Ridge is the topographic high region in the upper MSE.

2.1.2 Geology of the Northern Embayment

Subsurface data suggest that the northern MSE Cretaceous, Paleocene, and lower Eocene deposition started with the deposition of the Cretaceous nonmarine Tuscaloosa formation (Stearns, 1957). Marine advance and depositional limits reached a maximum in the Paleocene with the deposition of the Porters Creek Clay, which once generally extended beyond the MSE limit (Cushing et al., 1964).

The entire MSE is underlain by igneous rocks that form the synclinal structure of the MSE, that are Paleozoic in age (Cushing et al., 1964). Cretaceous deposits rest unconformably on Paleozoic bedrock throughout the MSE except in the extreme southern part, where Lower Cretaceous deposits overlie truncated Jurassic strata (Stearns, 1957).

Paleocene Midway Group strata underlie the Eocene and overlie the Upper Cretaceous strata (Stearns, 1957). The Paleocene strata is composed of nearly 300 m of predominantly dark clay (Stearns, 1957, Autin et al., 1991). The Midway Group constitutes the entire Paleocene Series except in northern Louisiana, where the lower part of the Wilcox Group is included (Stearns, 1957).

Eocene sediments crop out or underlie about 70 % of the MSE and are thickest in the southeastern part of the region, where marine sediment provide a basis for unit differentiation (Stearns, 1957). The Eocene rocks are divided, in ascending order, into the Wilcox Group, Claiborne Group, and Jackson Group .

Quaternary deposits unconformably overlie Eocene sediments and cover much of the Coastal Plain surface, including Pleistocene and Holocene sands, gravels, and clays from alluvial floodplain surfaces and terraces (Stearns, 1957). Loess covers much of the area east of the Mississippi River alluvial plain and caps CR (West et al., 1980).

2.2 Crowley’s Ridge

2.2.1 Modern Geomorphology

CR is a topographic ridge located in Eastern Arkansas (AR) and Southeast Missouri (MO). CR is 18 km wide at its widest, and extends ~320 km from Helena, AR to Thebes, Illinois (IL), dividing the northern MSE into the Eastern and Western lowlands (Jobe et al., 2020 Figure 1). The ridge stands 30 to 60 m higher than the adjoining Eastern and Western Lowlands (Guccione et al., 1986) and the northern third of the ridge is generally steeper on its western margin, indicating an overall eastward tilt of the topography (Cox, 1988). Geomorphic analysis indicates CR is composed of three fault-bounded blocks, each 5–10 km wide (Boyd & Schumm, 1995).

CR can be divided into three distinct geomorphological regions; northern CR, central CR, and southern CR, all defined by their own distinct differences in landscapes, elevation and tilt. These distinctions include erosional and tectonic features that have shaped the morphology of the ridge (Jobe et al., 2020).

2.2.2 Formation of Crowley’s Ridge

Earlier research on CR interpreted the ridge to be an erosional remnant created by incision of an ancient alluvial surface by the paleo-Mississippi and paleo-Ohio Rivers, with the ancestral Mississippi River flowing on the western side of CR and the ancestral Ohio River on the eastern side of CR (Guccione et al., 1986; Van Arsdale et al., 1995). Later research found that CR is also fault bounded (Van Arsdale et al., 1995) and that the northern part is still seismically active (Baldwin et al., 2006). More recent research, however has inferred CR to be a tectonic landform bounded by active Quaternary faults (Jobe et al., 2020).

2.2.3 Geology of Crowley's Ridge

CR consists of Paleocene to Oligocene basin fill sediment overlain by Pleistocene and Pliocene sediment (Hayward et al., 1988). The Wilcox Group is the oldest unit ranging from Paleocene to Eocene and is ~236 m thick at the southern edge of the ridge and consists of interbedded sand, silt, clay, and some lignite, all deposited in a fluvial deltaic environment (Meissner, 1984).

The Eocene Claiborne Group overlies the Wilcox and is exposed along flanks of the ridge (Guccione et al., 1986). The Claiborne sediments consist of fine sand, silt, sandy clays, and some minor lignite, all deposited in deltaic and nearshore marine environments (Meissner, 1984)

The Jackson Group overlies the Claiborne Group and is exposed in the southernmost portion of CR. Here, the sediments are approximately 150 m thick and consist of sandy clay, silt, and glauconitic, fossiliferous sandy clay deposited in a nearshore marine environment (Stearns, 1957). The Jackson Group was deposited during the last marine transgression and outcrops throughout the ridge, but this group is often not present in the southern part of the ridge (Wilbert, 1953).

The sand and gravel unit known as the Upland Complex (UC) overlies the Jackson Group on CR and varies in thickness from 0 to 38 m. In outcrops, the UC is continuous for hundreds of meters laterally. The texture of the sand and gravel is coarse, poorly sorted, and subrounded. In gravel beds, sub-rounded and imbricated clasts are granule to pebble in size, commonly with a medium to coarse sand matrix. The Pliocene UC gravels exposed on the ridge are interpreted as being deposited dominantly in braided streams and coarse-grained meandering stream environments (Hayward et al., 1988). The gravel has also been interpreted to represent the depositional environment of a floodplain (Guccione et al., 1986).

The Pliocene strata are capped by multiple Pleistocene loess sheets. The loess has a reported thickness of up to 43 m on the southern portion of the ridge (West et al., 1980). The loess on the northern parts of the ridge is noticeably thin to nonexistent in some outcrops (Guccione et al., 1986).

2.3 The Upland Complex

2.3.1 Petrology of the Upland Complex

Early research defined the UC as a layer that represented a fluvial deposit that is discontinuously preserved on drainage divides from western Kentucky (KY) to Louisiana (LA) along the eastern side of the Mississippi River valley and on CR from southern IL into eastern AR (Potter, 1955). The mineralogy and petrology of early investigations defined the UC as coarse grained gravels and sands. (Potter, 1955; Autin, 1996).

Lumsden et al. (2016) did a an analysis of the UC, sampling 18 exposures in TN, KY, MS, MO, and IL Optical petrography, grain size analysis, heavy mineral analysis, and X-ray diffraction were used to investigate the petrology of the gravel. Lumsden et al. (2016) reported that the UC consisted of massive bedded, well rounded chert pebble gravel and coarse quartz sand. Gravel clasts were almost entirely chert with some polycrystalline quartzite (<5%) (Lumsden et al., 2016).

Sand textures included abundant, sharply angular, limpid, deeply embayed grains of monocrystalline and polycrystalline quartz, and continuous quartz overgrowths were observed on dust rims of monocrystalline quartz grains and grains of fine sandstone (Lumsden et al., 2016). Grains also exhibit polycrystalline texture with complex sutured contacts among crystallites. Abundant angular and unaltered feldspar (both K-feldspar and plagioclase) in CR samples were also observed (Lumsden et al., 2016).

There are several inferred depostional environments for the UC. One is that it is a meandering stream deposit, inferred from the presence of large relict meanders preserved in the UC (Cox et al., 2014). While another interpretation has suggested the UC was a braided stream deposit based off petrological analysis and sedimentary structures (Lumsden et al., 2016).

2.4 Loess on Crowley's Ridge

2.4.1 Deposition of Loess

Loess is terrestrial clastic sediment, composed predominantly of silt-sized particles, and essentially thick accumulations of wind-blown dust (Pye, 1995). Extensive loess-paleosol pairings on CR record the cyclical transitions between stable landscape conditions during interglacial periods with pedogenesis, and rapid loess accumulation during glacial periods (Brown & Forman, 2012).

Loess units on the ridge, from the oldest to youngest include: Marianna silt, Crowley's Ridge loess, Loveland loess, Roxana silt, and Peoria loess (Rutledge st al., 1996; Markewich et al. 2011; Brown & Forman, 2012; Figure 4). The upper parts of four of the units have been pedogenically modified (Crowley's Ridge loess, Loveland loess, Roxana silt, and Peoria loess) (Rutledge et al., 1996).

2.4.2 Ages of the Loess Units

Research on the ages of Mississippi Valley loess has been extensive, but many of the different methods applied to dating the loess have yielded different results. One of the oldest suspected ages of the loess deposits is the Crowley's Ridge loess (Figure 5), which has ages of >~159-274 ka (Forman & Pierson, 2002). The Teneriffe Silt, a supposed correlative deposit of the Loveland loess, yielded younger thermoluminescence ages of ~70-100 ka (Maat & Johnson, 1996; Forman & Pierson, 2002). Overlying Crowley's Ridge loess is the Loveland loess (Figure

5) which was deposited during the Illinoian Glaciation (Rutledge et al., 1996; Grimley, 2003). The Loveland loess (Figure 5) has luminescence ages ranging from ~ 110-180 ka (Forman & Pierson, 2002; Maat & Johnson, 1996). The Sangamon geosol is formed on the Loveland loess and seperates it from the overlying Roxana silt (Muhs & Bettis, 2000; Forman & Pierson, 2002; Grimley, 2003). The Roxana silt was deposited ~30-55 ka (Brown & Forman, 2012) and is seperated from the overlying Peoria loess by the Farmdale geosol (West et al., 1980). The youngest loess deposit is the Peoria loess (Figure 5), deposited during the last glacial advance, with ages that range from ~12-25 ka (Brown & Forman, 2012).

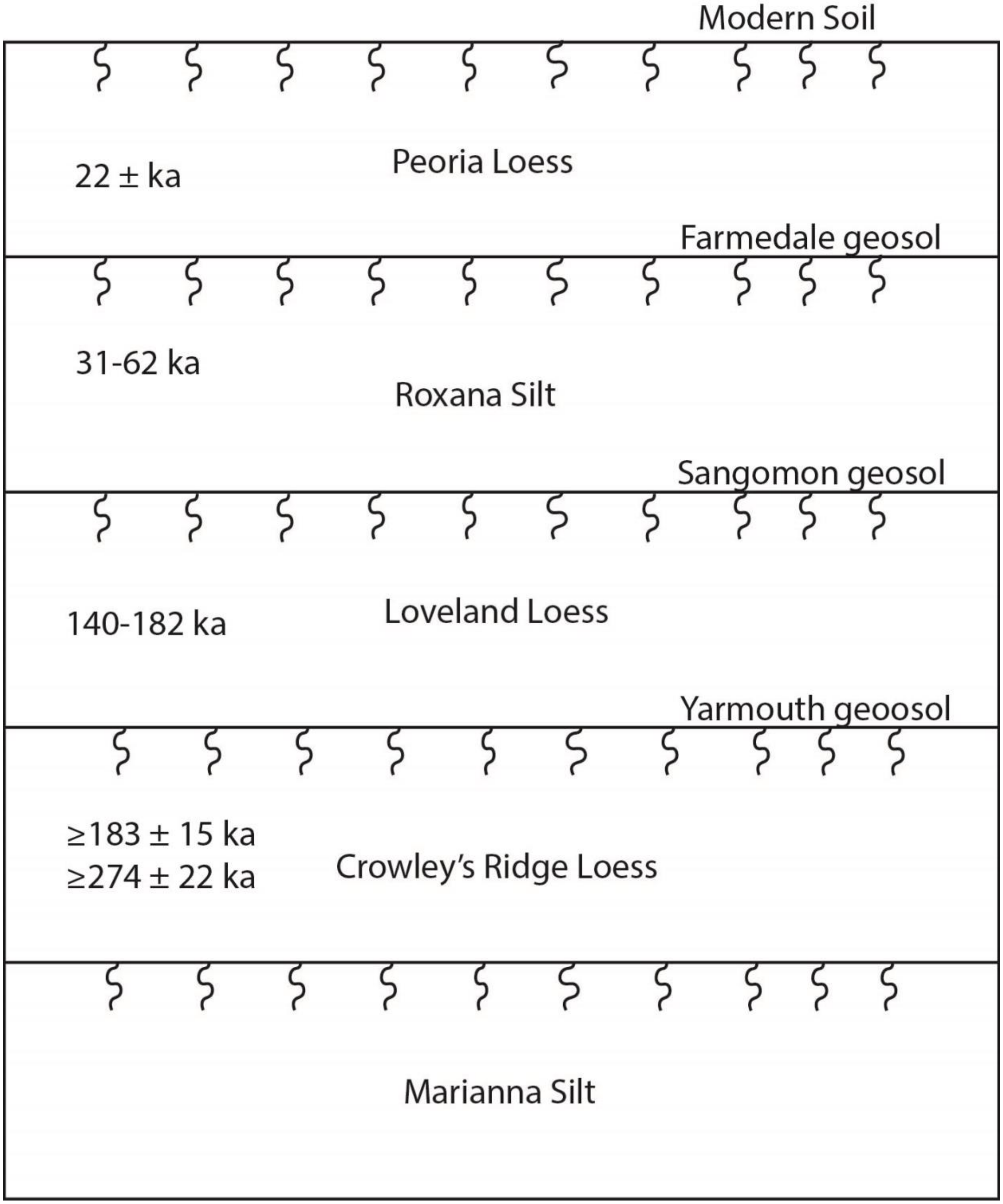

Figure 4 Drum pit loess stratigraphy, and ages from Brown and Forman (2012)

2.5 Study Area

2.5.1 Location of Study Area

The study area is located in a private gravel mining pit owned by Jeff Drum and is 30 km south of Jonesboro and 5.6 km northeast of Harrisburg, off Highway one (35°36'33.75"N, 90°41'27.32"W). The pit is referred to as Drum pit and is accessible via a dirt road from the west side of the ridge on Massengill Road past Bolivar cemetery (Figure 5). The outcrop of interest for this study is located on the eastern most boundary of the pit.

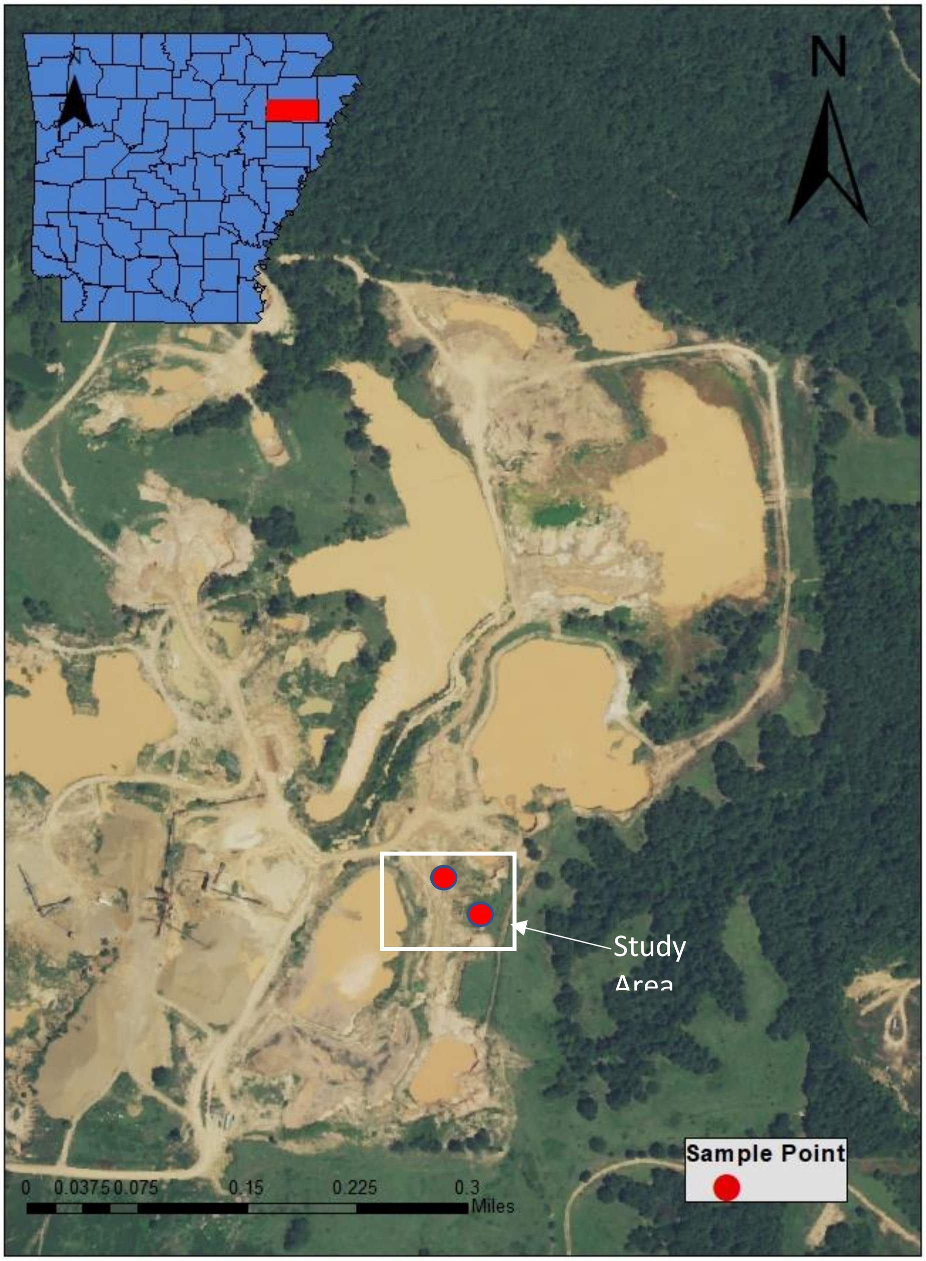

Figure 5 Satellite Imagery and locations of outcrops in Drum pit. The eastern and western outcrop are labeled with red dots.

Chapter 3

Materials and Methods

3.1 Sample Collection

Samples were collected from two exposures within Drum Pit in Poinsett County, Arkansas with permission from the owner, Jeff Drum. The two outcrops were separated by ~10 m in distance from each other. Detailed field notes and descriptions were recorded in the field. Color was documented with the use of a Munsell color chart, and measured sections of both outcrops were created in the field. At the western outcrop and eastern outcrop samples were collected from different horizons defined by changes in lithology, grain size, matrix fabric, and sedimentary structures and geometry (Figures 6 and 7). Samples were collected with spades, and shovels. Samples were collected and put in brown film bags. The bags had a volume comparable to a liter and each was filled to capacity (Table 1)

Table 1. Overview and general information on analyzed clay samples

Sample	Outcrop	Height (m)	Stratigraphy	Texture	Color	Thickness (m)	Applied methods
E8	East	1.95	clay rich layer	Fine grained	Gray (10YR 7/1)	0.2	XRD, SEM-EDS, ICP-MS
E7	East	1.75	Crossbedded sand layer	Coarse grained	Yellow (2.5YR 5/8)	0.4	XRD, SEM-EDS
E5	East	1.35	Clay rich layer	Fine grained	Gray (10YR 7/1)	0.1	XRD, SEM-EDS, ICP-MS
E4	East	1.25	Nodular Clay laminae	Fine grained	Yellow (10YR 6/2)	0.05	XRD, SEM-EDS, ICP-MS
E3	East	1.2	Unconsolidated gravel and sand layer	Pebbles	Yellow (10YR 3/4)	0.5	XRD, SEM-EDS, ICP-MS
E2	East	0.75	Sand lens	Coarse grained	Yellow (10 YR 6/6)	0.15	XRD, SEM-EDS, ICP-MS
E1	East	0.6	Unconsolidated gravel and sand layer	Pebbles	Yellow (2.5YR 3/4)	0.6	ICP-MS
W2	West	3.21	clay rich layer	Fine grained	Gray (10YR 7/1)	0.25	XRD, SEM-EDS, ICP-MS
W1	West	4.29	clay rich layer	Fine grained	Gray (10YR 7/1)	0.17	XRD, SEM-EDS, ICP-MS

Munsell Color chart abbreviations YR = Yellow Red. Applied Methods: X-ray diffraction (XRD), Scanning Electron Microscopy-Energy Dispersive X-Ray Spectroscopy (SEM-EDS), ICP-MS

Figure 6 Western outcrop sample location

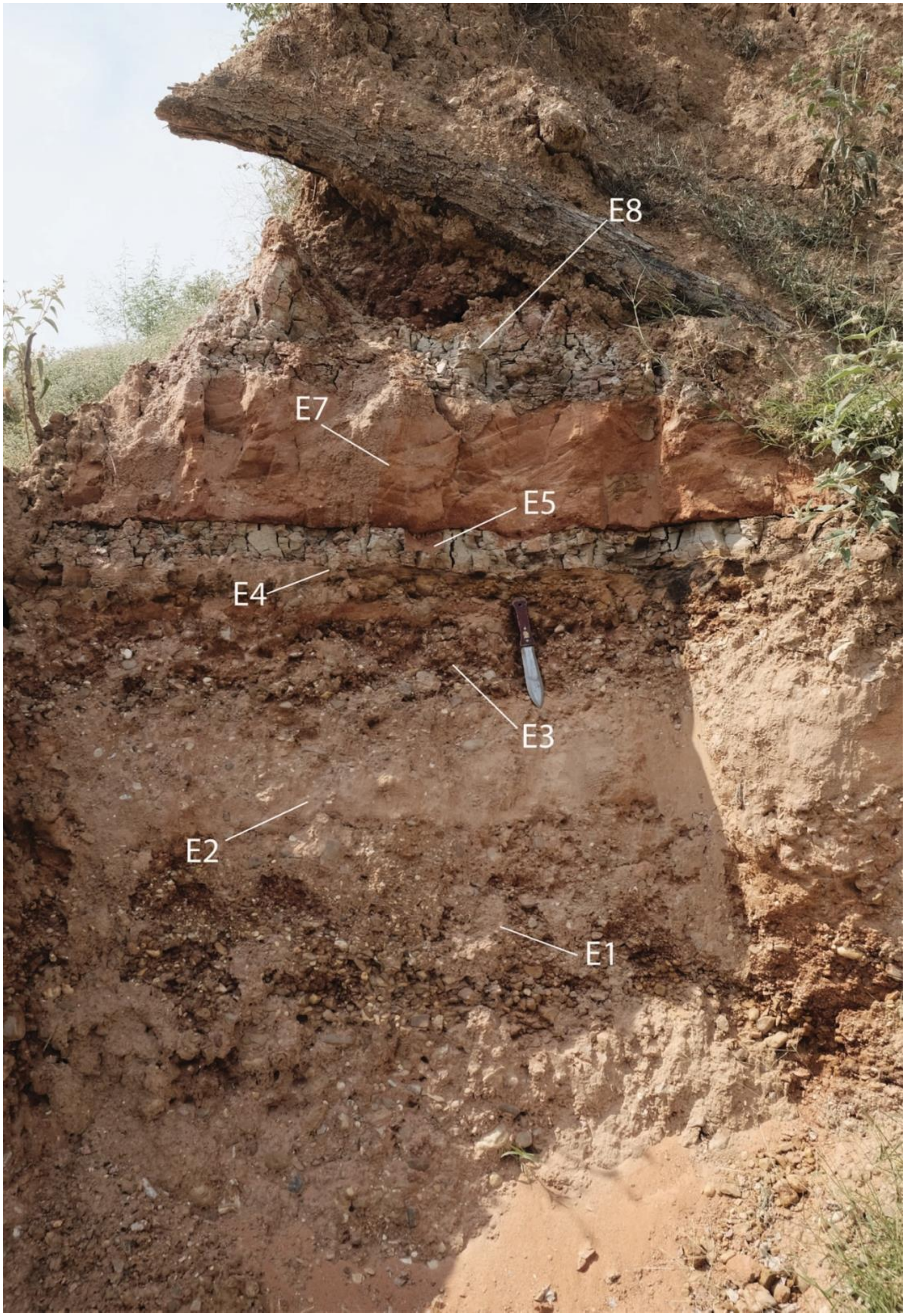

Figure 7 Eastern outcrop sample locations

3.2 Lithofacies Analysis

The eastern and western outcrops were photographed using a digital single lens reflex camera at ground level in Drum Pit. Outcrop descriptions, detailed field notes, and measured stratigraphic sections are the basis for classification of lithofacies and the assessment of stratigraphic architecture. Architectural elements were separated using a classification system dependent on sediment composition, sediment body geometry and relationships, and sedimentary structures (Miall, 2013).

3.3 X-Ray Powder Diffraction and Interpretation

X-ray powder diffraction was performed on the global sample and clay fraction for samples E2, E3, E4, E5, E7, and E8. For samples W1 and W2, however, just the global sample was measured. Sample preparation initially included sieving with the 63 μm sieve before powdering with an agate mortar and pestle prior to whole rock XRD measurements. The clay fraction was separated according to Moore and Reynolds (1997) and Zanoni et al. (2016), which included sonication and centrifugation. Oriented mounts were prepared by pipetting the suspension made from centrifugation was then put on glass slides and left to dry at room temperature overnight. The thickness of the prepared mounts exceeded 50 μm, which is required for semi-quantitative determination of the clay mineral content (Moore and Reynolds, 1997). The measurements were taken in air-dried (AD) conditions and after ethylene-glycol (EG) saturation at the Geosciences Clay Laboratory of Texas Tech University (TTU) using a Bruker D8 Advance diffractometer. Measurement parameters consisted of 1 mm divergent and receiving slits with a step scan in Bragg- Brentano geometry which uses a CuKα radiation (45 kV and 40 mA). Sample mounts were scanned at a counting time of 1.8 s per 0.02°2Θ from 3 to 70 and from 3 to 30 °2Θ for the whole rock and the clay fraction, respectively.

XRD pattern interpretation was conducted using Bruker EVA software and the PDF4+ database published by the International Centre for Diffraction Data. Qualitative identification was determined by searching for mineral phases with corresponding peaks in a diffractogram. Selection occurred by pairing specific mineral phases from the PDF4+ database to the strongest peaks in a diffractogram. Mineral phases were confirmed by looking at weaker peaks in a diffraction pattern and comparing their positions to the suggested mineral. Each mineral selected in a diffraction pattern would eliminate its associated peaks from further consideration. This process was repeated until all the peaks had a mineral phase associated to them.

3.4 Modeling and Qualitative Description of Clay Minerals

X-ray diffraction patterns of clays from sample E5 were modelled using the Sybilla$^{©}$ software (Chevron™), which is based on mathematical formalism provided by Drits and Sakharov (1976). Sybilla$^{©}$ modelling was used to reveal the nature of mixed-layer clay minerals reported in the sample E5. Sample E5 was used because it was a representative sample of the illite-smectite rich clay layer. Modelling first included a trial-and-error procedure that yielded optimal clay mineral structural and probability parameters, which enabled the best fit to be obtained between experimental and calculated positions and intensities of basal reflections for each mineral present in the sample. Once the parameters of all the modelled phases had been set, the content of each phase could be adjusted to match the original pattern as far as possible. To produce the modelled E5 pattern two discrete phases were introduced (illite, and kaolinite) and two mixed-layer minerals (R0 I-S-S and R1 I-S-S).

3.5 Scanning Electron Microscopy-Energy Dispersive X-Ray Spectroscopy

SEM analyses were carried out by means of a Zeiss Crossbeam 540 apparatus equipped with an energy-dispersive spectrometer (EDS) at the Texas Tech Microscopy Center of the

College of Arts and Sciences. Carbon-coated thin sections of samples W1 and W2, in addition to carbon-coated powders from samples E2, E3, E4, E5, E7, and E8 were used for this investigation. The measurements were performed at high vacuum, 15 kV and ~1 nA, with two silicon drift energy dispersive X-ray detectors from Oxford Instruments. High-resolution back-scatter electron images have been acquired using a 4-quadrant-backscatter detector. EDS analyses were performed on spots with a diameter of at least 100 nm and an acquisition live time of 20 s. The Zeiss AZtec software (Oxford Instruments, Oxford, UK) was used for EDS spectra quantification in a standardless mode. Chemical data were used as oxide percentages and were normalized to 100%.

Chapter 4

Results

4.1 Geology of the Study Area

The study area is an open mining pit that mines the UC gravel in the ridge for construction and building applications (Behrman et al., 2019). Three units are present in the study area, they include from bottom to top: the Eocene Claiborne Group, and the Quaternary UC, and Quaternary loess (Figure 8). Within the UC are the clay layers which are the primary interest of this project. There are two distinct bands of clay in the gravel that are parallel to each other and separated by crossbedded sand. The two clay layers are 10-15 cm thick and have sharp upper and lower contacts. The layers are gray when fresh but yellow and orange if it has not rained or if the exposure is not a fresh cut (Table 1).

This project examined two outcrops in Drum pit, a western outcrop and an eastern outcrop, separated by a couple dozen meters in distance. Both outcrops are very similar, but show some distinct differences stratigraphically.

The western outcrop (Figure 6) is stratigraphically composed of crossbedded sands and gravels 3 m thick. Overlying the gravels and sands is the first primary clay rich layer, which is 10-12 cm in thickness with a sharp bottom and top contact. Overlying the clay rich horizon is a coarse grained crossbedded sand layer a little over half a meter in thickness. Above the crossbedded sand is the second clay rich layer with a sharp bottom and top contact. A coarse-grained sand and gravel layer overlies this clay layer. The eastern outcrop (Figure 7) has a basal gravel and sand layer that is overlain by a clay rich layer. The clay layer has a nodular clay layer beneath it with some limonite. The clay boundaries are not as planar as the west outcrop and have undulating top and bottom contacts. Overlying the clay rich horizon is a crossbedded sand. Above this layer is the second clay rich layer, with its upper portion missing. The two clay layers persist throughout out the mining pit. Other similar clay rich layers have been observed throughout the ridge during preliminary research of the UC by my advisor, Dr. Counts. Recent fieldwork revealed however that the clay rich horizons have been extracted or no the outcrop hosting the material no longer exist.

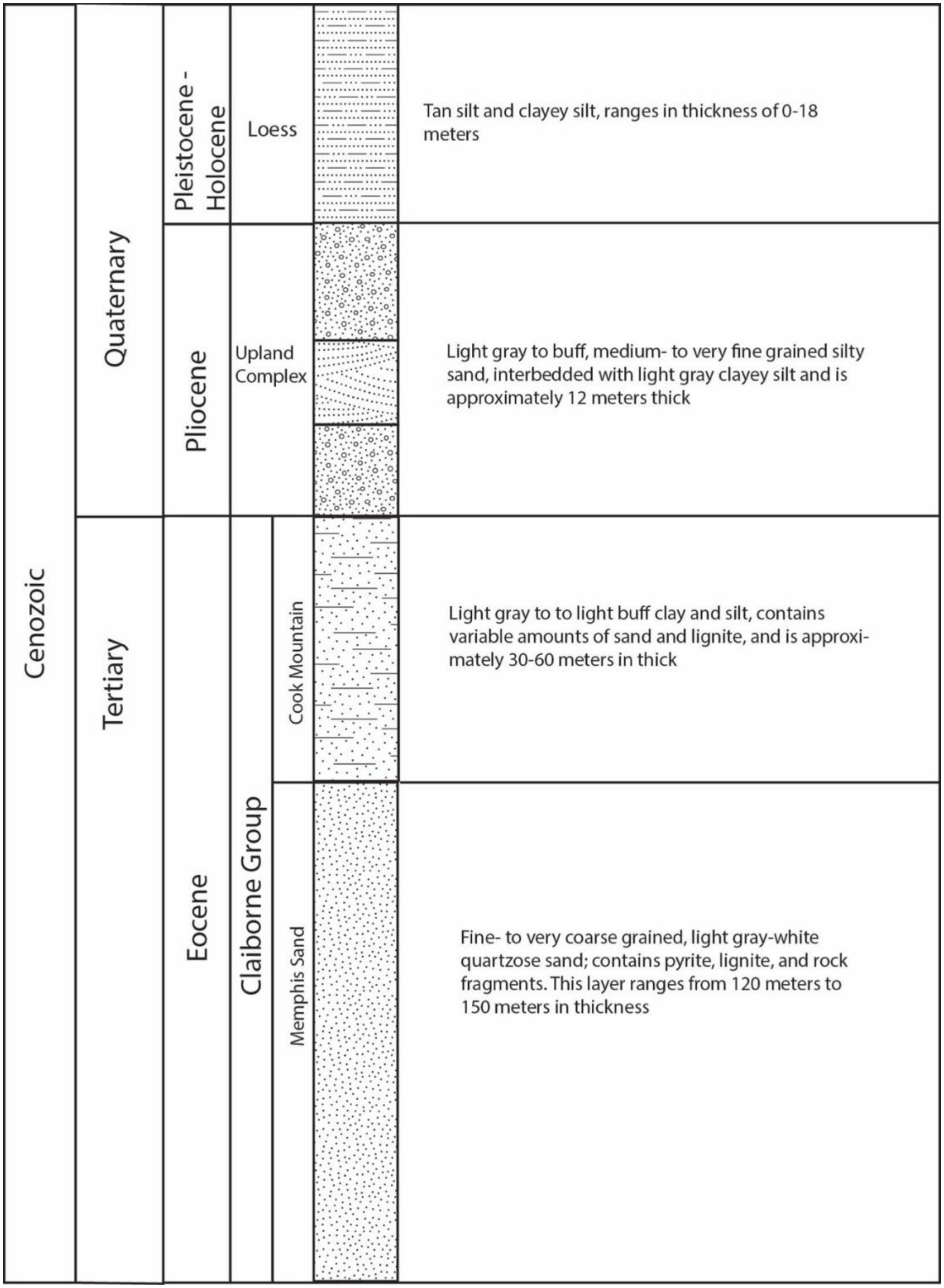

Figure 8 Stratigraphy of Drum pit. The clay layers of interest are located in the UC

4.2 Lithofacies Analysis

4.1.1 Lithofacies

Clast supported massive gravel (Gcm) lithofacies

This is a clast supported, massive to poorly bedded gravel facies with well-rounded to subrounded pebble and cobble clasts (Table 2). The matrix varies between a sandy and clayey matrix, with some crudely dipping gravel beds. This gravel sheet extends to the east and west outcrop (Figure 9A). This lithofacies is generally interpreted to be either inertial bedload or turbulent flow material (Miall, 2013).

Matrix supported massive gravel (Gmm) lithofacies

This gravel lithofacies is matrix supported, with well-rounded large to very large pebbles, with a clayey and sandy matrix (Table 2). Some of these gravel facies have an apparent dip of less than 30°. The gravel sheet is continuous throughout the eastern and western outcrop (Figures 9A, 10B, and 10C). The Gmm lithofacies represents a high strength or viscous plastic debris flow (Miall, 2013) or a sheetflood deposit (Blair & McPhearson, 1994).

Matrix supported massive gravel (Gmp) lithofacies

This is a matrix supported planar crossbedded gravel lithofacies found only in the west outcrop (Table 2). The facies is characterized by well-rounded, very poorly sorted cobbles to small pebbles with iron and manganese coating. These facies have a very well sorted medium grained sandy matrix (Figure 9B). Lithofacies Gmp may represent longitudinal bedforms, lag deposits or sieve deposits (Miall, 2013).

Clast supported massive gravel (Gcp) lithofacies

This lithofacies is a poorly sorted, well-rounded small pebble to cobble gravel, clast supported deposit (Table 2). The unit has pockets of sandy matrix with planar bedding, and clay coatings on clasts. This facies is continuous throughout the study area but was absent in the eastern outcrop (Figure 9D). This lithofacies may be characterized as a clast rich debris flow, a low strength pseudoplastic debris flow (Miall, 2013), or the basal part of a fining upward succession in a highly concentrated sediment dispersion that is rapidly aggrading (e.g. Maisels, 1993).

Sandy cross laminated (Sh) lithofacies

The Sh lithofacies is a well sorted, coarse-grained sand and is found in both the eastern and western outcrops (Figure 10). The principal feature of this facies is horizontal and occasional cross lamination. This lithofacies is sometimes understood to represent plane-bed flow (critical flow; Miall, 2013).

Sandy bedded (St) lithofacies

This lithofacies is a very well sorted unoxidized white sand found in both the western and eastern outcrop (Table 2). The most characteristic feature of this facies is the crossbedding, and in some parts of the study area includes rizolith casts filled with white unoxidized sand. This facies only appears in the study area between both clay layers and only when both clay layers are present (Figures: 9D, 9E, 10A, 10B, and 10C). The St lithofacies can potentially characterize a lower flow regime (Miall, 2013)

Fine grained laminated (Fl) lithofacies

The Fl lithofacies is a well sorted silty clay to clay rich layer (Table 2). Features in these lithofacies include horizontal laminations and vertical fractures. This lithofacies appears in the eastern outcrop but in some areas will pinch out and then reappear. The upper and lower contact of this facies is always distinct but is sometimes scoured or wavy. This facies is found in both the eastern and western outcrops (Figures: 9B, 9D, 9E, 10A, and 10C). This fine grained lithofacies can be interpreted to represent an overbank, abandoned channel, or waning flood deposit (Miall, 2013).

Fine grained structureless (Fm) lithofacies

This is a well sorted clay rich facies and is found in both the western and eastern outcrop (Table 2). This facies lacks sedimentary structure and is continuous throughout the outcrop and has variable thickness (Figures: 9C, 9D, 9E, and 10C). Lithofacies Fm can characterize an overbank, abandoned channel, or drape deposit (Miall, 2013). This lithofacies commonly occurs within gravelly and sandy braided sediments where they represent deposits from standing pools of water during low stage abandonment (Miall, 2013).

Nodular clay layer (Fn) lithofacies

This unique facies is a nodular clay that only occurs beneath the lowermost clay layer in the eastern outcrop. The nodular clay is brown and well sorted with very thin, and distinct boundaries (10A). The nodules have a similar mineralogy to the clay layer above it and may be a product of clays leeching.

Table 2 Lithofacies Association

Lithofacies	Texture	Sorting	Color (range)	Sedimentary structures, soil structure, and other features	Sedimentary Geometries	Contacts	Occurrence, estimated volumetric abundance (VA; 1 = minimal, 5 = major) and lithofacies associations	Present in the West or East outcrop or both (W=West, E=East)
Gcm	Matrix supported, large to v. large well-rounded pebbles, with a med. to c. grained sand matrix of quartz grain composition.	moderately-poorly sorted	7.5YR 5/6-2.5YR 4/8	Some bedding with apparent dips of 26° and 24°. Occasional fining upward trend.	Sheets that are 25-30 cm thick and extending laterally for tens of meters	Gradational contact above and below	Va = 5	W
Gmm	Matrix supported, large to v. large well-rounded pebbles, with a m. to c. grained sand matrix of quartz grain composition.	v. poorly sorted	2.5YR 6/8		Sheets that are 25-30 cm thick and extending laterally for tens of meters	Gradational contact above and below	Va = 3	W and E

Gmp	Matrix supported, cobble to small pebble gravel	poorly sorted	2.5YR 4/8	Sandy Crossbedding	Sheets that are 10-20 cm in thickness and extend laterally for tens of meters	Gradational contact above and below	Va = 2	W
Gcp	Clast supported, well rounded large cobble to small pebble gravel, with pockets of sand. Very little clay in matrix, however clay that is present is a coating or film on cobbles	poorly sorted	5YR 4/6		Sheets are two meters thick and extend laterally for tens of meters	Gradational contact above and below	Va = 2	W
Sh	C. grained, horizontally laminated oxidized sand.	well sorted	10YR 7/1-2.5Y 8/3- 5YR 6/8	Horizontal and occasional cross lamination.	Lens is 3-5 cm in thickness and extends laterally for tens of meters	Sharp upper and lower contact	Va = 2	W and E
St	Quartz grain sand	well sorted	2.5YR 5/8	Rizolith casts filled with white unoxidized sand	Lens is 20-50 cm in thickness and extends laterally for	Sharp upper and lower contact	Va = 1	W and E

					tens of meters			
Fl	Clay-silty clay	well sorted	10YR 6/2-2.5YR 5/6	Horizontally laminated, with vertical cracks	Lens is 12-15 cm in thickness and extends laterally for tens of meters	Sharp upper and lower contact	Va = 2	W and E
Fm	silty clay, with red stains	well sorted	10YR 6/2-2.5YR 5/6	Structureless	Lens is 12-15 cm in thickness and extends laterally for tens of meters	Undulating sharp upper and lower contact	Va = 3	W and E
Fn	Nodular Clay	well sorted	10YR 6/2		Lens is 3-5 cm in thickness and extends tens of meters	Distinct upper and lower boundary	Va = 1	E

Munsell Color Chart Abbreviations: YR = Yellow Red. Texture Abbreviations; v = very, m = medium, c. = coarse

Figure 9 Western Lithofacies. A Gravel lithofacies at the bottom of the section, B fine grained lithofacies overlying gravel lithofacies and underlying sandy lithofacies C fine grained lithofacies D Both fine grained lithofacies with interbedded sand lithofacies E Overall Western outcrop

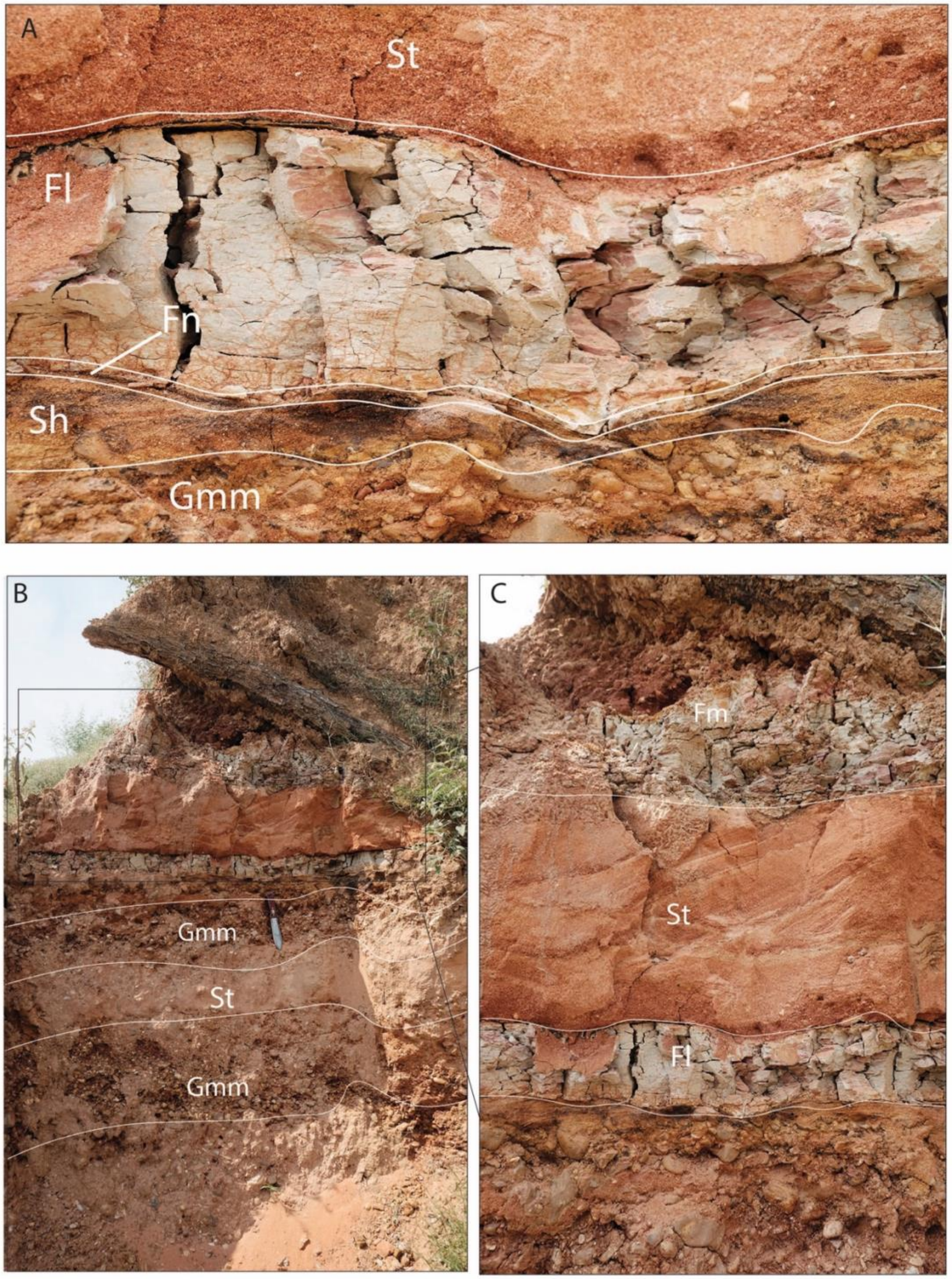

Figure 10 Eastern Lithofacies A fine grained lithofacies overlying nodular clay lithofacies and underlying gravel lithofacies B Gravel lithofacies C Sandy Lithofacies underlying fine grained lithofacies

4.1.2 Architectural Elements

Lithofacies were organized into architectural elements based on Miall’s (2013) and Dalrymple and James (2010) classification systems.

Channels (Gravel Bars and Bedforms and Sandy bars and Bedforms))

Facies may have been deposited within a channel architectural element (Table 3). Most coarse gravel deposits in fluvial systems are deposited in channels (Miall, 2013). Lithofacies that define architectural elements can include almost any lithofacies. This architectural element can represent a sheet concave up erosional base, or an internal concave up 3rd order erosion surface (Table 3 Dalrymple & James, 2010).

Gravel Bars and Bedforms (Gmm, Gmp, Gcp, and Gcm)

Gravel Bars (GB) are generally characterized by the presence of gravel and sand facies that exhibit clast and matrix supported sorting. GB are sheets of gravel with coarse grained to cobble clast and variable sand, clay, or clayey sand matrix. This element is weakly bedded and massive with a yellow orange color when fresh. GB elements are commonly interbedded with sandy bedform elements and may represent a lens, blanket or tabular body (Table 3) (Dalrymple & James, 2010).

Sandy Bedforms (St, Sh)

The Sandy Bedforrms (SB) element consist of sandy lithofacies, dominated by crossbedding sedimentary structures. Typically, this lithofacies appears in the Eastern and Western outcrop as either a lens or between two fine grained clay rich layers with a sharp top and bottom contact (Figure 9D and 10C). The SB element can be interpreted to be a minor crevasse splay, minor bar, channel fills, or a lens (Table 3) (Dalrymple & James, 2010).

Floodplain Fines and Abandoned Channel (Fm, Fl)

The fine-grained sediments in the exposure could represent a variety of environments. The fines are typically deposited as continuous layers with laminated bedding. The fine grained lithofacies can be organized into a Floodplain Fine or Abandoned Channel architectural elements. Floodplain Fine elements can represent the product of a chute or neck cutoff while an Abandoned Channel element is interpreted to represent an overbank sheet flow, floodplain pond or swamp (Table 3) (Dalrymple & James, 2010).

Table 3 Architectural Elements of the Western and Eastern Outcrops.

Element	Symbol	Principal Lithofacies assemblages	Geometry and Relationships
Channels	CH	any combination	finger, lens or sheet concave-up erosional base; scale and shape highly variable; internal concave up 3rd order erosion surface common
Gravel Bars and Bedforms	GB	Gmm, Gmp, Gcp	lens, blanket; usually tabular bodies; commonly interbedded with SB
Sandy Bedforms	SB	St, Sh	Lens, sheet, blanket, wedge, occurs as channel-fills crevasse splays, minor bars
Abandoned Channel	CH(FF)	Fl, Fm	Product of chute or neck cutoff

Table adapted from Dalrymple & James, 2010

4.2 XRD Mineralogy

4.2.1 Global Mineralogy

XRD analysis of the global fraction was performed on six samples from the eastern outcrop (Fm, St, Fl, Fn, and Gmm) and on the two clay rich horizons from the western outcrop (Figure 11). Global fraction mineralogy revealed a sharp quartz peak at ~26.55 °2θ and a sharp K-feldspar peak at ~27.5 °2θ that are ubiquitous throughout the samples. Analysis of the global fraction also revealed that samples: W1, W2, E5, and E4 had nearly identical mineralogy. Global fraction diffraction images also indicated the presence of phyllosilicates such as illite-smectite, mica/illite, and kaolinite (Fig. 11), which will be further evaluated during the presentation of the clay fraction mineralogy.

4.2.2 060 reflection and nature of the octahedral sheet of 2:1 clay mineral

The position of the (060) reflection is beneficial in distinguishing between dioctahedral and trioctahedral clay minerals (Rich, 1957). The 060 reflection is determined from the randomly oriented powders of global fraction (Moore & Reynolds, 1997). Dioctahedral smectites have 060 reflections at 1.50-1.52 Å, whereas trioctahedral smectites have 060 reflections at 1.53-1.54 Å (Schultz, 1969). Global fraction XRD analysis of the clay rich horizons (Figure 12) revealed the presence of dioctahedral smectites, which may be identified as montmorillonite, beidellite or nontronite based on Moore and Reynolds, (1997) (Haldar & Tišljar, 2014)

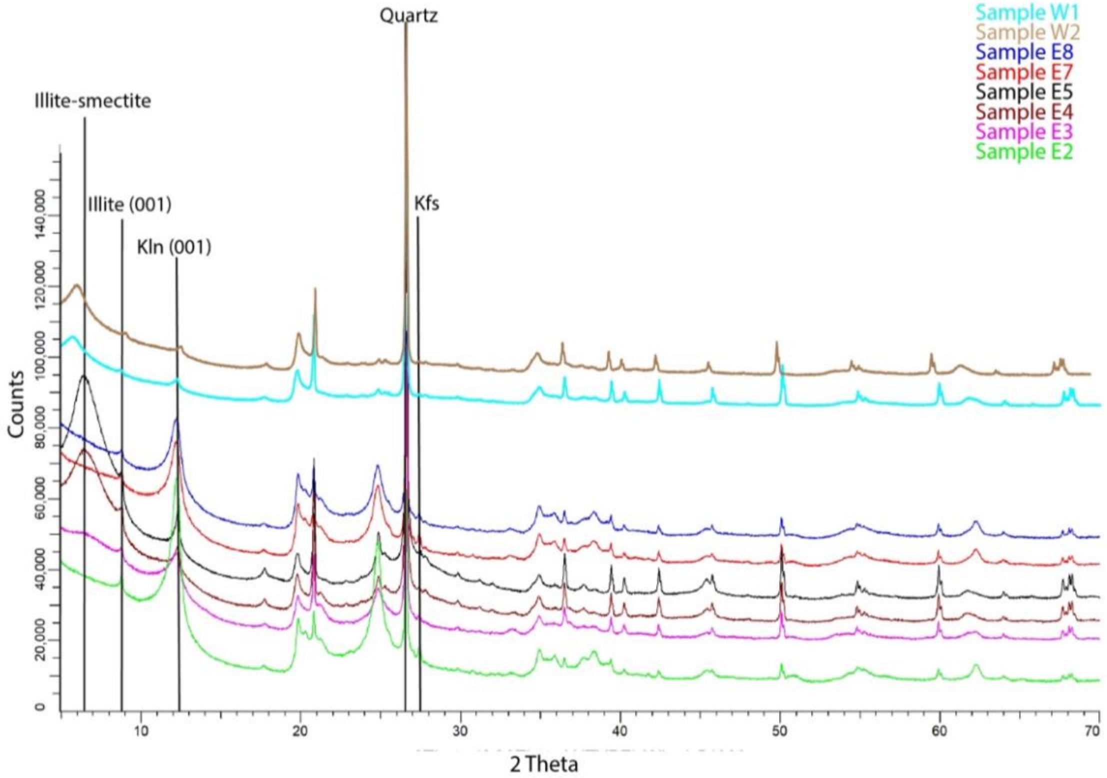

Figure 11 XRD Whole-rock pattern from the west and east outcrop showing the presence of illite-smectite, illite (001), kaolinite (Kln) (001), quartz (Qtz), and K-feldspar (Kfs). Mineral abbreviations after Kretz (1983)

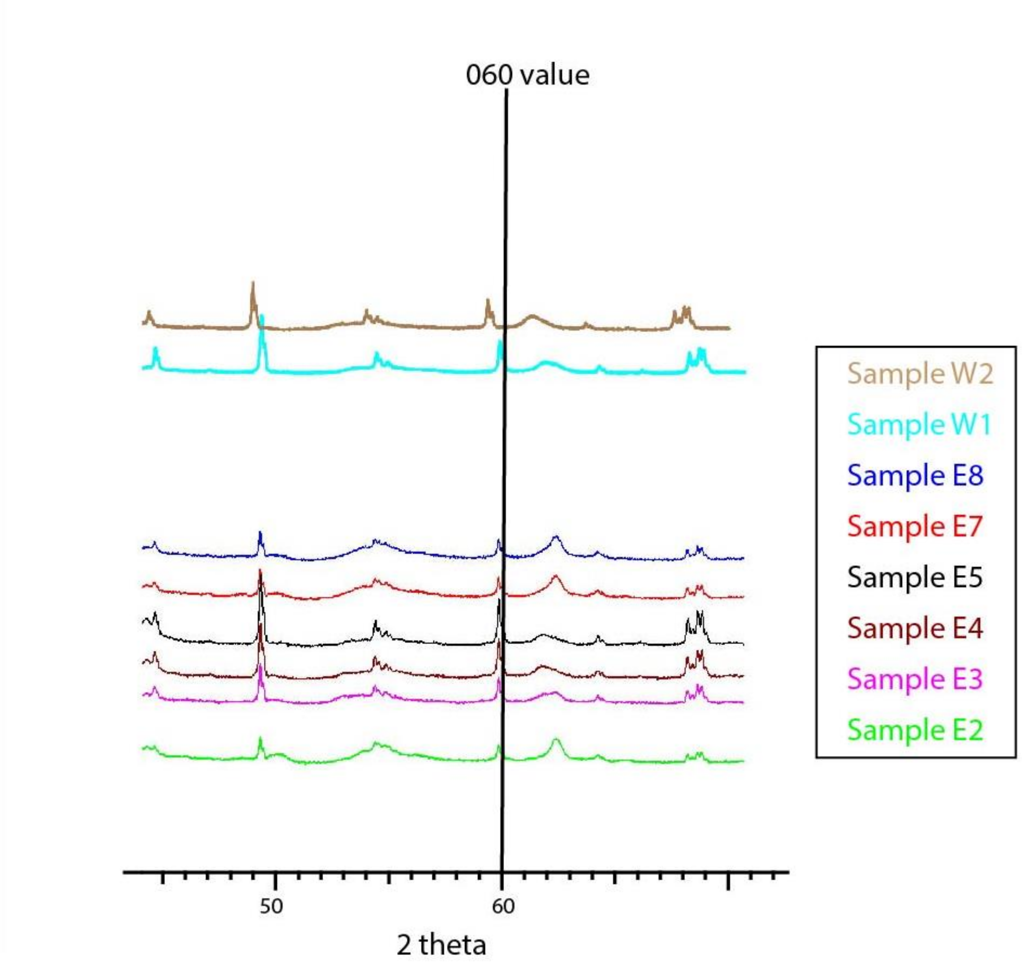

Figure 12 Whole rock fraction 060 peak

4.2.3 Clay Fraction Mineralogy

Clay fraction XRD analysis was performed on the < 2 μm fraction (clay fraction) which was separated from samples E8, E7, E5, E4, E3, and E2 (Fm, St, Fl, Fn, and Gmm). To identify clay minerals from the smectite group and mixed-layered clay minerals, glycolation was performed on samples E8, E7, E5, E4, E3 and E2. Thereafter, the XRD pattern of glycolated samples were compared against untreated ones. Clay minerals present were then identified by diagnostic basal reflections (Brindley, 1952; Moore & Reynolds, 1997). All XRD traces indicated similar clay mineralogy among samples, however the abundance of minerals differed between samples E8, E7, and E2 and samples E5, E4, and E3.

Samples E8, E7, E3, and E2

The <2 μm fractions separated and analyzed from the sand and gravel layers (Figure 13B, 13C, 13E and 13F) and the <2 μm fractions from the topmost clay rich layer in the eastern outcrop (Figure 16A) all exhibited similar mineralogy. Samples E8, E7 and E3 (Figure 13A, 13B, and 14F) can be distinguished by an abundance of kaolinite and to a lesser degree illite.

Samples E8 (Figure13A), and E7 (Figure 13B) had almost identical diffractograms with diagnostic kaolinite 001 and 002 peaks at 12.28 °2θ (7.20 Å) and 24.9 °2θ (3.57 Å), respectively. Illite was identified in both these samples with a basal 001 refection at 8.85 °2θ (3.57 Å). Illite-smectite is present to an even lesser degree with a discrete reflection at 5.18 °2θ (17.00 Å).

The X-ray diffractogram of sample E3 (Figure 14E) has diagnostic kaolinite 001 and 002 peaks at 12.23 °2θ and 24.92 °2θ, respectively. Illite shows a discrete 001 peak at 8.86 °2θ (10.05 Å) while illite-smectite was identified by its first superstructure reflection (001*) at 5.02 °2θ (17.57 Å) that appeared after glycolation. Sample E3 had less distinct kaolinite peaks compared to samples E8 and E7, but had a more pronounced 001 illite-smectite peak.

The sample E2 diffractogram (Figure 14F) displayed a sharper 001 and 002 kaolinite reflections at 12.25 °2θ(7.21 Å) and 24.91 °2θ(3.57 Å), respectively compared to sample E3. A less pronounced illite 001 peak is present in this sample. Illite-smectite 001 reflection was likewise less defined at 5.02 °2θ(17.01 Å). Sample E2 showed an XRD trace more similar to samples E8 and E7 than to E3.

Sample E5 and E4

The clay fraction analyzed from the lower clay rich horizon (E5) as well as the underlying nodular clay (E4) displayed similar mineralogy distinct from the mineral content exhibited by samples E8, E7, E3, and E2.

Sample E5's X-ray diffractogram (Figure 13C) exhibited a diagnostic 001 illite-smectite peak at 5.12 °2θ(17.18 Å) that emerged after glycolation. Illite was identified by the 001 peak it produced at 8.81 °2θ(10.03 Å) while kaolinite was identified by its minute 001 peak at 12.35 °2θ(7.16 Å). This sample stands out from all other samples in its large illite-smectite abundance, with minor amounts of illite and kaolinite.

Similarly sample E4's X-ray diffractogram (Figure 14D) has a mineralogy similar to that of sample E5. This sample was identified by its large 001 illite-smectite peak that appeared after glycolation at 5.21 °2θ(16.69 Å) as well as additional 002 and 003 diagnostic peaks appearing at 10.41 °2θ(8.49 Å) and 26.62 °2θ(3.34 Å). Smaller kaolinite reflections were present and identified by their 001 and 002 peaks at 12.32 °2θ(7.18 Å) and 24.90 °2θ(3.57 Å), respectively. Illite was also present with a 001 peak at 8.85 °2θ(9.99 Å). Sample E4 displayed a diffractogram similar to sample E5 (Figure 14D), however had a slightly smaller illite-smectite 001 peak with a marginally higher amount of illite and kaolinite.

The topmost clay layer (Figure 13A) exhibited a mineralogy different from the lower clay layer (Figure 13C). The principal difference being that the topmost clay layer had a higher abundance of kaolinite and the lower clay layer in contrast had less kaolinite and more illite-smectite. The <2 μm fraction mineralogy of the top clay rich horizon had an almost identical mineralogy to that of the sands and gravels. The global fraction mineralogy of the clay rich horizons from the western outcrop (W1 and W2) compared to the global fraction of the clay rich horizons from the eastern outcrop are almost identical with the exception of the top most clay layer (E8).

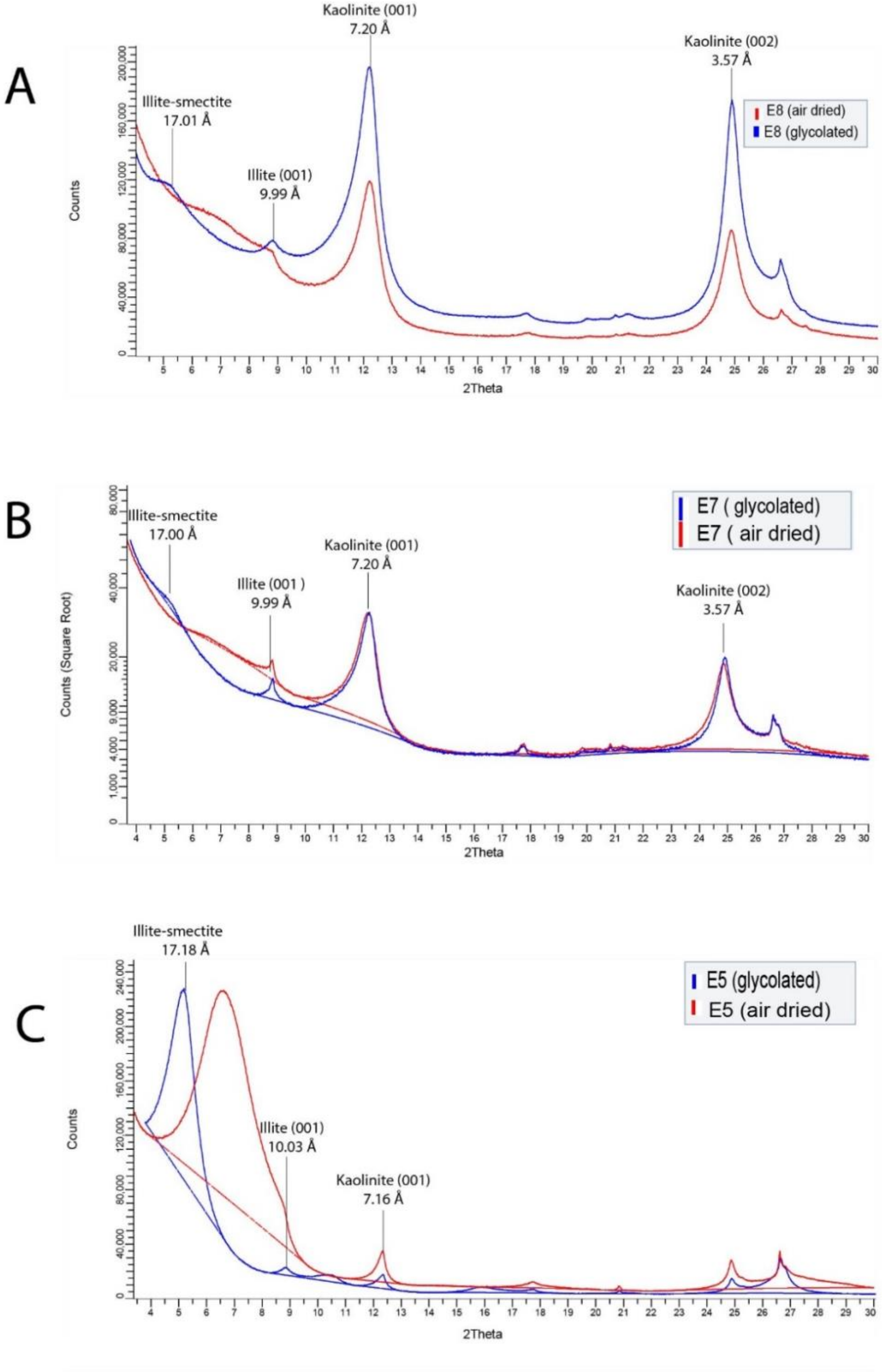

Figure 13 X-ray diffractograms of samples E8-E5 ***A*** *X-ray diffractograms of sample E8* ***B*** *X-ray diffractogram of sample E7* ***C*** *X-ray diffractogram of sample E5*

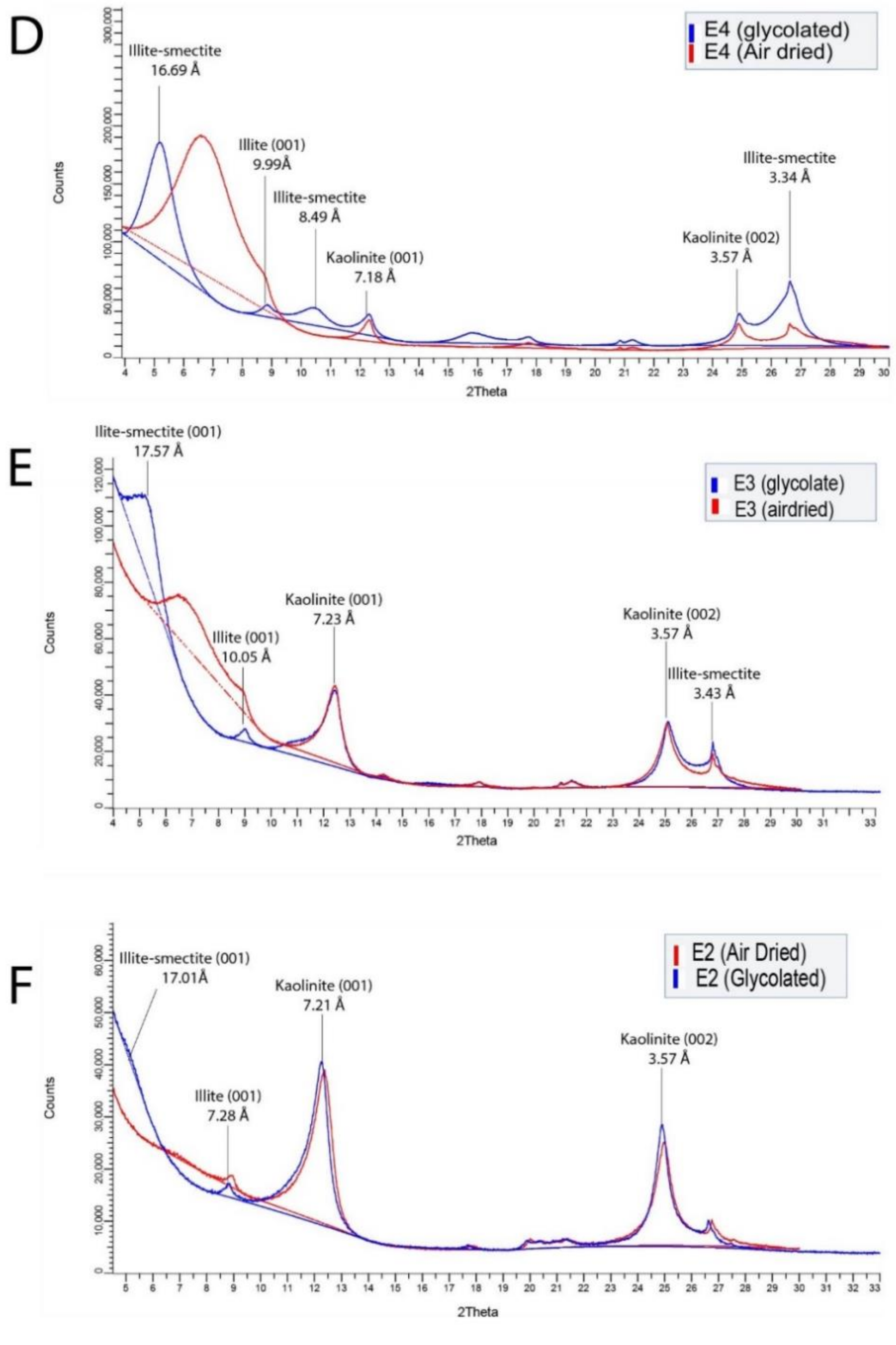

*Figure 14 <2 μm clay fraction X-ray diffractograms **D** X-ray diffractogram of sample E4 **E** X-ray diffractogram of sample E3 **F** X-ray diffractogram of sample*

4.3 Scanning Electron Microscopy-Energy Dispersive X-Ray Spectroscopy

SEM-EDS analysis backscatter electron (BSE) imaging was used to further investigate clay mineralogy and search for igneous phases to substantiate the hypothesis that the clay rich layers present in Drum pit formed from the weathering of pyroclastic material that accumulated in a fluvial system and was later deposited in an abandoned channel. SEM-EDS analysis was conducted on powders from the eastern outcrop (Tables 4-9) and two thin sections made from the clay rich horizons from the western outcrop (Table 10-11). Results from the SEM-EDS analysis found the presence of volcanic glass, sanidine, pumice, albite, and leucite in the clay rich horizons from the western and eastern outcrop. The analysis also discovered igneous minerals in the surrounding sand and gravel layers.

Kaolinite, illite and illite-smectite

The SEM-EDS analysis provided the confirmation of minerals found in the XRD investigation while providing identification of other clay minerals. Kaolinite was an abundant mineral recognized with BSE imaging and phase chemistry, this mineral was identified by its morphology that takes the appearance of a book also known as a kaolinite book (Figure 15A) and high percentage ($\geq$ 40 wt. %) of Al_2O_3 content (Table 4) (Frost & Kristof, 2004). Illite is characterized by the presence of Si, Al, K, and potentially minor amounts of Fe and Mg and usually has ~ 5 wt% K_2O and ~ 9 wt% FeO (Środoń, 2006) (Table 8). Similarly, illite-smectite was recognized by higher concentrations of SiO_2 at ~60 wt% and Al_2O_3 at ~30 wt% and lesser amounts of K_2O, Fe_2O and MgO with concentrations ranging from ~1 to 5 wt% (Table 6). BSE images of hemispherical structures on grain surfaces, are a diagnostic morphological feature of illite-smectite (Figure 15F) which can be indicative of incomplete glass alteration (de la Fuente et al., 2000).

Volcanic Material

Multiple igneous phases were found in almost all samples in the western and eastern outcrop. Volcanic glass was identified by its angular morphology (Figure 18C) and diagnostic phase chemistry (Table 4) containing an abundance of ~80 wt.% SiO_2 relative to a low amount of Al_2O_3 at 12 wt.%. Pumice was recognized in BSE images by its vesicular texture (Figure 15D and 16G). Sanidine was frequently identified in samples (Figure 16G and 16K) by its phase chemistry with an abundance of K_2O at ~15 wt.% (Table 5). Albite was found to a lesser degree and classified by its higher amount of Na_2O (Table 11). Leucite was found in the crossbedded sand layer and was distinguished by its phase chemistry and crystal habit with high K_2O at ~ 20 wt.% (Table 5) and its euhedral, pseudocubic crystals (Figure 16H) (Mazzi et al., 1976; Anthony, 1990).

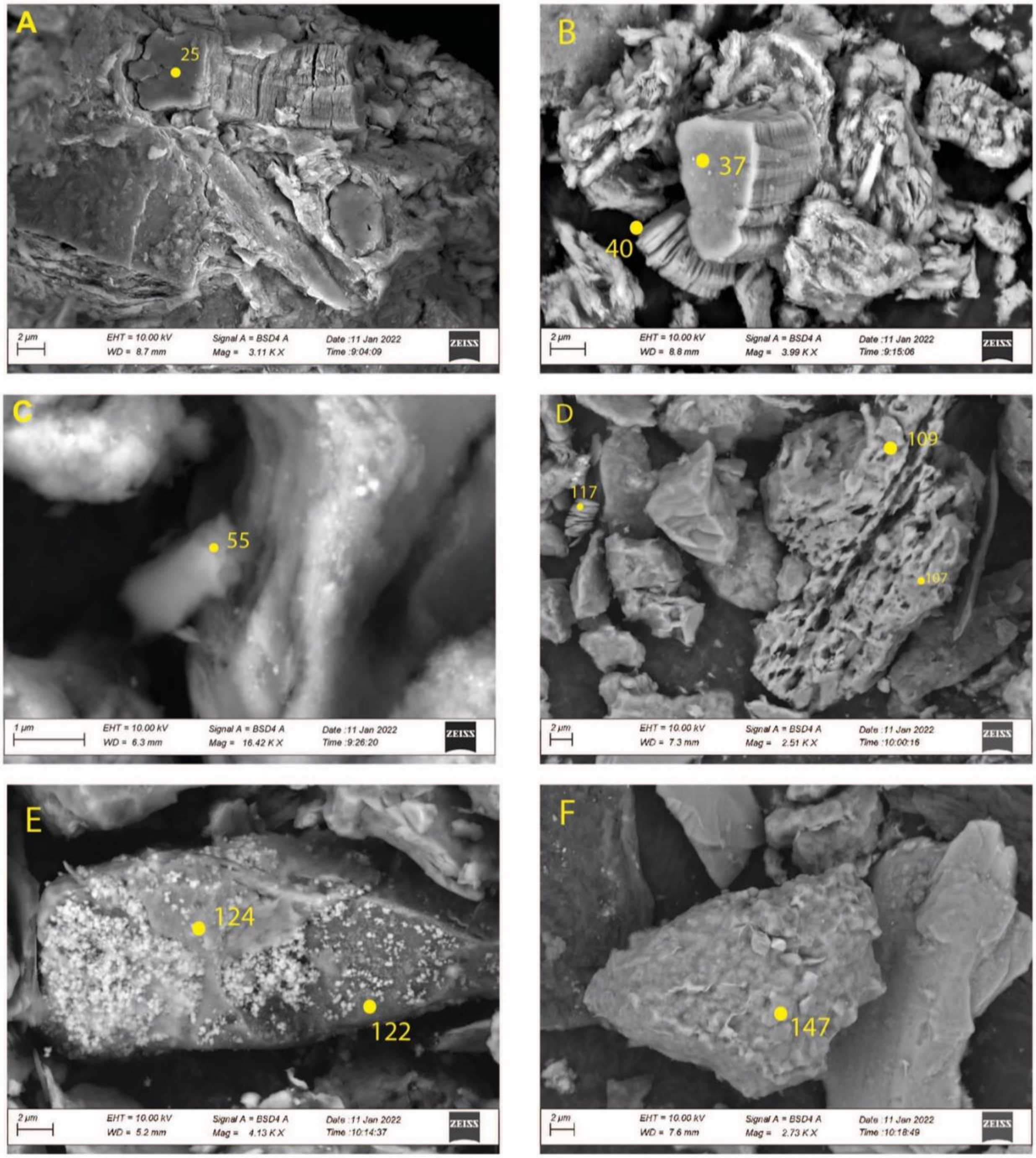

Figure 15 SEM-EDS image and image numbers from the Eastern Outcrops. A. (Image 3) kaolinite, B. (Image 5) kaolinite, C. (Image 5) volcanic glass magnified, D. (image11) pumice grain, E. (Image 12) smectite, F. (image 14) illite-smectite. Yellow dots and numbers correspond with analysis in tables 4-11

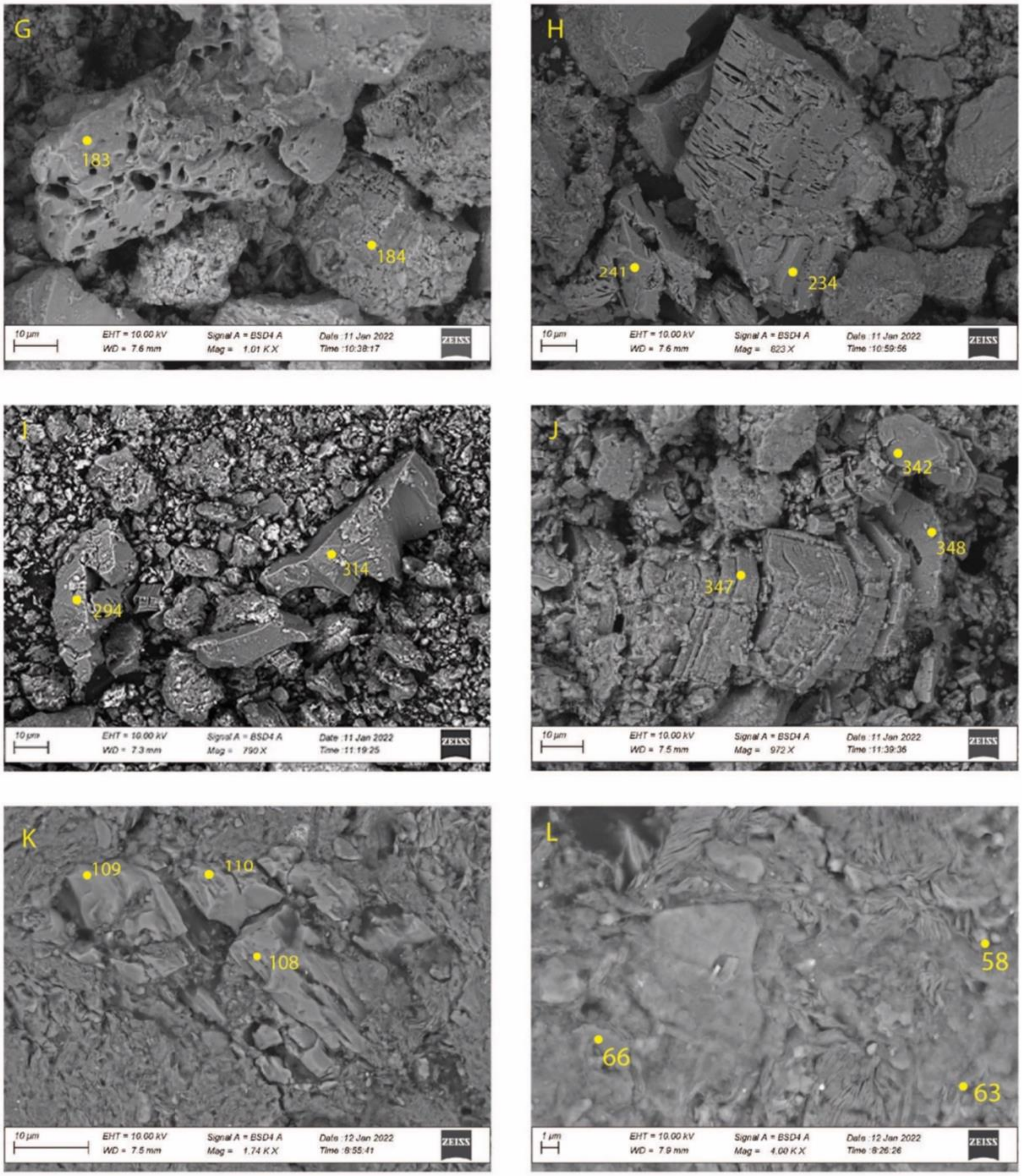

Figure 16 SEM-EDS images and image numbers from the eastern outcrop and images K and L from the western outcrop. G (image 18) pumice and sanidine H (image 22) leucite I (Image 26) volcanic glass J (image 29) kaolinite, K (image 9) sanidine, L (image 4) illite-smectite. Yellow dots and numbers correspond with analysis in tables 4-11.

Table 4. EDS chemistry of representative phases from the top clay layer, sample E8

Sample	E8	E8	E8	E8*	E8*	E8*	E8	E8	E8*	E8
Mineral	Kln	Kln	Kln	Kln	Kln	Kln	Mnt	Mnt	Glass	Glass
image	1	1	1	3	5	5	1	5	5	5
Analysis	-	-	-	25	37	40	-	-	55	57
SiO_2	54.5	53.2	57.9	55.3	55.3	55.3	55	53.6	78.5	78
Al_2O_3	42	44.3	39.2	44.7	44.7	44.8	27.7	31	12	12.5
FeO	2.9	2	0	0	0	1.9	15.9	11.2	9	9
MgO	0.5	0.5	0	0	0	0	0.7	1.4	0.5	0.6
K_2O	0	0	0	0	0	0	0	0	0	0
NaO	0	0	0	0	0	0	0	0	0	0
MnO	0	0	0	0	0	0	0	0	0	0
CaO	0	0	0	0	0	0	0	0	0	0
total	99.9	100	97.1	100	100	102	99.3	97.2	100	100.1

Kln- kaolinite and Mnt- montmorillonite. Mineral abbreviations after Kretz (1983). Samples with asterisks can be found in Figure 18

Table 5 EDS chemistry of representative phases from crossbedded sand, sample E7

Sample	E7	E7	E7*	E7*	E7	E7	E7	E7	E7*	E7*
Mineral	Sa	Sa	Sa	Sa	Sa	Kln	Mnt	Lct	Lct	Lct
image	17	17	18	18	18	19	21	21	22	22
Analysis	-	-	183	184	-	-	-	-	234	241
SiO_2	62.9	63.1	54.3	63.4	63.1	62.2	78.6	55.2	59.7	62.5
Al_2O_3	20	19.9	21.6	20.9	19.3	37.8	19.1	17.8	17	17.7
FeO	0	0	14.6	0	0	0	0	0	0	0
MgO	0	0	0.3	0	0	0	0	0	0	0
K_2O	11.2	11.2	6.7	15.6	17.6	0	2.3	27	21	19.4
NaO	2.9	2.9	2.4	0	0	0	0	0	0	0.4
MnO	0	0	0	0	0	0	0	0	0	0
CaO	0	0	0	0	0	0	0	0	0	0
total	97	97.1	99.9	99.9	100	100	100	100	97.7	100

Kln- kaolinite; Mnt- montmorillonite; Sa- sanidine; Lct-leucite. Mineral abbreviations after Kretz (1983). Analyses with asterisks can be found in Figure 19

Table 6 EDS chemistry of representative phases from the lower clay layer, sample E5

Sample	E5	E5*	E5*	E5*	E5*	E5*	E5*	E5	E5	E5
Mineral	Kln	Sa	Sa	Kln	I-S	Glass	I-S	Mnt	Glass	Kln
image	9	11	11	11	12	12	14	16	16	16
Anlys.	-	107	109-	117	122	124	147	-	-	-
SiO_2	59.6	63.9	65.5	55.7	66.4	86.4	64.3	63	84.3	57.7
Al_2O_3	40.4	24.1	20.7	44.3	21.5	7.5	26.1	33.6	9	42.3
FeO	0	0	0	0	5.1	4.2	0	0	4	0
MgO	0	0.7	0	0	1.4	0.6	4.1	2.4	1.3	0
K_2O	0	11.3	13.9	0	5.6	1.3	5.5	0	1.4	0
NaO	0	0	0	0	0	0	0	1	0	0
MnO	0	0	0	0	0	0	0	0	0	0
CaO	0	0		0	0	0	0	0	0	0
total	100	100	100.1	100	100	100	100	99	100	100

Kln- kaolinite; Sa- sanidine; I-S- illite-smectite. Mineral abbreviations after Kretz (1983)Whitney and Evans (2010) Analyses with asterisks can be found in Figure 18

Table 7 EDS chemistry of representative phases from the nodular clay layer, sample E4

Sample	E4	E4	E4	E4	E4	E4	E4	E4
Mineral	Kln	Sa	I-S	Sa	I-S	I-S	Kln	I-S
image	24	24	24	24	24	24	24	24
Anlys.	-	-	-	-	-	-	-	-
SiO_2	54.5	48.3	52.8	51.7	67.5	48.3	58.4	51.9
Al_2O_3	45.5	35.9	28.8	34.7	17.2	16.8	40.4	25.1
FeO	0	2.1	12.1		10.9	16.2	0	16.4
MgO	0	0.9	4	1	1.4	2.9	0	2.3
K_2O	0	12.8	2.2	12.6	3	0	1.1	4.3
NaO	0	0	0	0	0	0	0	0
MnO	0	0	0	0	0	0	0	0
CaO	0	0	0	0	0	1.2	0	0
TiO_2	0	0	0	0	0	14.7	0	0
total	100	100	99.9	100	100	100.1	99.9	100

Kln- kaolinite; Sa- sanidine; I-S- illite-smectite. Mineral abbreviations after Kretz (1983)

Table 8 EDS chemistry of representative phases from the gravel layer, sample E3

Sample	E3	E3	E3	E3	E3*	E3	E3	E3	E3	E3*
Mineral	Kln	I-S	Mnt	Mnt	Sa	I-S	Ill	I-S	Mnt	Mnt
image	25	25	25	25	26	26	26	26	26	26
Anlys.	-	-	-	-	294	-	-	-	-	314
SiO_2	54.5	43.8	64.5	78.3	65.3	54	49.2	58.5	79.2	74.8
Al_2O_3	44.4	24.3	18.4	11.5	19.5	31.9	34.7	13.1	13.2	10.8
FeO	0	28.7	15.5	7.2	0	11	9.4	27.7	7.2	13.6
MgO	0	1.9	0.6	1.5	0	0.6	1.1	0.7	0.4	0.9
K_2O	0	0.7	0.6	1.5	14.6	2.5	5.6	0.7	0	0
NaO	0	0	0	0	0.6	0	0	0	0	0
MnO	0	0	0	0	0	0	0	0	0	0
CaO	0	0.5	0.4	0	0	0	0	0	0	0
total	98.9	99.9	100	100	100	100	100	100.7	100	100.1

Kln- kaolinite; Mnt- montmorillonite; Sa- sanidine; I-S- illite-smectite; Ill- illite. Mineral abbreviations after Kretz (1983). Analyses with asterisks can be found in Figure 19

Table 9 EDS chemistry of representative phases from the gravel layer, sample E2

Sample	E2	E2	E2	E2	E2	E2	E2	E2*	E2*	E2*
Mineral	Mnt	Sa	Kln	Kln	Kln	Mnt	I-S	Kln	Kln	Kln
image	27	27	27	27	27	28	28	29	29	29
Analysis	-	-	-	-	-	-	-	342	347	348
SiO_2	49.1	64.8	56.5	59.3	56.1	50.8	48.6	53.8	55.5	55
Al_2O_3	36	20.7	43.5	40.7	43.9	34.3	32.4	46.2	44.5	45
FeO	7.6	0	0	0	0	8.8	17.8	0	0	0
MgO	0.9	0	0	0	0	1.1	0.7	0	0	0
K_2O	6.4	14.2	0	0	0	4.9	0.5	0	0	0
NaO	0	0.3	0	0	0	0	0	0	0	0
MnO	0	0	0	0	0	0	0	0	0	0
CaO	0	0	0	0	0	0	0	0	0	0
total	100	100	100	100	100	99.9	100	100	100	100

Kln- kaolinite; Mnt- montmorillonite; Sa- sanidine; I-S- illite-smectite. Mineral abbreviations after Kretz (1983). Analyses with asterisks can be found in Figure 19

Table 10 EDS chemistry of representative phases from the top clay layer, sample W2

Sample	W2	W2	W2	W2	W2	W2	W2	W2*	W2*	W2*
Mineral	Sme	Sme	Sme	Sme	Sme	Ms	Sme	Glass	Kln	Glass
Image	1	1	1	1	1	2	2	4	4	4
Analysis	4	5	7	8	11	24	28	58	66	63
SiO_2	54.3	59	51	58.4	51.2	50.3	49	89.4	56.4	90.4
Al_2O_3	20.8	25.8	20.3	24.7	29.3	40.4	27.3	10	43.6	8.6
FeO	18.7	10.2	24.6	11.3	7.2	0	15.3	0	0	0
MgO	2.9	2.3	1.7	2.5	3.6	0.3	2.4	0.4	0	0.9
K_2O	2.2	1.8	1.4	1.7	8.8	8	6	0	0	0
NaO	0	0	0	0	0	0.9	0	0	0	0
MnO	0	0	0	0	0	0	0	0	0	0
CaO	1.1	1	1.1	1.3	0	0	0	0	0	0
total	100	100.1	100.1	99.9	100.1	99.9	100	99.8	100	99.9

Kln- kaolinite; Sme- smectite; Ms- Muscovite. Mineral abbreviations after Kretz (1983) Analyses with asterisks can be found in Figure 19

Table 11 EDS chemistry of representative phases from the lower clay layer, sample W1

Sample	W1	W1	W1*	W1*	W1*	W1	W1	W1	W1	W1
Mineral	Sme	Kln	Sa	Sa	Sa	Sa	Kln	Kln	Ab	Ab
image	7	7	9	9	9	9	10	10	13	13
Analysis	85	89	108	109	110	112	141	144	165	164
SiO_2	66.4	53	66.1	65.7	65.8	65.4	67.7	55.9	68.2	68.6
Al_2O_3	12.5	42	19.5	18.5	18.9	18.5	28.8	44.1	18.7	19.4
FeO	5.1	5	0	0	0	0	3.5	0	0	0
MgO	16	0	0	0	0	0	0	0	0	0
K_2O	0	0	13.9	14.8	15.3	13.6	0	0	7.3	6.6
NaO	0	0	0.5	1.1	0	1.1	0	0	5.7	5.5
MnO	0	0	0	0	0	0	0	0	0	0
CaO	0	0	0	0	0	0	0	0	0	0
total	100	100	100	100.1	100	98.6	100	100	99.9	100.1

Sme- smectite; Kln- kaolinite; Ab- albite; Sa- sanidine. Mineral abbreviations after Kretz (1983) Analyses with asterisks can be found in Figure 19

Smectite

The smectite group includes dioctahedral aluminum phyllosilicate of montmorillonite, beidellite and nontronite series identified by the 060 (Figure 12) reflection in the clay rich layer (Haldar & Tišljar, 2014). The clay rich beds 060 reflection (Figure 12) ranged from 1.49 to 1.50 Å, indicating the presence of montmorillonite based on Moore and Reynolds (1997). Phase chemistry identification of montmorillonite with Al-Mg-smectite exhibited a phase chemistry consisting of ~52 wt.% SiO_2, ~27 wt.% Al_2O_3, ~10 wt.% CaO and ~10 wt.% Na_2O where Na can be substituted for Ca and Al can be substituted for Mg (Petit et al., 2002) (Table 4 and 6). Montmorillonite is distinguished from beidellite as it is the Al end member of dioctahedral smectite (Petit et al., 2002), which is identified by its large concentration of ~60 wt.% SiO_2, and ~35 wt.% Al_2O_3 and a small concentration of Na_2O at ~5 wt.%. Nontronite is the structural counterpart of beidellite, the Al end member of dioctahedral smectite (Petit et al., 2002). Nontronite is distinct from other smectites with its high iron concentration at ~30 wt.% FeO, and ~4.5 wt.% Na_2O (Haldar & Tišljar, 2014). Nontronite is not explicitly identified in SEM-EDS, however some analysis of illite-smectite (Table 8) have higher concentrations of FeO reaching up to 28 wt.% FeO but have no recorded concentrations of Na2O. This high iron concentration suggest that the identification of certain smectite by phase chemistry may represent intermediate members between nontronite and Al-montmorillonites (Brigatti, 1983).

Diagrams plotting different ratios of octahedral and interlayer cations (Mg, Fe, Al, and K; Fig 18) obtained from EDS were created from chemical compositions of clay minerals determined from major elemental data that was converted into major oxides (in weight %) and normalized to 100%. Smectite, illite-smectite, illite, montmorillonite, and kaolinite compositions were studied using major oxide values plotted over bivariate diagrams (Figure 17) marked with illite, kaolinite, smectite, and chlorite standard compositional fields of Pal et al., (2015). In MgO/Al_2O_3 vs K_2O/Al_2O_3 binary diagram (Figure 17), data plots of smectites, illite-smectie, montmorillonite, kaolinite, and illite are clustered close to the illite and smectite compositional field or in the illite compositional field. In MgO/Al_2O_3 vs CaO/Al_2O_3 binary diagram are generally clustered in the illite compositional field. The data show a positive trending behavior with some illite-smectite and montmorillonite data points located in between the illite and chlorite field (Figure 17) indicating an increase in CaO.

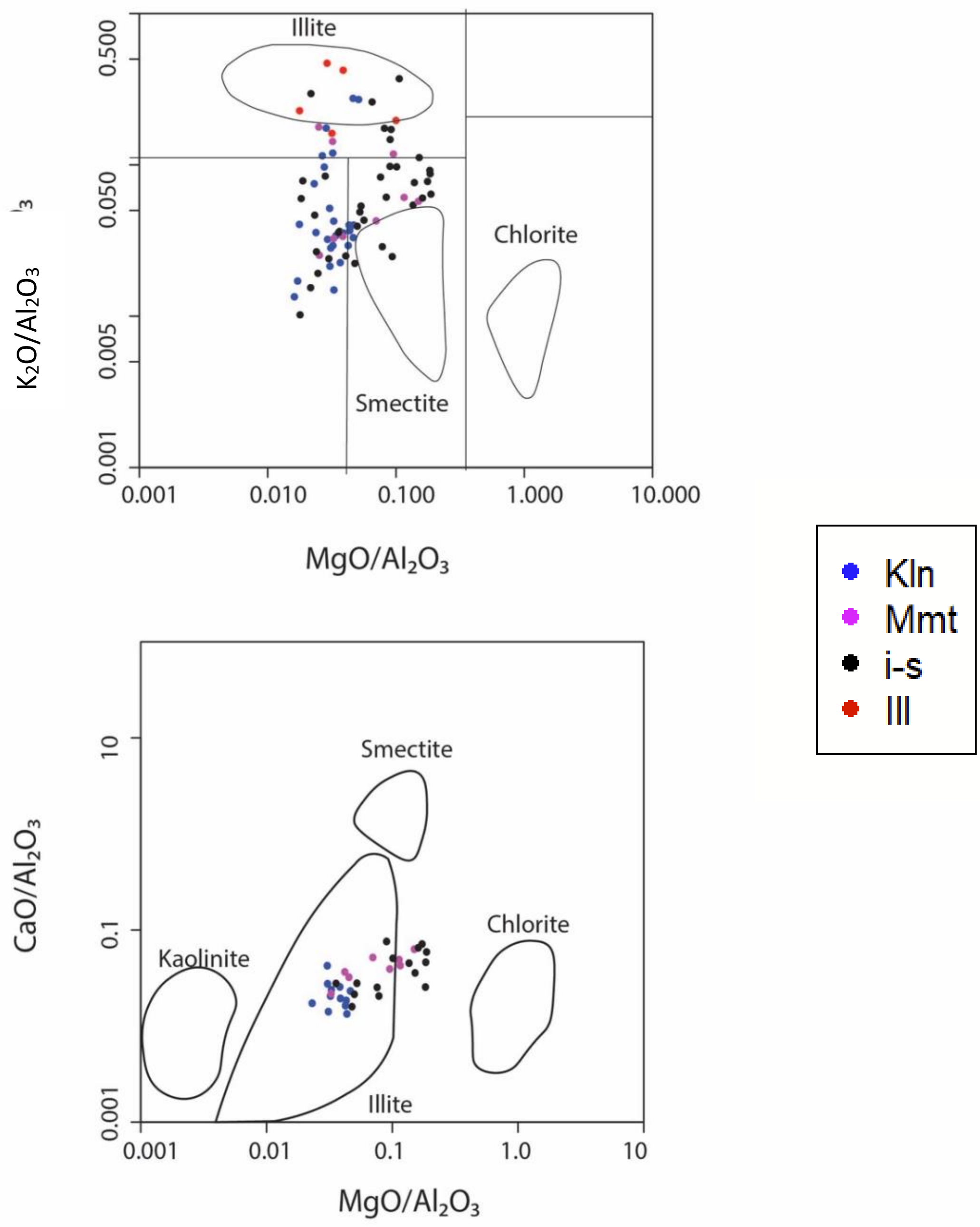

Figure 17 Major oxide data plotted in comparison to the standard clay compositions to delineate clay composition of illites (red), illite-smectite (black), montmorillonite(pink) and kaolinites (blue). Modified from Pal et. al (2015) and Weaver and Pollard (1975)

4.4 Modeling and Qualitative Description of Clay Minerals

Modeling and quantification of clay minerals present in the fine-grained fraction is provided in Figure 18 . One representative sample from the clay rich horizons, sample E5, was modeled since the <2 μm fraction from the clay horizons had identical mineralogy with the exception of sample E8. Clay pattern modelling was helpful in understanding this sample because it is a mixed layer clay, whose features are considered modifiable (Uzarowicz et al., 2012). The model results showed the 001 peak consisting of two composite illite-smectite reflections. One being R1 illite(0.42)/smectite, an illite-smectite dominated by smectite, and the second being an R0 illite(0.8)/smectite, an illite-smectite dominated by illite.

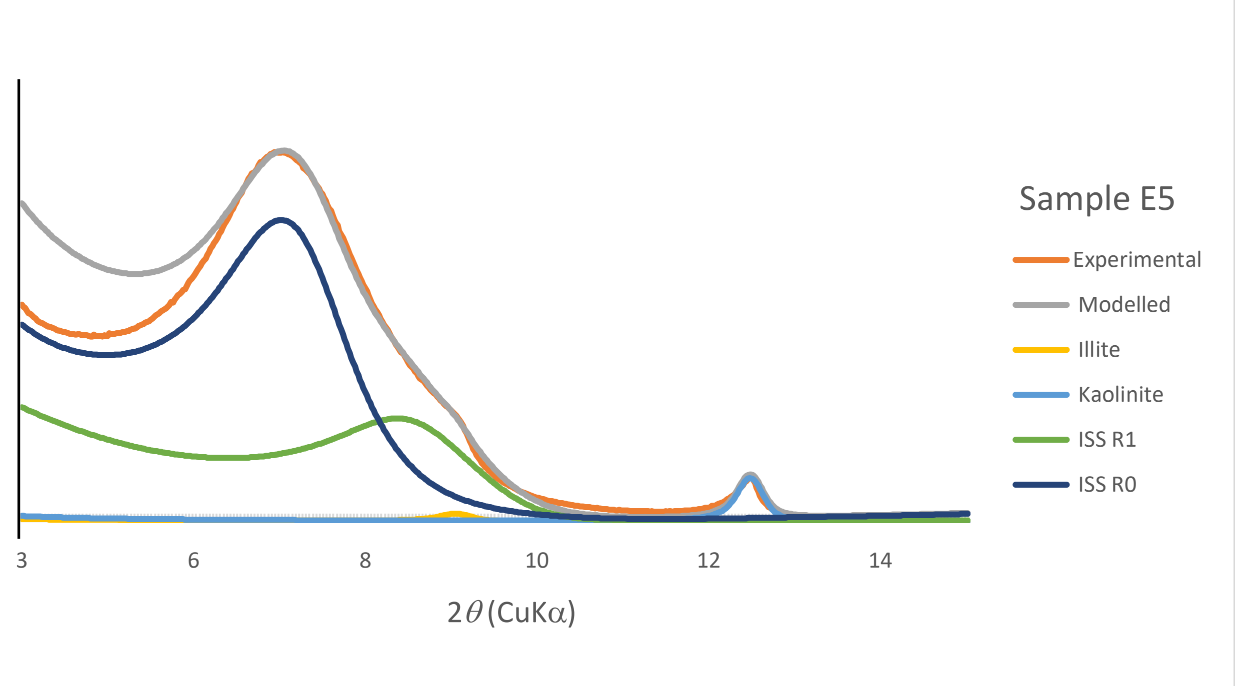

Figure 18 Sybilla© modelling of the experimental XRD spectra of a representative sample from the clay rich horizon (E5). ISS- Illite-smectite, R1-Reichweite 1, R0- Reichwheite 0

4.5 Mineral Assemblages

The overall mineralogic variety of the samples analyzed is fairly uniform (Table 12), the only difference is in the abundance of minerals present. Samples were also distinguished by the variety of igneous minerals identified. All phases measured in the global fraction were recognized in the clay fraction with the exception of quartz and k-feldspars, these two minerals were ubiquitous. Clay fraction mineralogy did not reveal the presence of new minerals; however, it did provide information regarding relative clay mineral abundances. It was shown that the samples from the sand and gravel layers (E7, E3, E2) and one sample from the clay rich horizon (E8) all contained large amounts of kaolinite; this was discerned from clay fraction X-ray diffractograms (Figure 13 and 14) exhibiting large diagnostic kaolinite peaks. The nodular clay layer and lower clay rich horizon X-ray diffractograms, in contrast, showed less illite and kaolinite present, but was more abundant in illite-smectite. The western outcrop's clay rich layers global fraction X-ray diffractogram was identical to that of the lower clay rich layer diffractogram from the eastern outcrop.

SEM-EDS and BSE images discerned a variety of pyroclastic constituents present in all samples. Igneous materials were discerned by their: morphology, texture, and phase chemistry. Glass was identified in most samples by its abundant Al_2O_3 composition relative to SiO_2, and sharp angular morphology. Sanidine and leucite were found primarily by their abundant K_2O content with sanidine typically containing ~ 10 wt. % (Table 7) and leucite typically having ≥ 20 wt.% (Table 5). Conversely, albite was identified by its high Na_2O content (Table 11), while pumice was recognized by its vesicular texture (Figure 18D and 19G). Almost all samples had igneous minerals identified by SEM-EDS. Overall, the top clay rich sample and the gravel and sand samples from the eastern outcrop had abundant kaolinite with various igneous phases

(Figure 16). The nodular clay layer and lower clay rich layer from the eastern outcrop were distinguished by their large amount of illite-smectite, while also having various igneous minerals present. The western outcrop clay rich horizons had global diffractograms identical to that of the lower clay rich horizon diffractograms from the eastern outcrop. The western outcrops SEM-EDS analysis identified predominantly volcanic glass and sanidine.

Table 12. XRD and SEM-EDS mineralogy of analyzed samples

Sample	**XRD Mineral Composition (Global Fraction)**	**XRD Mineral Composition (Clay Fraction)**	**SEM Mineral Composition**
E8	I/M I-S, Kln, Qz, Kfs		Glass
E7	I/M, I-S, Kln, Qz, Kfs		Sa, Glass, Lct
E5	I/M, I-S, Kln, Qz, Kfs		Glass
E4	I/M, I-S, Kln, Qz, Kfs		Sa
E3	I/M, I-S, Kln, Qz, Kfs		Glass, Sa
E2	I/M, I-S, Kln, Qz, Kfs		Glass
W2	I/M, I-S, Kln, Qz, Kfs		Glass
W1	I/M, I-S, Kln, Qz, Kfs		Sa, Ab

Kln- kaolinite; Sa- sanidine; Lct-leucite; Ill- Illite; I-S- illite-smectite; Ab- albite; Ms- muscovite. Mineral abbreviations after Kretz (1983)

Chapter 5

Discussion

5.1 Origin of Clay beds

Mineralogical analysis of clay rich horizons and adjacent sand and gravel layers from the western (Figure 6) and eastern (Figure 7) outcrop revealed that three of the four clay rich layers have identical mineralogy. Clay fraction XRD analysis revealed that both clay rich horizons from the western outcrop and a single clay rich horizon from the eastern outcrop were dominated by illite-smectite with large 001 basal peaks (Figure 13C). The sand and gravel layers in addition to the other clay rich horizon from the eastern outcrop were abundant in kaolinite (Figure 13A, 13B, 14E and 14F), which all exhibited distinct 001 and 002 peaks. Clay modelling of the air-dried composite 001 basal reflection of illite-smectite (Figure 18) further identified the presence of two illite-smectite phases, one phase having 80% of illite component and the other phase having 40% of illite component. A rather minute 001 reflection of discrete mica/illite was detected in all samples in the western and eastern outcrop (Figure 13 and 14). SEM-EDS analysis and BSE images revealed the presence of volcanic phases in every sample (Table 12). The abundance of illite-smectite in the clay rich horizons can be better understood through investigating its formation. During diagenesis, smectite alters to illite in the general reaction sequence: smectite → random illite-smectite→ ordered illite-smectite→ illite (Hong et al., 2017).

Smectite can form from volcanic glass, directly in pore spaces of sandstone and could form in weathering environments characterized by very slow movement of water, whether swampy lowlands or in arid to semiarid regions (Berner, 1971; Moore & Reynolds, 1997). The lack of organic material present in the sample is not consistent with a swampy environment, and smectite was not found in pore spaces of sandstone. The clay rich horizon may have been deposited in an environment with slow moving water, however the presence of volcanic glass in addition to hemispherical structures on the surface of the grains (Figure 14F) which is indicative of incomplete glass alteration (de la Fuente et al., 2000) infers that smectite likely formed from volcanic glass. Volcanic ash in general is thermodynamically unstable and highly reactive when deposited in supergene environments (Hong et al., 2017). Weathering and alteration of ash takes place rapidly during early diagenesis, and volcanic glass will rapidly devitrify and convert to authigenic clay minerals (Hong et al., 2017). This fits with the interpretation that smectite was deposited with other K-rich volcanic material that enabled the alteration of smectite to illite-smectite (Šegvić et al., 2014)

The conversion of smectite to illite through a mixed-layer or interstratified illite-smectite series can occur as a result of the exposure to higher temperatures associated with deep burial diagenesis (Pollastro, 1985; Ferrage et al., 2011; Galán & Ferrell, 2013) or at low surface temperatures in continental environments (Sandler & Harlavan, 2006) particularly in hypersaline environments and in the presence of Fe-smectite (Huggett, 2005). The clay layers in Crowley's Ridge, however do not meet most of these conditions. The sand and gravel layers as well as the clay layers showed no indication of being exposed to higher temperatures, and the literature does not corroborate the presence of a heat source possible to convert smectite to illite (Autin, 1996). Given the geologic context, illitization could not have occurred in a hypersaline environment at lower temperatures because the clay rich horizons were deposited in what is interpreted to be a Quaternary fluvial deposit, which practically did not undergo any burial (Van Arsdale et al., 2007; Cox et al., 2014). SEM-EDS analysis however, does satisfy one of the mentioned conditions, the abundance of Fe in the system. High concentrations of Fe can be associated with reducing conditions in water saturated environments, such as those where repeated wetting and drying cycles are produced (Huggett, 2005).

These aforementioned wetting and drying cycles are acknowledged to produce K fixation in smectite and illite although smectite is the more likely precursor since it is a major clay mineral responsible for K fixation and has been demonstrated to have more faculty to fix K compared to other 2:1 minerals due to the higher specific surface area and negative layered charge (Brady & Weil, 2008). Illitization as a result of K fixation can happen in various ways such as a response to slow sediment accumulation, which allows clay minerals to be in contact with seawater for extended periods of time (Schultz, 1978). Alternatively K fixation takes place from repeated wetting and drying cycles, thus enabling the illitization process (Środoń & Eberl, 1984). The latter explanation for the cause of K fixation is more probable because the clay layers were deposited in a continental freshwater environment, not in a marine environment. The clay rich horizons are interpreted to have formed in a fluvial environment as an an abandoned channel facies (Table 3) surrounded by high energy fluvial facies (Miall, 1996). Both environments would represent extended periods of sediment accumulation and contact with a fluid medium that fits the scope necessary for K fixation (Schultz, 1978).

K fixation occurs when wetting and drying concentrates K from sparingly soluble K rich components (Davis & Hayes, 1987). The fixation of K, or the entrapment of K^+ ions irreversibly in between 2:1 collapsed phyllosilicate layers, occurs when the interlayer space collapses due to dehydration or drying (Florence et al., 2017). K fixation is a solid-state transformation (SST) mechanism that occurs during wetting and drying of smectite at earth's surface (Altaner, 1997). The fixation of potassium is expected to occur wherever smectite and k components are subjected to the wetting and drying processes (Florence et al., 2017). SST mechanisms associated with k fixation typically involves the gradual replacement of the parent mineral (smectite) by the daughter mineral (illite) in close topatic contact in polar 2:1 layers (Altaner, 1997). Both continuous solid-state transformation (Hower et al. 1976) and stepwise dissolution-precipitation mechanisms (Boles and Franks 1979; Nadeau et al. 1985) have been proposed for the formation of illite. The transformation model explains that the tetrahedral charge is developed through solid-state Al for Si substitution while the 2: I layer structure of the reactant smectite was retained. The dissolution-precipitation model explains that low charged smectite dissolves and tetrahedrally high charged illite crystallizes from solution.

Paleoclimate interpretations and clay modelling results is consistent with the conditions necessary for the gradual replacement of smectite by illite. If a sample has 0–60% illite in illite-smectite, this means that the clay is likely the product of pedogenic illitization, consistent with clay modelling results indicating ~40 % illite (Figure 18) suggesting that illitization was likely promoted through wetting and drying in a seasonal climate (McIntosh et al., 2021) or an environment with periodic flooding (Środoń & Eberl, 1984). These inferences fit the general interpretations of the past climatic conditions of the UC which include: periodic meltwater flooding associated with deglaciation (Self et al., 1986), heavy rainfall associated with a subtropical environment (Potter, 1955), or periodic flooding as a result of seasonal rainfall (Autin, 1996). All of these factors potentially provide the necessary climatic regime important for forming significant illite layers (Środoń & Eberl, 1984). For the conversion of smectite to illite/smectite associated with K fixation to occur, a source of K must be available (Pollastro, 1985). The global fraction XRD results indicated that K-feldspar is indeed present (Figure 11). Additionally, SEM-EDS phase chemistry revealed presence of K-rich igneous components (Table 5 and 11) such as leucite, volcanic glass, sanidine (Figure 15). Their decomposition could have provided the source for K fixation to occur (Šegvić et al., 2014).

Global fraction XRD analysis produced a 060 peak (Figure 12) which is indicative of montmorillonite, a dioctahedral smectite (Moore & Reynolds, 1997). The identification of montmorillonite also reinforces a pyroclastic origin since volcanic ash commonly alters into montmorillonite (Berti et al., 2022). SEM-EDS analysis not only revealed the presence of montmorillonite, but the potential occurrence of members of a montmorillonite-nontronite series. Phase chemistry of montmorillonite samples had high amounts of Fe suggesting that smectitic material potentially represents intermediate members between nontronite and Al-montmorillonites (Brigatti, 1983). Major oxide plots (Figure 17) of MgO/Al_2O_3 vs K_2O/Al_2O_3 indicates a positive trend of smectite data points in the illite field and outside the field that shows a gradual enrichment in CaO or an increase in montmorillonite. Phase chemistry of smectitic material enriched in CaO also had increasing amounts of FeO (Table 10) which supports the presence of an intermediate montmorillonite-nontronite members. The occurrence of this intermediate nontronite member can form in a variety of environments. Sherman et al. (1962) described the occurrences of nontronite and nontronite-like minerals in soils from weathered basalts and found that alteration is related to both the mode of occurrence of the parent rocks and the climatic (semi-arid, moderate rainfall, and humid tropical rainforest) and weathering environments consistent with the paleoclimate of the UC. The occurrence of nontronite veins has also been observed as an alteration product of volcanoclastic rocks in the Milos bentonites, Greece (Ece, 1999).

The minor mica/illite peaks present in the gravel and sand layers and in the clay rich. can be detrital or form as recycled material in sedimentary rocks, during pedogenic or weathering processes, and diagenetically (Moore & Reynolds, 1997). The mica/illite was not discovered in any paleosols and was not buried at depth or for any extended period of time. The samples analyzed were all deposited in fluvial environments, and the limited presence of mica/illite material can be best explained as being detrital. Sybilla© modelling results (Figure 18) reinforce a detrital origin because the weathering of mica/illite produces illite rich illite-smectite (Righi, 1993) consistent with the modelled 001 peak of illite rich illite-smectite.

The large amount of kaolinite identified in XRD and SEM-EDS analysis in the sand and gravel layers may be the result of residual weathering, precipitation or hydrothermal alteration of other aluminosilicates, in particular feldspar (Moore & Reynolds, 1997). The presence of large basal 001 kaolinite peaks (Figures 13 and 14) in all sand and gravel XRD traces is indicative of vertical precipitation of kaolinite grains (Islam et al., 2002). It is probable that kaolinite precipitated from the percolation of fluid, this fits with the paleoclimate of the UC interpreted to be the same as the modern climate (Potter, 1955; Self et al., 1986) which is a subtropical climate (Gray & Ferguson, 1977) thus, providing the mechanism necessary for the formation of kaolinite. The XRD results for the (Figure 13B, 14E, and 14F) kaolinite rich sand and gravel layers in the eastern outcrop were identical to the upper clay rich horizon from the eastern out crop (Figure 13C). The other clay layers rich layers, however, were abundant in illite-smectite, all exhibiting large 001 illite-smectite peaks and were all indistinguishable. The clay rich horizon abundant in kaolinite is an outlier relative to the lower clay rich layer in the eastern outcrop and the clay layers in the western outcrop.

The presence of kaolinite in the clay rich horizon could be explained by; detrital contamination, clay translocation or as a result of percolation from late modern fluids which affected a top portion of the profile. A detrital contamination appears unlikely because detrital grains typically exhibit low crystallinity and anhedral morphology while diagenetic kaolinite grains exhibit a high degree of crystallinity with hexagonal euhedral plates (Bauluz et al., 2008). High to moderate crystalinity and hexagonal euhedral plates were observed in BSE images (Figure 16J) indicating a diagenetic origin. Percolation typically occurs in coarse very permeable mediums such as gravel and sand, like those found surrounding the clay rich horizons (Hall, 1983). This coupled with the fact that the gravel and sand layer above the kaolin rich clay layer has been mined away and greatly disturbed (Figure 7). This reinforces the idea that kaolinite precipitated from a large volume of water percolating downwards giving rise to kaolinite crystallization vertically across the studied profile. The kaolinite grains could not have been transported large distances since delicate aggregates of kaolinite grains cannot be sustain great distances without being destroyed or altered considerably (Shelton, 1964). Another interpretation may be the translocation of clay minerals, particularly the < 1 μm, which is known to infiltrate micro and macropores (Mohammadnia & Kowsar, 2003). The kaolinite grains observed in BSE images were very coarse however, exceeding 1 μm (Figure 16J) making clay translocation an unlikely explanation.

5.2 Provenance of Clay beds in Crowley's Ridge

Primary minerals in volcanic ash that survived the post-depositional alteration includes sanidine, altered volcanic glass and less stable primary minerals include the formation of smectite and mixed-layer illite-smectite (Dai et al., 2017). XRD and SEM-EDS analysis identified minerals and phases that correspond to primary stable and unstable minerals found in volcanic ash, indicating a pyroclastic origin (Table 12). Identifying the volcanic source of the airfall ash deposit can be deduced from mineralogy and phase chemistry as well as geologic context. The geologic age of the source eruption must have occurred between ~2.6 to 0.2 Ma. Another clue is the presence of pumice (Figure 15D and 16G), which is indicative of a violent eruption and commonly forms from catastrophic fragmentation of vesicular magma or lava, mainly of felsic composition (Klug et al., 2002; Kano, 2003; Dellino et al., 2005).

Minerals identified in SEM-EDS analysis that are useful in better understanding the volcanic provenances include sanidine and leucite. Sanidine was distinguished from orthoclase by its phase chemistry. Analysis of sanidine typically exhibited a chemistry that did not exceed ~16 wt %. in K_2O (Table 6) while orthoclase typically shows ≥ 16 wt.%. Leucite is a K-rich, silica undersaturated igneous mineral commonly formed in alkaline magmas (Gittins, 2015). Major alkaline provinces can typically be found in stable continental regions such as in east and central Africa along rift valleys (Bailey, 1964), around mantle plumes and hotspots (Pirajno, 2004) or conversely at subduction zones (Cruz-Uribe et al., 2018). Leucite formation has also been interpreted to occur from the partial melting of mantle material (Edgar, 1987).While sanidine is the high temperature alkaline K-Na feldspar and forms from the crystallization of lavas at high temperatures with rapid cooling, it is usually found in rhyolites, trachytes, and dacites (Haldar, 2020).

It can be inferred from XRD and SEM analysis that a caldera forming eruption is likely the event that produced and distributed the material necessary to form the clay rich horizons. The four caldera forming eruptions that occurred during the Quaternary that are of interest include Yellowstone Caldera, Valles Caldera, Long Valley Caldera and the Acoculco Caldera Complex (Figure 22). To discern the provenance of the ash deposit, it is necessary to consider: the distance of the volcanic source from the study area, the age of the sediment layer the clay rich horizon was deposited in, the volume and distribution of the ashfall, and the phase chemistry of the pyroclastic material in the clay rich horizon and adjacent sand and gravel layers. Another important constraint is that the two clay layers present in each outcrop (Figure 6 and 7) are most likely the products of two separate eruptions, or at least a period of time between each ashfall based off the two clay beds separated by a sandy layer.

5 .2.1 Valles Caldera

The Valles Caldera is a resurgent caldera (Smith & Bailey, 1968) located in north central New Mexico, ~ 1,437 km away from the study area (Figure 19; Table 13). The Valles Caldera formed during two major rhyolitic ignimbrite episodes, the first occurring at 1.61 Ma with the eruption of the Otowi Member of the Bandelier Tuff after 13 Ma years of volcanic activity (Wolff & Gardner, 1995). Subsequent activity produced intracaldera high silica rhyolite domes and associated tuffs (Smith & Ross, 1970). At 1.22 Ma, the Tshirege Member of the Bandelier Tuff erupted to form the Valles Caldera on approximately the same site as the earlier structure (Table 13) (Self et al., 1986). The Tshirege Member and the Otowi Member are of interest because both these members contain Plinian ash fall units, together these members comprise the Bandelier Tuff which has a combined magma volume of 650 km^3 (Crowe et al., 1978).

While little literature mentioning the distribution of the Tshirege member ash fall units exists, estimations of the eruptive volume of the Plinian ash fall from the Otowi Member have been calculated (Cook et al., 2016). Even though the ash fall deposits from the Tshirege Member happened after the Otowi ashfall units were deposited, both eruptions displaced a similar volume of material (Self et al., 1996). Within the Otowi Member exist the Guaje Plinian deposits, which consist of five fall units (Self et al., 1986). The estimated bulk volume of the first unit could be as little as 7 km^3 or as much as 30 km^3 and the other units could represent as much as 65 km^3 bulk volume (Self et al., 1996). The combined ash fall units results in a total fall volume of 187 km^3 or 68 km^3 or 65 km^{3}and reaching as far as West Texas ~50 km from Lubbock (Cook et al., 2016).

Valles Caldera is part of a silicic volcano that formed at the intersection of a volcanically active lineament and tectonically active rift (Goff & Grigsby, 1982). Most of the volcanic field has been dominated by mafic to intermediate volcanism and around 1.8 Ma transitioned to exclusively rhyolitic volcanism (Wolff & Gardner, 1995). Valles Caldera's earlier history of volcanism may potentially explain the presence of minerals found in SEM-EDS analysis such as leucite. While an explosive rhyolitic eruption may explain the presence of pumice and sanidine.

Unfortunately, the mafic and intermediate volcanism preceded the rhyolitic eruption, which is problematic in explaining the presence of leucite. The biggest disadvantage however, is the distribution and paleotransportation. Cook et al. (2016) calculated the general distribution moving in southeast direction away from the study area, while Izett et al. (1972) mapped the ash fall only reaching as far as ~50 km east of Lubbock, TX, far short of the distance necessary to reach the study area. While Valles Caldera experienced two eruption events responsible for two different ash fall units, the lack of far-reaching distribution for either eruption makes Valles Caldera an unlikely source.

5.2.2 Yellowstone Caldera

The Yellowstone Caldera is located in Northwestern Wyoming and ~1,175 km from the study area (Figure 19; Table 13). Yellowstone Plateau volcanic field referred to as Yellowstone produced three of the largest caldera forming eruptions during the Quaternary as well as numerous smaller-volume intra-caldera eruptions before and after caldera-forming events (Christiansen, 1984). The volcanism responsible for the volcanic field is a product of basaltic magmas ascending from a mantle plume to interact with a silicic-rich continental crust producing partial melts of rhyolitic composition and the characteristic caldera-forming volcanism of Yellowstone (Smith & Braile, 1994). Yellowstone is a part of a 800 km linear age progression of volcanic centers, forming the Yellowstone hotspot track (Smith & Braile, 1994).

Approximately 6,500 km^3 of magma has been erupted from Yellowstone over three caldera cycles during which the Huckleberry Ridge, Mesa Falls, and Lava Creek Tuffs were erupted at 2.077 ± 0.003 Ma, 1.300 ± 0.001 Ma, and 0.6313 ± 0.0043 Ma (Table 13) (Christiansen, 1984; Watts et al., 2012). While the available hotspot ash fall tuff record commences at ~16 Ma, shortly after the initiation of hotspot silicic volcanism at ~16.5 Ma, and continues through the most recent explosive eruptions in the late Pleistocene, only the Huckleberry Ridge, Mesa falls, and Lava Creek Tuffs are of interest because they fit within the allotted time range discussed earlier of 2.6 Ma to 0.02 Ma (Christiansen, 1984).

The Huckleberry Ridge Tuff (HRT) is the oldest eruption that will be examined in this discussion at ~2.077 Ma, with the largest volume and distribution at ~2,500 km^3 (Swallow et al., 2019) with a documented distribution reaching as far as the state of Iowa (Mastin et al., 2014).

HRT produced two fall deposits and three ignimbrite members (A, B, and C), pre-A fall deposits took two weeks to erupted, then breaks of weeks to months between members A and B, and years to decades between B and C with an additional pre-C fall deposit (Swallow et al., 2019).

The second and volumetrically smallest Yellowstone eruption was the Mesa Fall Tuff (MFT) at 280 km^3 that occurred ~1.3 Ma (Christiansen, 2001). The MFT has been interpreted as a single eruptive unit, sourced from the Henry's Fork caldera in the Island Park, Idaho region (Rivera et al., 2016). The distribution of MFT is significantly smaller than that of HRT with fewer ash beds present and the furthest one extending to Nebraska (Izett et al., 1972).

The Lava Creek Tuff (LCT) is the product of the youngest Yellowstone eruption at ~0.6 Ma. The eruption aggregated more than 1,000 km^3, and formed an ash-flow plateau that buried an area of more than 7,500 km^2 and, like the first two volcanic cycles, produced windblown ash that accumulated in ponds and topographic lows on the Great Plains of Nebraska and Kansas to depths of as much as 9 meters and that can be found in Pleistocene deposits from California to Iowa, and Canada to Mexico (Izett et al., 1972; Christiansen, 2001). This caldera forming eruption is traditionally thought to have produced two members, LCT-A and LCT-B, which represent two eruptive phases indistinguishable in age but separated by a cooling break (Christiansen, 2001). LCT may have two additional tuff units that precede both members A and B; however, their relative volumes remain unknown (Wilson et al. 2018). LCT-A and -B are approximately equal in volume (~ 500 km^3) with the ash from the earlier erupted LCT-A covering a more limited region relative to LCT-B. LCT-A distribution is estimated to cover the state of Wyoming, while LCT-B distribution reaches as far as Arkansas (Izett et al., 1972). LCT deposits including ignimbrite and ash are distributed around Yellowstone caldera and their isopach distributions suggest each member (A and B) erupted from separate caldera ring fracture vents (Shamloo & Till, 2019).

Yellowstone's multiple caldera forming eruptions provide likely sources for the clay layers. MFT can be immediately ruled out because of its limited distribution (Figure 22e), however HRT and LCT appear to be likely sources. LCT fits the appropriate distribution, however the documented dispersal of the HRT does not reach the study area. HRT erupted volume was almost twice of LCT and it may be that the distribution of HRT is not well documented since volcanic ash is thermodynamically unstable and highly reactive when deposited in supergene environments (Hong et al., 2017) or distribution was limited depending on the seasonal wind (Figure 23e). It should be stated that the western (Figure 11) and eastern outcrop (Figure 12) have two clay rich horizons separated by a crossbedded sand layer, meaning that it is likely that two separate ash falls separated by some period of time are responsible for the deposition of both clay rich horizons. This makes HRT a more likely candidate since it experienced a larger volume eruption with pre-A fall deposits taking two weeks to be erupted, then years to decades to erupt pre-C fall deposit (Swallow et al., 2019). Even though LCT formed from two eruptions it is still less likely because LCT A, its first eruption, had a very limited extent (Izett et al., 1972). The explosive silicic volcanism associated continental hotspots explains the presence of pumice (Christiansen, 1984). Alkaline magmatic sources, typically associated with the formation of leucite, are formed during mantle metasomatism (Balashov & Glaznev, 2006). This is consistent with an upper mantle origin of Yellowstone (Christiansen et al., 2002) which may potentially explain the presence of leucite found in SEM-EDS analysis.

Models of a contemporary Yellowstone eruption were created by Mastin et al., (2014) (Figure 20a-d) with temporal parameters lasting 3 days, 1 week, and 1 month, each producing

330 km^3 of volcanic for erupted volume, these values were chosen for this model because the Huckleberry Ridge Tuff, Mesa Falls Tuff, and Lava Creek Tuff expelled about 2450, 280, and 1000 km^3 DRE of magma, but only a fraction of this volume rose in buoyant ash columns that could be carried by winds to form fall deposits; the remainder was emplaced either as ignimbrites that spread along the ground or as intracaldera fill (Figure 23a-d) (Mastin et al., 2014). These models of a contemporary eruption are consistent with ashfall distributions mapped by Izett et al. (1972) furthermore model parameters did not use mapped distributions of ash bed localities while using historical meteorological data from 2001 (Mastin et al., 2014). It can be inferred that paleowinds have not changed significantly from modern wind directions today and that eruption distributions would indeed reach the study area. LCT and HRT appear as likely candidates with HRT seeming like the more probable of the two or conversely the lower clay rich bed represents a HRT and the upper clay rich bed represents LCT.

5.2.3 Long Valley Caldera

Long Valley Caldera is located in Southern California ~ 2,546 km from the study area (Figure 19). Early volcanism was characterized by basaltic eruptions from many vents scattered over a 4000 km^2 area, more silicic lavas evolved and ruptured catastrophically 0.73 Ma ago and 600 km^3 of magma was ejected mainly as ash flows (Hill et al., 1985). The eruption began with a Plinian phase from a vent located in the southeastern portion of the caldera, this phase was immediately followed by emplacement of low-temperature ignimbrites that were erupted from the same vent region (Gardner et al., 1991). The Bishop Tuff (BT) is a crystal-rich rhyolitic tuff that contains up to 30% phenocrysts of quartz, sanidine, plagioclase, biotite, pumiceous shards and Fe-Ti oxides (R. A. Bailey et al., 1976). The Bishop Tuff has an extensive distribution, reaching as far as eastern Nebraska (Figure 20e) (Izett et al., 1970).

The BT seems plausible as it has a distribution that is close to the study area and erupted a large volume of material. The presence of pumiceous shards, quartz, biotite and sanidine were all found in SEM-EDS analysis. One of the most problematic issues is that BT was interpreted to erupt in one cycle (Gardner et al., 1991) which fails to explain the presence of two clay rich horizons. It is also very difficult to explain the presence of leucite, since the BT is a product of silicic volcanism (Hill et al., 1985). The single eruption cycle and conditions inconsistent with the formation of leucite makes BT an unlikely source.

5.2.4 Acoculco Caldera Complex

The Acoculco Caldera Complex (ACC) is located in Southeastern Mexico ~1,980 km away from the study area (Figure 19). The ACC was formed 2.7 Ma in response to an eruption of 127 km^3 of ignimbrite, and has persisted until 0.06 Ma with two ignimbrite eruptions dated at 1.2 and 0.65 Ma (Sosa-Ceballos et al., 2018). The ACC is located within a calc-alkaline volcanic arc produced by subduction of multiple plates under the North American Plate (Avellán et al., 2020). Miocene Rocks located within the volcanic field corroborate this notion as the rocks found were those associated with different stages of the caldera evolution as subduction related calc-alkaline magmas (Avellán et al., 2019). During a period of time associated with late post caldera formation however, the peralkaline magma suite gradually dominated the calc-alkaline suite, resulting in 90 km^3 of magma erupted (Avellán et al., 2019).

The ACC may be a potential source, it is closer than Long Valley Caldera and has eruptions that fit the appropriate time scale; however, the ACC is an unlikely source for multiple reasons, the main one being that the ash fall unit, the Maguey Unit, has not been well mapped or documented (Avellán et al., 2019). It can be inferred from what little is known however that if the ACC was responsible for the pyroclastic deposit that the clay rich horizons formed from, it would have most likely formed from the eruptions from 1.2 and 0.65 Ma. The reason being that these fit the aforementioned temporal constraints and are associated with late post-caldera volcanism and extra caldera volcanism dominated by a peralkaline magma suite (Avellán et al., 2019). The peralkaline magma suite provides a potential source and explanation for the presence of leucite (Gschneidner & Eyring, 1978).

While the ACC provides two eruptive events within the appropriate age range and magmatism consistent with the formation of leucite, it unfortunately lacks documented ash fall units as well as their distribution, and extent to conclude whether this is a likely source for the clay rich horizons. The other eruptions have been studied and although it has been published that the 1.2 Ma ignimbrite produced 27 km^3 of material and dispersed to the northeast and the 0.65 eruption produced 11 km^3 of material (Avellán et al., 2020), nothing concerning pre fall units associated with ignimbrite eruptions has been mentioned. The one fall unit mentioned in the literature is not associated with either eruption (Avellán et al., 2019). This appears to make the ACC an unlikely source, however until more is known it cannot be entirely ruled out either.

Table 13. Eruption units and their time of eruption, location, volume and distance from study area. Eruption units are listed based of their source from the study area. Closest sources for the eruption unit are lised first.

Eruption Unit	Date (Ma)	Location	Volume (km^3)	Distance (km)
Otowi member	1.61	New Mexico	65-187	1,437
Tshirege member	1.22	New Mexico	65-187	1,437
Huckleberry Ridge Tuff	2.1	Wyoming	2,500	1,775
Mesa Falls Tuff	1.3	Idaho	280	1,775
Lava Creek Tuff A	0.6	Wyoming	500	1,775
Lava Creek Tuff B	0.6	Wyoming	500	1,775
Bishop Tuff	0.73	California	600	2,456
Maguey fall unit	1.2	Mexico	N/A	1,980

Figure 19 Map showing where the calderas are in relation to the study area

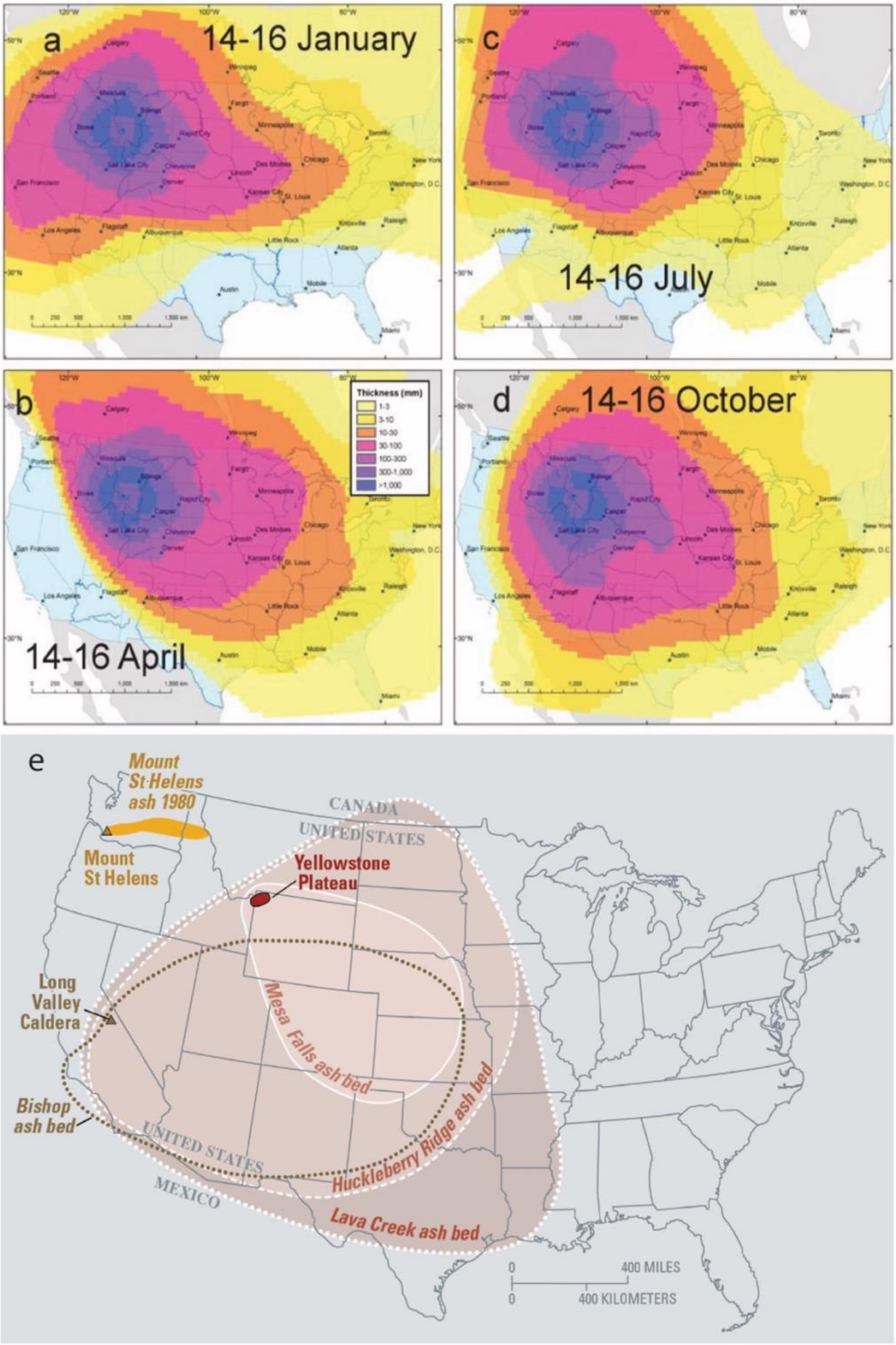

Figure 20 igures (a-d) are modeled Yellowstone eruptions adapted from Mastin et al., (2014) figure (e) is the estimated ash distribution for Yellowstone and Long Valley eruptions based off the appearance of ash in outcrops and cores adapted from Izett & Wilcox (1982).

5.3 Implications for Sediment Paleotransport

XRD analysis revealed the presence of illite-smectite (Figure 13), most likely a product of a precursor smectite that probably underwent illitization. Such smectite was interpreted to represent altered volcanic glass. Identification of additional volcanic minerals and phases using SEM-EDS such as: pumice, sanidine, albite, volcanic glass, and leucite (Table 12) reinforces the idea that the clay rich horizons formed from weathered pyroclastic material. The presence of pumice calls for a large silicic explosive eruption (Klug et al., 2002; Dellino et al., 2005) while microscopic altered volcanic glass suggest the clay horizons are a product of a ash fall deposit (Nakagawa & Ohba, 2002). This indicates that the clay rich horizons are the weathered product of pyroclastic material discharged from a Plinian eruption. Furthermore, the clay rich layers were discovered interbedded within the Upland Complex (UC), which is understood to be a high energy fluvial deposit (Autin, 1996; Lumsden et al., 2016), specifying the environment the ash was deposited in.

A clue to the nature of the eruption is that the two clay rich horizons (Figure 6 and 7) are separated by a sand layer ~1 m in thickness. Clay rich beds separated by a sand layer suggest that these horizons may be the product of two separate eruption episodes or one eruptive episode with a break in between ash fall deposition. Periods between ash fall deposition or cyclical eruptions is a trend consistent with silicic volcanism (Denlinger & Hoblitt, 1999). The break or period between ash fall deposits represented by the sand layer is hard to distinguish. Determining sedimentation rates without theoretical models or the use of geochronology to determine the rate of sediment deposition is complex and requires more data to understand (Szmytkiewicz & Zalewska, 2014).

Volcanic ash transportation models (Mastin et al., 2014) are used to infer the distribution of tephra deposits, while lithofacies analysis and clay mineralogy is used to infer the environment the clay rich horizons were deposited in. The clay rich beds were deposited in the Pliocene to early Pleistocene UC (Self, 1993). This time period would have had a paleoclimate similar to today's climate in this region based on fauna and flora in the UC that resembles that of todays in the southeast, a humid temperate climate (Berry, 1937). Likewise, volcanic ash transport and dispersion modelling of a contemporary caldera forming Yellowstone eruption (330 km^3) with a continent-scale umbrella cloud, and using historical NOAA wind patterns from 2001 as a meteorological input (Mastin et al., 2014), closely matches actual Quaternary volcanic ash distribution maps based on outcrops and cores (Izett & Wilcox, 1982). It can be inferred from eruption models and ash fall distributions that a modelled contemporary Yellowstone eruption would have a distribution analogous to the Yellowstone eruption ~2.6 Ma (Figure 20). The limiting factor being whether the eruption would have an umbrella cloud or not, because the distribution of the tephra is dependent on the growth of the umbrella cloud and ambient wind field (Mastin et al., 2014). The recent Hunga Tonga Ha'apai eruption that occurred on the 15th of January 2022 had an umbrella cloud and was classified as having volcanic explosivity index (VEI) of 6 (Poli & Shapiro, 2022). The Yellowstone eruptions producing the HRT, MFT, and LCT, had a higher VEI of ~8.4 (Fujii et al., 2017) indicating that these eruptions would have produced umbrella clouds to disperse the tephra.

Once the ash was discharged and transported, it was then distributed in the fluvial environment that deposited the UC. The depositional system for the UC has several interpretations which include a shallow braided river system (Potter, 1955), a meander system (Cox et al., 2014), or a fluctuation between both (Cox et al., 2014). Lithofacies analysis of this outcrop is helpful in determining what environment the clay rich beds were deposited in. Sand and gravel facies were organized into gravel bars and bedforms, sandy bars and bedforms, and channels architectural elements. The clay lithofacies characterize floodplain fines typically interpreted as deposits of overbank sheet flows, floodplain ponds and swamps or an abandoned channel element such as a chute or neck cutoff (Table 3) (Dalrymple & James, 2010).

The clay rich horizons may have been deposited in a meandering river floodplains as overflow of floodwaters transports material from the channel onto the floodplain, eventually draining into chutes and meander scroll swales in the lower part of the floodplain (Zwoliński, 1992). Floodplain clays are continuous for large distances, typically contain calcareous deposits, and pedogenetic and bioturbation features are abundant (Ielpi & Ghinassi, 2014), which were not observed within the clay rich horizons of interest. Furthermore, coarse gravels are not found on floodplains (Knighton, 1998), and the absence of organic rich deposits makes a swamp environment unlikely as well (Boggs, 2001).

The clay rich horizons could be interpreted as an abandoned channel element such as an abandoned chute, channel, or neck cutoff. Abandoned channel meanders are known as sites of clay accumulation (Gilvear & Bravard, 1996) which collects in the channel after it is temporarily occupied by flood waters (Lindsey et al., 1998). Meander loops abandon gradually (chute-cut off) or suddenly (neck-cutoff), during chute cut-off which can explain the difference in flow regime between the gravel and sand layers and the clay layer.

During chute-cut off, the river gradually reoccupies an old swale, and simultaneously flow gradually decreases in the main channel, eventually leading to gradual abandonment thus resulting in the development of a thick sequence of low flow sedimentary structures - essentially ripple cross-lamination (Posamentier & Walker, 2006). Neck cut-off involves the breaching of a neck between two meanders, and the sudden cut-off of an entire meander loop with sandy sediment, results in a sequence of deposits dominated by flood- introduced silts and muds (Walker, 1976). This sudden change appears like a potential scenario because of the clay layers distinct contact with the sand layer below it. Alternatively, these clay rich layers may represent abandoned bar chutes, such as the ones found in the South Platte River in Colorado, filled with fine grained sediment in gravel deposits. Abandoned bar chutes, tend to be oriented subparallel to stream flow, hundreds of meters in length, with layers varying in thickness potentially reaching up to 60 cm in thickness (Lindsey et al., 1998) similar to the clay rich beds observed in Drum pit.

The fundamental processes that controls whether a river has a braided or meandering pattern are not completely understood, but braiding is favored by rapid discharge fluctuations, of a greater absolute magnitude than in meandering river and higher slopes, a coarser load, and more easily erodible banks (Walker, 1976). It is therefore difficult to discern whether the clay was deposited in a meandering or braided channel. The gravel and sand lithofacies indicate a high energy environment and could potentially be interpreted as a debris flow in an alluvial fan environment, however there is no indication of higher slopes in Drum pit. It is however possible there may have been some relief at the top of UC before it was covered by eolian silt.

The lithofacies analysis reveals that the ash was deposited in and adjacent to a high energy fluvial system. Consequently, large volumes of fine-grained materials would drain into the fluvial system and mix with other fine-grained material. The resulting mix of fine-grained sediment was most likely deposited in a flooding event. The lithofacies analysis suggests that this may have happened as an abandoned channel or neck-cutoff deposit. After the sudden deposition of the clay beds the load then transition to largely coarse grained sandy material This was followed by another pulse of fine sediment incursion leading to the deposition of another clay layer. This was then followed by potential gravel debris flow or turbid flow deposits as a result of flooding or channel reactivation.

Chapter 6

Conclusion

XRD analysis of the clay fraction identified dominant illite-smectite phases in three of the four clay rich beds and kaolinite in the gravel and sand layers and one clay rich horizon. The smectite precursor of illite-smectite was found to be a product of volcanic glass alteration. SEM-EDS investigation identified igneous phases such as sanidine and pumice, which indicate a potentially explosive volcanic origin. The Valles, Yellowstone, Long Valley and Acoculco Calderas were all considered plausable sources based on temporal constraints established from overlying and underlying sediment, mineralogy, estimated distribution, phase chemistry, and the distance from the study area. Paleowinds were interpreted to be similar to contemporary wind directions based off of Yellowstone eruption models and mapped units of tephra deposits .

- Precursor smectite in the clay was the result of the alteration of volcanic glass.
- Alteration of smectite to illite-smectite occurred through K-fixation as a result of wetting-drying successions from cyclical flooding and rain. K-rich volcanic rocks such as sanidine and leucite provided a source of K for K-fixation to occur.
- Pronounced kaolinite basal reflexes in XRD traces in gravel and sand layers indicates that kaolinite precipitated from the percolation of fluid within the outcrop, likely within a moist and subtropical climate similar to today’s climate.
- Less pronounced mica/illite peaks observed in XRD traces were likely detrital in nature

- The top clay rich horizon in the eastern outcrop exhibited a mineralogy distinct from the other clay rich horizons and produced XRD traces identical to the adjacent gravel and sand layersin the eastern outcrop. This may be due to material being mined away from the gravel layer above it resulting in kaolinite being mobilized as a percolating product from late modern fluids.
- Huckleberry Ridge Tuff and Lava Creek Tuff are the most likely tephra sources because the tuffs are the appropriate age, have multiple episodic eruptions, and have large discharge volumes and distributions.
- The tephra was interpreted to have been deposited in a high energy fluvial environment where it was mixed with other fine-grained sediment and then concentrated and deposited into an abandoned channels during a flooding event.

Future Geochemical Analysis

The results from XRD and SEM-EDS analysis was helpful in distinguishing multiple sources the clay beds may have originated from. This analysis by itself however, is not enough to discern definitively the provenance. Major and minor trace element analysis would be important future work for a more certain provenance. Airborne tephra deposits produced by explosive volcanism can preserve an extensive record of magmatism (Hannon et al., 2021). These tephra deposits can preserve the original geochemistry of their source magmas (Hong et al., 2019). This is particularly true for immobile elements (e.g. Ti, Zr, Th, and Nb) and rare earth elements (REE; Zielinski, 1982)

Volcanic ash alters rapidly when exposed to water, and results in the restructuring of amorphous volcanic glass into clay minerals, elemental mobility during devitrification strongly influences most cations (Hannon et al., 2021). However, the retention of many immobile elements makes the use of classical discrimination diagrams and direct comparisons possible (Jones et al., 2016). Diagrams that would be helpful for distinguishing provenance in future work includes: REE spider diagrams normalized to chondrite compared to that of Yellowstone LCT and HRT as well as comparisons with Valles caldera bandelier tuff, and BT from Long valley caldera. Trace element concentrations/ratios would be beneficial in discriminating geochemical trends among clay layers through time and discern magmatic processes, additionally a chemical weathering index may also be practical.

List of References

Altaner, S. P. (1997). Comparison of Structural Models of Mixed-Layer Illite/Smectite and Reaction Mechanisms of Smectite Illitization. *Clays and Clay Minerals*, *45*(4), 517–533. https://doi.org/10.1346/CCMN.1997.0450404

Anthony, J. W. (Ed.). (1990). *Handbook of mineralogy*. Mineral Data Pub.

Autin, W. J. (1996). Pleistocene stratigraphy in the southern Lower Mississippi Valley. *Engineering Geology*, *45*(1–4), 87–112. https://doi.org/10.1016/S0013-7952(96)00009-9

Autin, W. J., Burns, S. F., Miller, B. J., Saucier, R. T., & Snead, J. I. (1991). Quaternary geology of the Lower Mississippi Valley. In R. B. Morrison (Ed.), *Quaternary Nonglacial Geology* (pp. 547–582). Geological Society of America. https://doi.org/10.1130/DNAG-GNA-K2.547

Avellán, D. R., Macías, J. L., Layer, P. W., Cisneros, G., Sánchez-Núñez, J. M., Gómez-Vasconcelos, M. G., Pola, A., Sosa-Ceballos, G., García-Tenorio, F., Reyes Agustín, G., Osorio-Ocampo, S., García-Sánchez, L., Mendiola, I. F., Marti, J., López-Loera, H., & Benowitz, J. (2019). Geology of the late Pliocene – Pleistocene Acoculco caldera complex, eastern Trans-Mexican Volcanic Belt (México). *Journal of Maps*, *15*(2), 8–18. https://doi.org/10.1080/17445647.2018.1531075

Avellán, D. R., Macías, J. L., Layer, P. W., Sosa-Ceballos, G., Gómez-Vasconcelos, M. G., Cisneros-Máximo, G., Sánchez-Núñez, J. M., Martí, J., García-Tenorio, F., López-Loera, H., Pola, A., & Benowitz, J. (2020). Eruptive chronology of the Acoculco caldera complex – A resurgent caldera in the eastern Trans-Mexican Volcanic Belt (México).

Journal of South American Earth Sciences, *98*, 102412. https://doi.org/10.1016/j.jsames.2019.102412

Badurina, L., Šegvić, B., Mandic, O., & Slovenec, D. (2021). Miocene tuffs from the Dinarides and Eastern Alps as proxies of the Pannonian Basin lithosphere dynamics and tropospheric circulation patterns in Central Europe. *Journal of the Geological Society*, *178*(6), jgs2020-262. https://doi.org/10.1144/jgs2020-262

Bailey, D. K. (1964). Crustal warping-a possible tectonic control of alkaline magmatism. *Journal of Geophysical Research*, *69*(6), 1103–1111. https://doi.org/10.1029/JZ069i006p01103

Bailey, R. A., Dalrymple, G. B., & Lanphere, M. A. (1976). Volcanism, structure, and geochronology of Long Valley Caldera, Mono County, California. *Journal of Geophysical Research*, *81*(5), 725–744. https://doi.org/10.1029/JB081i005p00725

Balashov, Yu. A., & Glaznev, V. N. (2006). Cycles of alkaline magmatism. *Geochemistry International*, *44*(3), 274–285. https://doi.org/10.1134/S0016702906030050

Baldwin, J. N., Witter, R. C., Vaughn, J. D., Harris, J. B., Sexton, J. L., Lake, M., Forman, S. L., & Barron, A. D. (2006). Geological Characterization of the Idalia Hill Fault Zone and Its Structural Association with the Commerce Geophysical Lineament, Idalia, Missouri. *Bulletin of the Seismological Society of America*, *96*(6), 2281–2303. https://doi.org/10.1785/0120050136

Bauluz, B., Mayayo, M. J., Yuste, A., & González López, J. M. (2008). Genesis of kaolinite from Albian sedimentary deposits of the Iberian Range (NE Spain): Analysis by XRD, SEM and TEM. *Clay Minerals*, *43*(3), 459–475. https://doi.org/10.1180/claymin.2008.043.3.10

Behrman, C., Van Arsdale, R., Kwon, Y., Stockslager, K., Leverett, D., & Lumsden, D. (2019). Drone Geologic Mapping of an Active Sand and Gravel Quarry, Desoto County, Mississippi. *Drones*, *3*(3), 57. https://doi.org/10.3390/drones3030057

Berner, R. A. (1971). *Principles of chemical sedimentology*. McGraw-Hill.

Berry, E. W. (1937). Tertiary Floras of Eastern North America. *Botanical Review*, *3*(1), 31–46. JSTOR.

Berti, D., Slowey, N. C., Yancey, T. E., & Deng, Y. (2022). Rare earth nanominerals in bentonite deposits of the Eocene Texas coastal plains. *Applied Clay Science*, *216*, 106373. https://doi.org/10.1016/j.clay.2021.106373

Boggs, S. (2001). *Principles of sedimentology and stratigraphy* (3rd ed). Prentice Hall.

Brady, N. C., & Weil, R. R. (2008). *The nature and properties of soils* (14th ed). Pearson Prentice Hall.

Braile, L. W., Hinze, W. J., Keller, G. R., Lidiak, E. G., & Sexton, J. L. (1986). Tectonic development of the New Madrid rift complex, Mississippi embayment, North America. *Tectonophysics*, *131*(1–2), 1–21. https://doi.org/10.1016/0040-1951(86)90265-9

Brigatti, M. F. (1983). Relationships between composition and structure in Fe-rich smectites. *Clay Minerals*, *18*(02), 177–186. https://doi.org/10.1180/claymin.1983.018.2.06

Brindley, G. W. (1952). Identification of Clay Minerals by X-ray Diffraction Analysis. *Clays and Clay Minerals*, *1*(1), 119–129. https://doi.org/10.1346/CCMN.1952.0010116

Brown, N. D., & Forman, S. L. (2012). Evaluating a SAR TT-OSL protocol for dating fine-grained quartz within Late Pleistocene loess deposits in the Missouri and Mississippi river valleys, United States. *Quaternary Geochronology*, *12*, 87–97. https://doi.org/10.1016/j.quageo.2012.06.008

Burke, K., & Dewey, J. F. (1973). Plume-Generated Triple Junctions: Key Indicators in Applying Plate Tectonics to Old Rocks. *The Journal of Geology*, *81*(4), 406–433. https://doi.org/10.1086/627882

Christiansen, R. L. (1984). *Yellowstone magmatic evolution: Its bearing on understanding large-volume explosive volcanism*. 89–95.

Christiansen, R. L. (2001). *The Quaternary and Pliocene Yellowstone Plateau Volcanic Field of Wyoming, Idaho, and Montana*. United States Government Printing Office.

Christiansen, R. L., Foulger, G. R., & Evans, J. R. (2002). Upper-mantle origin of the Yellowstone hotspot. *Geological Society of America Bulletin*, *114*(10), 1245–1256. https://doi.org/10.1130/0016-7606(2002)114<1245:UMOOTY>2.0.CO;2

Cook, G. W., Wolff, J. A., & Self, S. (2016). Estimating the eruptive volume of a large pyroclastic body: The Otowi Member of the Bandelier Tuff, Valles caldera, New Mexico. *Bulletin of Volcanology*, *78*(2), 10. https://doi.org/10.1007/s00445-016-1000-0

Cox, R. T. (1988). Evidence of Quatermary Ground Tilting Associated with the Reelfoot Rift Zone, Northeast Arkansas. *Southeastern Geology*, *28*, 211–224.

Cox, R. T., Lumsden, D. N., & Van Arsdale, R. B. (2014). Possible Relict Meanders of the Pliocene Mississippi River and Their Implications. *The Journal of Geology*, *122*(5), 609–622. https://doi.org/10.1086/676974

Cox, R. T., & Van Arsdale, R. B. (1997). Hotspot origin of the Mississippi embayment and its possible impact on contemporary seismicity. *Engineering Geology*, *46*(3–4), 201–216. https://doi.org/10.1016/S0013-7952(97)00003-3

Cox, R. T., & Van Arsdale, R. B. (2002). The Mississippi Embayment, North America: A first order continental structure generated by the Cretaceous superplume mantle event.

Journal of Geodynamics, *34*(2), 163–176. https://doi.org/10.1016/S0264-3707(02)00019-4

Crowe, B. M., Linn, G. W., Heiken, G., & Bevier, M. L. (1978). *Stratigraphy of the Bandelier Tuff in the Pajarito Plateau. Applications to waste management* (LA-7225-MS, 6870764; p. LA-7225-MS, 6870764). https://doi.org/10.2172/6870764

Cruz-Uribe, A. M., Marschall, H. R., Gaetani, G. A., & Le Roux, V. (2018). Generation of alkaline magmas in subduction zones by partial melting of mélange diapirs—An experimental study. *Geology*, *46*(4), 343–346. https://doi.org/10.1130/G39956.1

Cushing, E. M., Boswell, E. H., & Hosman, R. L. (1964). General Geology of the Mississippi Embayment. *Geological Survey Professional Paper*, *448-B*.

Dai, S., Ward, C. R., Graham, I. T., French, D., Hower, J. C., Zhao, L., & Wang, X. (2017). Altered volcanic ashes in coal and coal-bearing sequences: A review of their nature and significance. *Earth-Science Reviews*, *175*, 44–74. https://doi.org/10.1016/j.earscirev.2017.10.005

Dalrymple, R. W., & James, N. P. (2010). *Facies models 4*. Geological association of Canada.

Davis, J. A., & Hayes, K. F. (Eds.). (1987). *Geochemical Processes at Mineral Surfaces* (Vol. 323). American Chemical Society. https://doi.org/10.1021/bk-1987-0323

de la Fuente, S., Cuadros, J., Fiore, S., & Linares, J. (2000). ELECTRON MICROSCOPY STUDY OF VOLCANIC TUFF ALTERATION TO ILLITE-SMECTITE UNDER HYDROTHERMAL CONDITIONS. *Clays and Clay Minerals*, *48*(3), 339–350.

Dellino, P., Mele, D., Bonasia, R., Braia, G., La Volpe, L., & Sulpizio, R. (2005). The analysis of the influence of pumice shape on its terminal velocity. *Geophysical Research Letters*, *32*(21), L21306. https://doi.org/10.1029/2005GL023954

Denlinger, R. P., & Hoblitt, R. P. (1999). Cyclic eruptive behavior of silicic volcanoes. *Geology*, *27*(5), 459. https://doi.org/10.1130/0091-7613(1999)027<0459:CEBOSV>2.3.CO;2

Denton, J. S., Tuffen, H., Gilbert, J. S., & Odling, N. (2009). The hydration and alteration of perlite and rhyolite. *Journal of the Geological Society*, *166*(5), 895–904. https://doi.org/10.1144/0016-76492008-007

Dockery, D. T., & Thompson, D. E. (2016). *The geology of Mississippi*. University Press of Mississippi.

Drits, V. A., & Sakharov, B. A. (1976). X-ray structural analysis of mixed layer minerals. *Transactions of the Academy of Sciences USSR*, *295*, 1–252.

Ece, Ö. I. (1999). Clay Mineralogy and Occurrence of Ferrian Smectites between Serpentinite Saprolites and Basalts in Biga Peninsula, Northwest Turkey. *Clays and Clay Minerals*, *47*(3), 241–251. https://doi.org/10.1346/CCMN.1999.0470301

Edgar, A. D. (1987). The genesis of alkaline magmas with emphasis on their source regions: Inferences from experimental studies. *Geological Society, London, Special Publications*, *30*(1), 29–52. https://doi.org/10.1144/GSL.SP.1987.030.01.04

Ervin, C. P., & McGinnis, L. D. (1975). Reelfoot Rift: Reactivated Precursor to the Mississippi Embayment. *Geological Society of America Bulletin*, *86*(9), 1287. https://doi.org/10.1130/0016-7606(1975)86<1287:RRRPTT>2.0.CO;2

Ferrage, E., Vidal, O., Mosser-Ruck, R., Cathelineau, M., & Cuadros, J. (2011). A reinvestigation of smectite illitization in experimental hydrothermal conditions: Results from X-ray diffraction and transmission electron microscopy. *American Mineralogist*, *96*(1), 207–223. https://doi.org/10.2138/am.2011.3587

Florence, A., Ransom, M., & Mengel, D. (2017). Potassium Fixation by Oxidized and Reduced Forms of Phyllosilicates. *Soil Science Society of America Journal*, *81*(5), 1247–1255. https://doi.org/10.2136/sssaj2016.12.0420

Forman, S. L., & Pierson, J. (2002). Late Pleistocene luminescence chronology of loess deposition in the Missouri and Mississippi river valleys, United States. *Palaeogeography, Palaeoclimatology, Palaeoecology*, *186*(1–2), 25–46. https://doi.org/10.1016/S0031-0182(02)00440-6

Frost, R. L., & Kristof, J. (2004). Raman and Infrared Spectroscopic Studies of Kaolinite Surfaces Modified by Intercalation. In *Interface Science and Technology* (Vol. 1, pp. 184–215). Elsevier. https://doi.org/10.1016/S1573-4285(04)80041-3

Fujii, Y., Kodama, J., Fukuda, D., & Dassanayake, A. (2017). *Prevention of catastrophic volcanic eruptions*. *2017*, 211–215.

Galán, E., & Ferrell, R. E. (2013). Genesis of Clay Minerals. In *Developments in Clay Science* (Vol. 5, pp. 83–126). Elsevier. https://doi.org/10.1016/B978-0-08-098258-8.00003-1

Gardner, J. E., Sigurdsson, H., & Carey, S. N. (1991). Eruption dynamics and magma withdrawal during the Plinian Phase of the Bishop Tuff Eruption, Long Valley Caldera. *Journal of Geophysical Research*, *96*(B5), 8097. https://doi.org/10.1029/91JB00257

Gilvear, D., & Bravard, J.-P. (1996). Geomorphology of temperate rivers. In G. E. Petts & C. Amoros (Eds.), *The Fluvial Hydrosystems* (pp. 68–97). Springer Netherlands. https://doi.org/10.1007/978-94-009-1491-9_4

Gittins, J. (2015). Chapter 12. THE FELDSPATHOIDAL ALKALINE ROCKS. In H. S. Yoder, *Evolution of the Igneous Rocks: Fiftieth Anniversary Perspectives* (pp. 351–390). Princeton University Press. https://doi.org/10.1515/9781400868506-013

Goff, F., & Grigsby, C. O. (1982). Valles Caldera geothermal systems, New Mexico, U.S.A. *Journal of Hydrology*, *56*(1–2), 119–136. https://doi.org/10.1016/0022-1694(82)90061-0

Gray, J. L., & Ferguson, D. V. (1977). Soil Survey of Craighead County. In *Soil Survey of Craighead County* (p. 68). United States Department of Agriculture.

Grimley, D. (2003). Modern, Sangamon and Yarmouth soil development in loess of unglaciated southwestern Illinois. *Quaternary Science Reviews*, *22*(2–4), 225–244. https://doi.org/10.1016/S0277-3791(02)00039-2

Gschneidner, K. A., & Eyring, L. (Eds.). (1978). *Handbook on the physics and chemistry of rare earths*. North-Holland ; sole distributors for the U.S.A. and Canada, Elsevier North-Holland.

Guccione, M. J., Prior, W. L., & E.M. Rutledge. (1986). *The Tertiary and Quaternary Geology of Crowley's Ridge: A Guidebook*. Arkansas Geological Commission.

Haldar, S. K. (2020). Chapter 5—Igneous rocks. In S. K. Haldar (Ed.), *Introduction to Mineralogy and Petrology (Second Edition)* (pp. 159–186). Elsevier. https://doi.org/10.1016/B978-0-12-820585-3.00005-3

Haldar, S. K., & Tišljar, J. (2014). *Introduction to Mineralogy and Petrology*. Elsevier. https://doi.org/10.1016/C2012-0-03337-6

Hall, G. F. (1983). Pedology and Geomorphology. In *Developments in Soil Science* (Vol. 11, pp. 117–140). Elsevier. https://doi.org/10.1016/S0166-2481(08)70600-7

Hannon, J. S., Dietsch, C., & Huff, W. D. (2021). Trace-element and Sr and Nd isotopic geochemistry of Cretaceous bentonites in Wyoming and South Dakota tracks magmatic processes during eastward migration of Farallon arc plutons. *GSA Bulletin*, *133*(7–8), 1542–1559. https://doi.org/10.1130/B35796.1

Hayward, O. T., Geological Society of America, & South-Central Section. (1988). *Centennial field guide. Vol. 4 Vol. 4*. Geological Society of America.

Hill, D. P., Bailey, R. A., & Ryall, A. S. (1985). Active tectonic and magmatic processes beneath Long Valley Caldera, eastern California: An overview. *Journal of Geophysical Research, 90*(B13), 11111. https://doi.org/10.1029/JB090iB13p11111

Hong, H., Fang, Q., Zhao, L., Schoepfer, S., Wang, C., Gong, N., Li, Z., & Chen, Z.-Q. (2017). Weathering and alteration of volcanic ashes in various depositional settings during the Permian-Triassic transition in South China: Mineralogical, elemental and isotopic approaches. *Palaeogeography, Palaeoclimatology, Palaeoecology, 486*, 46–57. https://doi.org/10.1016/j.palaeo.2016.12.033

Hong, H., Zhao, L., Fang, Q., Algeo, T. J., Wang, C., Yu, J., Gong, N., Yin, K., & Ji, K. (2019). Volcanic sources and diagenetic alteration of Permian–Triassic boundary K-bentonites in Guizhou Province, South China. *Palaeogeography, Palaeoclimatology, Palaeoecology, 519*, 141–153. https://doi.org/10.1016/j.palaeo.2018.01.019

Huff, W. D. (2016). K-bentonites: A review. *American Mineralogist, 101*(1), 43–70. https://doi.org/10.2138/am-2016-5339

Huggett, J. M. (2005). Low-temperature illitization of smectite in the late eocene and early oligocene of the Isle of Wight (Hampshire basin), U.K. *American Mineralogist, 90*(7), 1192–1202. https://doi.org/10.2138/am.2005.1674

Ielpi, A., & Ghinassi, M. (2014). Planform architecture, stratigraphic signature and morphodynamics of an exhumed Jurassic meander plain (Scalby Formation, Yorkshire, UK). *Sedimentology, 61*(7), 1923–1960. https://doi.org/10.1111/sed.12122

Islam, Md. R., Stuart, R., Risto, A., & Vesa, P. (2002). Mineralogical changes during intense chemical weathering of sedimentary rocks in Bangladesh. *Journal of Asian Earth Sciences*, *20*(8), 889–901. https://doi.org/10.1016/S1367-9120(01)00078-5

Izett, G. A., & Wilcox, R. E. (1982). *Map showing localities and inferred distributions of the Huckleberry Ridge, Mesa Falls, and Lava Creek ash beds (Pearlette family ash beds) of Pliocene and Pleistocene age in the western United States and southern Canada*. https://doi.org/10.3133/i1325

Izett, G. A., Wilcox, R. E., & Borchardt, G. A. (1972). Correlation of a Volcanic Ash bed in Pleistocene Deposits near Mount Blanco, Texas, with the Guaje Pumice Bed of the Jemez Mountains, New Mexico. *Quaternary Research*, *2*(4), 554–578. https://doi.org/10.1016/0033-5894(72)90091-9

Izett, G. A., Wilcox, R. E., Powers, H. A., & Desborough, G. A. (1970). The Bishop Ash Bed, a Pleistocene Marker Bed in the Western United States. *Quaternary Research*, *1*(1), 121–132. https://doi.org/10.1016/0033-5894(70)90014-1

John W. Shelton. (1964). Authigenic Kaolinite in Sandstone. *SEPM Journal of Sedimentary Research, Vol. 34*. https://doi.org/10.1306/74D70FDD-2B21-11D7-8648000102C1865D

Kano, K. (2003). Subaqueous pumice eruptions and their products: A review. In J. D. L. White, J. L. Smellie, & D. A. Clague (Eds.), *Geophysical Monograph Series* (Vol. 140, pp. 213–229). American Geophysical Union. https://doi.org/10.1029/140GM14

K.F. Boyd, & Schumm, S. A. (1995). *Geomorphic Evidence of deformation in the northern part of the New Madrid seismic zone* (Professional Paper) [Professional Paper].

Klug, C., K., C., & C., B. (2002). Structure and physical characteristics of pumice from the climactic eruption of Mount Mazama (Crater Lake), Oregon. *Bulletin of Volcanology*, *64*(7), 486–501. https://doi.org/10.1007/s00445-002-0230-5

Kretz, R. (1983). Symbols for rock-forming minerals. *American Mineralogist*, *68*(1–2), 277–279.

Lindsey, D. A., Taggart, J. E., & Meeker, G. P. (1998). Gravel deposits of the South Platte River Valley north of Denver, Colorado Part C: Description, composition, and origin of clay lenses in gravel. *U.S. Geologic Survey*, *OPEN-FILE REPORT 98-148-C*.

Lumsden, D. N., Cox, R. T., Van Arsdale, R. B., & Cupples, W. B. (2016). Petrology of Pliocene Mississippi River Alluvium: Provenance Implications. *The Journal of Geology*, *124*(4), 501–517. https://doi.org/10.1086/686997

Maat, P. B., & Johnson, W. C. (1996). Thermoluminescence and new 14C age estimates for late quaternary loesses in southwestern Nebraska. *Geomorphology*, *17*(1–3), 115–128. https://doi.org/10.1016/0169-555X(95)00099-Q

Mastin, L. G., Van Eaton, A. R., & Lowenstern, J. B. (2014). Modeling ash fall distribution from a Yellowstone supereruption. *Geochemistry, Geophysics, Geosystems*, *15*(8), 3459–3475. https://doi.org/10.1002/2014GC005469

Mazzi, F., Galli, E., & Gottardi, G. (1976). The crystal structure of tetragonal leucite. *American Mineralogist*, *61*(1–2), 108–115.

McIntosh, J. A., Tabor, N. J., & Rosenau, N. A. (2021). Mixed-Layer Illite-Smectite in Pennsylvanian-Aged Paleosols: Assessing Sources of Illitization in the Illinois Basin. *Minerals*, *11*(2), 108. https://doi.org/10.3390/min11020108

Meissner, C. R. (1984). Stratigraphic Framework and Distribution of Lignite on Crowley’s Ridge, Arkansas. *United States Geological Survey*.

Miall, A. (2013). *The Geology of Fluvial Deposits: Sedimentary Facies, Basin Analysis, and Petroleum Geology*. Springer Berlin / Heidelberg. https://public.ebookcentral.proquest.com/choice/publicfullrecord.aspx?p=5591026

Miall, A. D. (1996). *The geology of fluvial deposits: Sedimentary facies, basin analysis, and petroleum geology*. Springer.

Mohammadnia, M., & Kowsar, S. A. (2003). Clay Translocation in the Artificial Recharge of a Groundwater System in the Southern Zagros Mountains, Iran. *Mountain Research and Development*, *23*(1), 50–55. https://doi.org/10.1659/0276-4741(2003)023[0050:CTITAR]2.0.CO;2

Mooney, W. D., Andrews, M. C., Ginzburg, A., Peters, D. A., & Hamilton, R. M. (1983). Crustal structure of the northern mississippi embayment and a comparison with other continental rift zones. *Tectonophysics*, *94*(1–4), 327–348. https://doi.org/10.1016/0040-1951(83)90023-9

Moore, D. M., & Reynolds, R. C. (1997). *X-ray diffraction and the identification and analysis of clay minerals* (2nd ed). Oxford University Press.

Muhs, D. R., & Bettis, E. A. (2000). Geochemical Variations in Peoria Loess of Western Iowa Indicate Paleowinds of Midcontinental North America during Last Glaciation. *Quaternary Research*, *53*(1), 49–61. https://doi.org/10.1006/qres.1999.2090

Nakagawa, M., & Ohba, T. (2002). *Minerals in Volcanic Ash 1: Primary Minerals and Volcanic Glass*. *6*.

Odom, W., Hofmann, F., Van Arsdale, R., & Granger, D. (2020). New 26Al/10Be and (U-Th)/He constraints on the age of the Upland Complex, central Mississippi River Valley. *Geomorphology*, *371*, 107448. https://doi.org/10.1016/j.geomorph.2020.107448

Pal, S., Shrivastava, J. P., & Mukhopadhyay, S. K. (2015). Mineral chemistry of clays associated with the Late Cretaceous-early Palaeogene succession of the Um-Sohryngkew river section of Meghalaya, India: Palaeoenvironmental inferences and K/Pg transition. *Journal of the Geological Society of India*, *86*(6), 631–647. https://doi.org/10.1007/s12594-015-0355-8

Petit, S., Caillaud, J. ., Righi, D., Madejová, J. ., Elsass, F., & Köster, H. M. (2002). Characterization and crystal chemistry of an Fe-rich montmorillonite from Ölberg, Germany. *Clay Minerals*, *37*(2), 283–297. https://doi.org/10.1180/0009855023720034

Pirajno, F. (2004). Hotspots and mantle plumes: Global intraplate tectonics, magmatism and ore deposits. *Mineralogy and Petrology*, *82*(3–4), 183–216. https://doi.org/10.1007/s00710-004-0046-4

Poli, P., & Shapiro, N. M. (2022). Rapid Characterization of Large Volcanic Eruptions: Measuring the Impulse of the Hunga Tonga Ha'apai Explosion From Teleseismic Waves. *Geophysical Research Letters*, *49*(8). https://doi.org/10.1029/2022GL098123

Pollastro, R. M. (1985). Mineralogical and Morphological Evidence for the Formation of Illite at the Expense of Illite/Smectite. *Clays and Clay Minerals*, *33*(4), 265–274. https://doi.org/10.1346/CCMN.1985.0330401

Posamentier, H. W., & Walker, R. G. (Eds.). (2006). *Facies Models Revisited*. SEPM (Society for Sedimentary Geology). https://doi.org/10.2110/pec.06.84

Potter, P. E. (1955). The Petrology and Origin of the Lafayette Gravel Part 2. Geomorphic History. *The Journal of Geology*, *63*(2), 115–132. https://doi.org/10.1086/626238

Pye, K. (1995). The nature, origin and accumulation of loess. *Quaternary Science Reviews*, *14*(7–8), 653–667. https://doi.org/10.1016/0277-3791(95)00047-X

Rich, C. I. (1957). Determination of (060) Reflections of Clay Minerals by Means of Counter Type X-Ray Diffraction Instruments. *American Mineralogist*, *42*(7–8), 569–570.

Righi, D. (1993). Characterization of Hydroxy-Interlayered Vermiculite and Illite/Smectite Interstratified Minerals from the Weathering of Chlorite in a Cryorthod. *Clays and Clay Minerals*, *41*(4), 484–495. https://doi.org/10.1346/CCMN.1993.0410409

Rivera, T. A., Schmitz, M. D., Jicha, B. R., & Crowley, J. L. (2016). Zircon Petrochronology and ^{40} Ar/ ^{39} Ar Sanidine Dates for the Mesa Falls Tuff: Crystal-scale Records of Magmatic Evolution and the Short Lifespan of a Large Yellowstone Magma Chamber. *Journal of Petrology*, egw053. https://doi.org/10.1093/petrology/egw053

Rutledge, E. M., Guccione, M. J., Markewich, H. W., Wysocki, D. A., & Ward, L. B. (1996a). Loess stratigraphy of the Lower Mississippi Valley. *Engineering Geology*, *45*(1–4), 167–183. https://doi.org/10.1016/S0013-7952(96)00012-9

Rutledge, E. M., Guccione, M. J., Markewich, H. W., Wysocki, D. A., & Ward, L. B. (1996b). Loess stratigraphy of the Lower Mississippi Valley. *Engineering Geology*, *45*(1–4), 167–183. https://doi.org/10.1016/S0013-7952(96)00012-9

Sandler, A., & Harlavan, Y. (2006). Early diagenetic illitization of illite-smectite in Cretaceous sediments (Israel): Evidence from K-Ar dating. *Clay Minerals*, *41*(2), 637–658. https://doi.org/10.1180/0009855064120210

Schultz, L. G. (1969). Lithium and Potassium Absorption, Dehydroxylation Temperature, and Structural Water Content of Aluminous Smectites*. *Clays and Clay Minerals*, *17*(3), 115–149. https://doi.org/10.1346/CCMN.1969.0170302

Schultz, L. G. (1978). *Professional Paper* (Mixed-Layer Clay in the Pierre Shale and Equivalent Rocks, Northern Great Plains Region) [Professional Paper].

Šegvić, B., Mileusnić, M., Aljinović, D., Vranjković, A., Mandic, O., Pavelić, D., Dragičević, I., & Ferreiro Mählmann, R. (2014). Magmatic provenance and diagenesis of Miocene tuffs from the Dinaride Lake System (the Sinj Basin, Croatia). *European Journal of Mineralogy*, *26*(1), 83–101. https://doi.org/10.1127/0935-1221/2013/0025-2350

Self, R. P. (1993). Late Tertiary to early Quaternary sedimentation in the Gulf coastal plain and lower Mississippi valley. *Southeastern Geology*, *33*(2), 99–110.

Self, S., Goff, F., Gardner, J. N., Wright, J. V., & Kite, W. M. (1986). Explosive rhyolitic volcanism in the Jemez Mountains: Vent locations, caldera development and relation to regional structure. *Journal of Geophysical Research*, *91*(B2), 1779. https://doi.org/10.1029/JB091iB02p01779

Self, S., Heiken, G., Sykes, M. L., Wohletz, K., Fisher, R. V., & Dethier, D. P. (1996). *Field excursions to the Jemez Mountain, New Mexico*. Bulletin of the New Mexico Bureau of Geology & Mineral Resources.

Shamloo, H. I., & Till, C. B. (2019). Decadal transition from quiescence to supereruption: Petrologic investigation of the Lava Creek Tuff, Yellowstone Caldera, WY. *Contributions to Mineralogy and Petrology*, *174*(4), 32. https://doi.org/10.1007/s00410-019-1570-x

Sherman, G. D., Ikawa, H., Uehara, G., & Okazaki, E. (1962). *Types of occurrence of nontronite and nontronite-like minerals in soils*.

Smith, R. B., & Braile, L. W. (1994). The Yellowstone hotspot. *Journal of Volcanology and Geothermal Research*, *61*(3–4), 121–187. https://doi.org/10.1016/0377-0273(94)90002-7

Smith, R. L., & Bailey, R. A. (1968). Resurgent Cauldrons. In *Geological Society of America Memoirs* (Vol. 116, pp. 613–662). Geological Society of America. https://doi.org/10.1130/MEM116-p613

Smith, R. L., & Ross. (1970). *Geologic map of the Jemez Mountains, New Mexico*. https://doi.org/10.3133/i571

Sosa-Ceballos, G., Macías, J. L., Avellán, D. R., Salazar-Hermenegildo, N., Boijseauneau-López, M. E., & Pérez-Orozco, J. D. (2018). The Acoculco Caldera Complex magmas: Genesis, evolution and relation with the Acoculco geothermal system. *Journal of Volcanology and Geothermal Research*, *358*, 288–306. https://doi.org/10.1016/j.jvolgeores.2018.06.002

Środoń, J. (2006). Chapter 12.2 Identification and Quantitative Analysis of Clay Minerals. In *Developments in Clay Science* (Vol. 1, pp. 765–787). Elsevier. https://doi.org/10.1016/S1572-4352(05)01028-7

Środoń, J., & Eberl, D. D. (1984). Illite. *Reviews in Mineralogy and Geochemistry*, *13*(1), 495–544.

Stearns, R. G. (1957). Cretaceous, Paleocene, and Lower Eocene Geologic History of the Northern Mississippi Embayment. *Geological Society of America Bulletin*, *68*, 1077–1100.

Stein, C. A., Stein, S., Gallahue, M. M., & Elling, R. P. (2022). Revisiting hotspots and continental breakup—Updating the classical three-arm model. In G. R. Foulger, L. C. Hamilton, D. M. Jurdy, C. A. Stein, K. A. Howard, & S. Stein (Eds.), *In the Footsteps of Warren B. Hamilton: New Ideas in Earth Science*. Geological Society of America. https://doi.org/10.1130/2021.2553(05)

Swallow, E. J., Wilson, C. J. N., Charlier, B. L. A., & Gamble, J. A. (2019). The Huckleberry Ridge Tuff, Yellowstone: Evacuation of multiple magmatic systems in a complex episodic eruption. *Journal of Petrology, 60*(7), 1371–1426. https://doi.org/10.1093/petrology/egz034

Szmytkiewicz, A., & Zalewska, T. (2014). Sediment deposition and accumulation rates determined by sediment trap and 210Pb isotope methods in the Outer Puck Bay (Baltic Sea). *Oceanologia*, *56*(1), 85–106. https://doi.org/10.5697/oc.56-1.085

Thompson Jobe, J. A., Gold, R. D., Briggs, R. W., Williams, R. A., Stephenson, W. J., Delano, J. E., Shah, A., & Minsley, B. (2020). Evidence for Late Quaternary Deformation Along Crowleys Ridge, New Madrid Seismic Zone. *Tectonics*, *39*(4). https://doi.org/10.1029/2019TC005746

Uzarowicz, Ł., Šegvic, B., Michalik, M., & Bylina, P. (2012). The effect of hydrochemical conditions and pH of the environment on phyllosilicate transformations in the weathering zone of pyrite-bearing schists in Wieściszowice (SW Poland). *Clay Minerals*, *47*(4), 401–417. https://doi.org/10.1180/claymin.2012.047.4.01

Van Arsdale, R. (2009). *Adventures Through Deep Time: The Central Mississippi River Valley and Its Earthquakes*. Geological Society of America. https://doi.org/10.1130/SPE455

Van Arsdale, R. B., Williams, R. A., Schweig, E. S., Shedlock, K. M., Odum, J. K., & King, K. W. (1995). The origin of Crowley's Ridge, northeastern Arkansas: Erosional remnant or tectonic uplift? *Bulletin of the Seismological Society of America*, *85*(4), 963–985. https://doi.org/10.1785/BSSA0850040963

Van Arsdale, R., Bresnahan, R., McCallister, N., & Waldron, B. (2007). Upland Complex of the central Mississippi River valley: Its origin, denudation, and possible role in reactivation of the New Madrid seismic zone. In S. Stein & S. Mazzotti, *Continental Intraplate Earthquakes: Science, Hazard, and Policy Issues*. Geological Society of America. https://doi.org/10.1130/2007.2425(13)

Walker, R. (1976). Facies model-3. Sandy fluvial systems. *Geoscience Canada*, *3*(2), 101–109.

Watts, K. E., Bindeman, I. N., & Schmitt, A. K. (2012). Crystal scale anatomy of a dying supervolcano: An isotope and geochronology study of individual phenocrysts from voluminous rhyolites of the Yellowstone caldera. *Contributions to Mineralogy and Petrology*, *164*(1), 45–67. https://doi.org/10.1007/s00410-012-0724-x

West, L. T., Rutledge, E. M., & Barber, D. M. (1980). Sources and Properties of Loess Deposits on Crowley's Ridge in Arkansas. *Soil Science Society of America Journal*, *44*(2), 353–358. https://doi.org/10.2136/sssaj1980.03615995004400020029x

Whitney, D. L., & Evans, B. W. (2010). Abbreviations for names of rock-forming minerals. *American Mineralogist*, *95*(1), 185–187. https://doi.org/10.2138/am.2010.3371

Wilbert, L. J. (1953). *The Jacksonian Stage in Southeastern Arkansas*. Arkansas Resources and Development Commission, Division of Geology. https://books.google.com/books?id=5NPmFwqnZcMC

Wolff, J. A., & Gardner, J. N. (1995). Is the Valles caldera entering a new cycle of activity? *Geology*, *23*(5), 411. https://doi.org/10.1130/0091-7613(1995)023<0411:ITVCEA>2.3.CO;2

Zanoni, G., Šegvić, B., & Moscariello, A. (2016). Clay mineral diagenesis in Cretaceous clastic reservoirs from West African passive margins (the South Gabon Basin) and its impact on regional geology and basin evolution history. *Applied Clay Science*, *134*, 186–209. https://doi.org/10.1016/j.clay.2016.09.032

Zwoliński, Z. (1992). Sedimentology and geomorphology of overbank flows on meandering river floodplains. *Geomorphology*, *4*(6), 367–379. https://doi.org/10.1016/0169-555X(92)90032-J

Appendices

Table of Eastern outcrop SEM-EDS analysis

An.	Type	SiO_2	Al_2O_3	FeO	MgO	K2O	NaO	MnO	CaO	TiO_2	NiO	CeO_2	Y2O3	PbO	BaO	ZrO2	NO2	SnO
3	Kln	52.8	34.2	7.9	1.1	4.1												
4	**Kln**	54.5	42	2.9	0.5													
5	Kln	49.3	36.2	9.9	1	3.5												
6	**Kln**	53.2	44.3	2	0.5													
7	Kln	52.9	35.4	9.6	1.3	0.8												
9	Kln	49.2	34.7	12.1	0.8	2.6			0.6									
10	Kln	51.5	34.1	11.5	1.1	1			0.7									
11	Kln	47.2	35.4	14.9	1.1	1			0.5									
12	**Mmt**	55	27.7	15.9	0.7	0.7												
15	Kln	55.7	39	4.5	0.8													
16	Kln	52.5	39.6	5.6	0.7	1.6												
17	**Kln**	57.9	39.2															
18	Kln	48.1	32.7	16.6	1	0.7			0.9									
20	kln	48.7	32.2	17.6	1.5													
23	**Kln**	48.7	48.3	3														
25	**Kln**	55.3	44.7															
26	Kln	52.7	39.1	8.1														
28	**Kln**	55.7	38.3	3.2		2.9												
29	Kln	46.3	30.7	20.3	1.3	0.9			0.5									
30	Kln	53.2	33.6	11.1	0.8	1.2												
31	Kln	46.7	30	20.7	1.4	1.2												
32	Kln	47.2	30.2	19.6	1.4	1			0.7									

33	Kln	51.9	32.5	12.2	1.4	1.3			0.6								
36	Kln	51.4	33.9	14.7													
37	**Kln**	55.3	44.7														
38	**Kln**	55.3	44.7														
39	**Kln**	52.8	43	4.2													
40	**Kln**	55.3	44.8	1.9													
41	Kln	51.7	39.8	7.5	1.1												
42	Kln	52.6	33.5	10.1	1.1	0.5			0.8	1.4							
43	Kln	49.9	31.3	15.5	1.2				0.8	1.2							
44	**Kln**	53.8	41.5	3.3	1.4												
45	**Kln**	53.4	41.6	3.7	1.3												
46	**Mmt**	53.6	31	11.2	1.4				1	1.9							
47	Kln	49	44	6.5													
48	**glass**	90.6	9.4														
49	**Kln**	54.2	40.9	4.3	0.6												
50	**Kln**	56	42.2	1.8													
51	**Kln**	56.4	42.1		1.5												
52	**Kln**	56.8	43.2														
53	**Kln**	56	44														
54	**Kln**	52.7	44.9	2.4													
55	**glass**	78.5	12	9	0.5												
56	**Kln**	58.4	41.6														
57	**glass**	78	12.5	9	0.6												
61	Mix	12.7	8.3	9.2	0.4					1.8						44.6	23
62	Kln	53	41.8	5.3													
63	**Kln**	56.5	43.5														
64	Kln	49.1	37.2	12.6	0.6	0.5											
65	Kln	49.8	35.2	10.8	0.7											3.5	
66	**Kln**	55.3	44.7														
75	Kln	54.2	41.1	4.7													
76	**Kln**	59.6	40.4														

77	**i-s**	54.9	20.3	18.5	3.8	1.3			1.2	
78	**i-s**	52.5	25.6	17	2.3	2.5				
80	Kln	53.4	37.9	8.1	0.6					
81	**Mmt**	59.3	26.5	9.9	3				1.3	
82	Kln	55.2	37.5		1	4.3	2			
83	Kln	49.5	32.4	7.7	1.5	8.9				
84	**i-s**	51.7	19.6	20.9	3.6	1.8			0.5	1.5
85	**i-s**	53.5	22.4	16.7	3.4	2.5			0.8	0.7
87	**i-s**	53.5	19.5	19.4	3.6	1.7			0.9	1.3
89	**i-s**	52.3	19.3	21.3	3.4	1.5				
90	**i-s**	53.7	26.2	15.2	2.2	1.6				
91	**glass**	96.2	3.8							
92	**glass-mmt**	81.3	15.5			2.4				
93	**glass**	97.5	2.5							
94	**glass-mmt**	83.8	9.9	4.7						
100	Kln	50.1	33.3	5.6	1.7	9				
104	Ill	60.6	23.2	5.7	0.9	9.8				
105	**San**	64.7	19			15	0.3			
107	**Ill**	63.9	24.1		0.7	11.3				
108	**San**	65.3	19.4	1.8	0.3	13.2				
109	**San**	65.5	20.7			13.9				
113	**San**	54.1	26.5	1.2	1.4	16.8				
114	Ms	48.7	39.9			10.7	0.7			
117	**Kln**	55.7	44.3							
119	**i-s**	56.9	22.1	15.9	3	1.2			1	
121	**i-s**	66.4	21.5	5.1	1.4	5.6				
122	**glass**	96.7	2.4			0.9				
123	**glass**	63.3	6.6	30						
124	**glass**	86.4	7.5	4.2	0.6	1.3				

135	Mmt	60.6	17.4	17.4	2.6	1			1.1									
136	**Ms**	49.4	39.5		0.7	9	1.4											
137	**Ms**	51.2	38.5			9.1	1.2											
138	**Mmt**	65.6	16.4	14.4	1.9	1			0.7									
140	**i-s**	66.7	21.1	5.5	1.9	3.1			1.6									
141	**Mmt**	70.2	17.8	7.3	1.7	2.1			0.7									
158	**Ill**	55.9	29	6.6	2.9	5.7												
159	**i-s**	53.4	19.9	20.7	3.2	1.2			1.3									
162	**i-s**	51.7	23.7	18.7	2.4	2.3			1.2									
164	**glass**	95.5	3.8			0.6												
166	**glass**	84.3	9	4	1.3	1.4												
167	**Kln**	57.7	42.3															
168	**Mmt**	63	33.6		2.4		1											
169	**Mmt**	61.9	32.8		2.3	1.4			1.7									
170	**Na-Sanidine**	62.9	20			11.2	2.9								3.1			
171	**Na-Sanidine**	63.1	19.9			11.2	2.9								3			
174	**i-s**	58.1	27.5	12.3	1	1												
176	i-s	53.3	34.4	9.9	0.8	1.6												
179	Kln	46.6	32.2	19	1.1	1.1												
181	Kln	49.7	34.2	14.7	1.5													
184	**San**	63.4	20.9			15.6												
186	**San**	60.6	20.6			18	0.8											
187	**San**	63.1	19.3			17.6												
188	**Kln**	62.2	37.8															
192	Kln	52.3	32.9	10.7	1	1.7			1.4									
195	*Ilm*	7	3.9	68.1	2.5					68.1								
196	*Ilm*	5.2	2.2	3.4	0.3					88.8								
197	*Cas*	2.7	1											2.5				93.8
200	Kln	51.7	39.7	8.1	0.5													

201	**San**																	
203	**Kln**	**55.7**	**44.3**															
204	Ilm	10.3	7.5	15.6	0.7					48.2							16.8	
205	Kln	52.8	28	13.6	0.8	4.9												
206	*Cas*	3.7	1.4											3.4				91.5
207	*Ilm*	2	1.3	4.1	0.7					91.9								
210	Kln	44.7	29.9	22.6	1.3	1.1			0.4									
211	Kln	35.6	24.4															
214	Kln	53.2	42.3	4.5														
215	**glass-Mmt**	78.6	19.1			2.3												
217	**San**	65	19.1			15.4			0.5									
219	**glass-Mmt**	86.4	13.6															
220	Kln	50.4	31	15.7	1.2	1.1			0.6									
221	Mmt	66.9	19.1	*12.6*	0.8				0.7									
223	Kln	47.5	30.6	19.6	1	1.3												
224	**Mmt**	69.8	20.8	7.8	0.8	0.7												
227	Kln	51	34.2	13.8	1													
228	San	64.7	20.3			14.3	0.6											
229	San	64.9	20.3			14.2	0.5											
230	leucite	55.2	17.8			27												
231	San	65.2	18.9			15.9												
234	leucite	59.7	17			21												
236	i-s	55.2	23	13.8	0.5	6.8	0.6											
237	Kln	47.5	35.1	16	0.6	0.6												
238	Kln	48.4	33.8	16.6	1.2													
241	leucite	62.5	17.7			19.4	0.4											
243	Mmt	54.3	24.2	21.5														
245	**Kln**	55.6	44.4															
246	Kln	53.6	34.7	10.9	0.9													

247	**Kln**	56.2	43.8							
249	Kln	50.6	34.2	13.1	1	1.1				
251	Ill	56.4	33.4	8.9						
252	**Kln**	58.4	41.6							
254	**Kln**	54.5	45.5							
256	San	48.3	35.9	2.1	0.9	12.8				
258	i-s	52.8	28.8	12.1	4	2.2				
260	San	51.7	34.7		1	12.6				
261	i-s	67.5	17.2	10.9	1.4	3				
263	i-s	48.3	16.8	16.2	2.9				1.2	14.7
265	Kln	76.2	16.4	7.4						
266	Kln	58.4	40.4			1.1				
268	i-s	51.9	25.1	16.4	2.3	4.3				
269	Kln	54.5	44.4			1				
270	i-s	43.8	24.3	28.7	1.9	0.7			0.5	
271	Mmt	64.5	18.4	15.5	0.6	0.6			0.4	
272	Kln	50.1	38.9	11						
273	i-s	48.7	32	17.2	1.3	0.8				
275	glass-mmt	78.3	11.5	7.2	1.5	1.5				
276	i-s	46.5	28	22.4	1.4	1.1			0.6	
277	i-s	52.4	28.7	15.2	1.5	1.4			0.8	
278	i-s	37.7	25.2	34.6	0.9	0.9			0.7	
279	i-s	56.5	27.9	14.3	1.3					
281	Kln	54.8	39.7	5.5						
283	i-s	47.5	26.4	13.5	2.8	9.8				
286	Mmt	60.4	31.8	3.1		4.6				
287	i-s	40.5	26.9	31.4	1.3					
288	i-s	47.4	30.2	19.5	1.7	1.3				
289	i-s	51.4	34	13.4	1.3					
290	i-s	50.9	39.2	5.4	1.1	3.3				

291	i-s	53.1	31.8	13.8	1.3					
292	i-s	55.5	37.5	5.1	0.9	1				
294	San	65.3	19.5			14.6	0.6			
295	Kln	91.5	3.2	5.3						
296	Kln	55.3	35.8	6.9		2				
297	i-s	54	31.9	11	0.6	2.5				
298	i-s	52.6	36.5	9.3	0.9	0.7				
299	GL	80.2	11.1	7.5	0.5	0.3			0.3	
300	i-s	50.8	31.4	15	1.5	0.7			0.5	
301	i-s	52.9	27.7	12.1	2.1	2.3			0.7	2.1
303	Ill	49.2	34.7	9.4	1.1	5.6				
304	i-s	58.5	13.1	27.7	0.7	0.7				
305	Mmt	79.2	13.2	7.2	0.4					
314	Mmt	74.8	10.8	13.6	0.9					
315	Mmt	49.1	36	7.6	0.9	6.4				
319	San	64.8	20.7			14.2	0.3			
320	glass?	86.6	7.7	5.5		0.3				
321	Kln	54.3	43.6			2.1				
322	Kln	56.5	43.5							
324	Kln	59.3	40.7							
327	Kln	56.1	43.9							
328	Kln	60.1	39.9							
331	Kln	54.3	44.6			1.1				
333	Mmt	50.8	34.3	8.8	1.1	4.9				
334	i-s	50.2	36.4	9.1	3.4	0.9				
335	i-s	48.6	32.4	17.8	0.7	0.5				
336	i-s	51.4	39.2	8.4	0.7	0.4				
337	i-s	51.2	33.4	12.8	1	0.8				
338	i-s	51.9	37	10.3	0.8					
339	San	55.5	42.1			2.4				
340	i-s	50.7	38.4	7.9	0.7	2.3				

342	Kln	53.7	45.4			0.9
344	Kln	53.8	46.2			
345	Kln	54.3	45.7			
346	Kln	50	42.7	7.3		
347	Kln	55.5	44.5			
348	Kln	55	45			
349	Kln	43.8	31.4	24.7		

EDS phase chemistry analysis from the western outcrop

An.	Type	SiO2	Al2O3	FeO	MgO	K2O	NaO	MnO	CaO	TiO2	NiO	CeO2	Y2O3	PbO	BaO	ZrO2	NO2	SnO
4	Sme	54.3	20.8	18.7	2.9	2.2			1.1									
5	Sme	59	25.8	10.2	2.3	1.8			1									
7	Sme	51	20.3	24.6	1.7	1.4			1.1									
8	Sme	58.4	24.7	11.3	2.5	1.7			1.3									
9	Sme	56.6	26.8	10.3	2.2	2.8	0.3		1.1									
10	Sme	52.5	32.1	5.8	1.9	7.4	0.3											
11	Sme	51.2	29.3	7.2	3.6	8.8												
19	Sme	56.5	26.3	11.6	2.6	1.9			1.1									
20	Sme	66.4	29	1.4	1.3	1.2			0.7									
21	Sme	56.9	23.4	13.1	2.9	1.3			1.2	1.3								
22	Sme	63.1	22.7	7	3.6	1.9			1.8									
23	Sme	56	23.4	16.9	2.5	0.5			0.8									
24	Ms	50.3	40.4		0.3	8	0.9											
27	Kln	49.8	39.6		0.5	9.2	0.9											
28	Sme	49	27.3	15.3	2.4	6												
30	Sme	55.4	25.4	14.8	2.7	1.7												
31	Sme	55.4	25.9	13.5	2.7	1.7	0.8											
32	Chl?	43.7	18.6	29.9	6.7	1.1												
33	Sme	54.6	26.4	12.2	2.7	2.5			0.9	0.6								
34	Sme	57.9	24	13.5	2.3	1.6			0.8									

35	Ms ?	52.4	42.1	4						
36	i-s	57.5	27.9	7.6	2.7	4.3				
37	**Kln**	55.9	44.1							
39	Sme	58.6	28.1	8.5	1.9	1.8	0.2		0.9	
40	Chl?	44.1	18.9	28.8	6.5	1.6				
41	Kln	53.8	42.8	2.6	0.3	0.5				
42	Kln ?	55.9	43.5			0.6				
43	Kln ?	56.3	43.7							
44	Kln ?	55.5	44.5							
50	Sme	53.6	28.8	13.5	1.6	1.9			0.6	
51	GL	87.7	11.8			0.5				
53	Sme	89.3	8.8		0.6	1.3				
54	**Kln**	56.3	43.7							
55	Sme	46.8	20.4	25.1	5.8	1.4			0.6	
58	GL	89.4	10		0.4					
59	Sme	56.3	34	4.7	1.4	3.6				
63	glass	90.4	8.6		0.9					
66	**Kln**	56.4	43.6							
84	Sme	56.3	25.8	11.5	2.7	1.4	0.4		0.7	1.2
85	**Sme**	66.4	12.5	5.1	16					
86	Sme	64.4	23.3	5.7	5.1	0.7			0.7	
87	Sme	65.2	22.7	5.5	5.7		0.2		0.7	
89	**kln**	53	42	5						
90	**Sme**	52	23.3	19.5	3.3	2				
92	**Sme**	46.2	20.9	22.1	7.1	3.6				
93	**Sme**	54.5	28.1	12	2	2.8	0.5			
94	**Sme**	57.1	35.5	1.6		5.7				
95	Kln ?	56.5	41.4		0.9	1.1				
108	San	66.1	19.5			13.9	0.5			
109	San	65.7	18.5			14.8	1.1			
110	San	65.8	18.9			15.3				

111	San	65.4	19			15	0.6				
112	San	65.4	18.5			13.6	1.1			1.5	
114	Sme	67.4	21.3	7	2.5	1.9					
115	Sme	57.5	26.7	14.2	1.6						
116	Sme	65.8	27.9		3.7	2.5					
120	**Sme**	30.6	11.7	23.8	4.6	4.5			1.2		23.5
123	**Sme**	46.3	29.2	13.6	2.2	8.8					
124	Sme	49.9	21.7	3.9	20.7	3.5	0.3				
125	Sme	79.9	2		4		8	6.1			
126	**Sme**	55.9	22.9	17.2	2.5	1.5					
129	**Sme**	49.1	21.2	21.9	5.7	2.2					
130	**Sme**	53	23.4	18.8	2.5	1.1	0.3	0.8			
131	**Sme**	56.1	23.5	13.5	3.9	3					
134	**Sme**	56.6	27.3	11.5	2.4	1.9	0.4				
135	**Sme**	48.6	29.1	12	1.7	7.4			1.2		
136	**Sme**	56.3	34.6		1.8	7.3					
137	Kln ?	59.2	26.3	12.4	2						
138	Sme	52.9	25.4	12.6	3.6	5.5					
139	**Sme**	59.7	24.7	10.8	2.6	1.5		0.8			
140	**Sme**	57.7	28.2	8.6	2.2	3.2					
141	**Kln**	67.7	28.8	3.5							
142	**Sme**	59	25	11.7	2.2	2.1					
143	**Sme**	55.9	36.4	6.3	1.4						
144	**Kln**	55.9	44.1								
165	Albite	68.2	18.7			7.3	5.7				
166	Albite	68	19.1			6.6	6.3				

Vitae

Trevor J. Dempsey was born in Fayetteville, North Carolina and raised in Columbus, Georgia. Trevor graduated from Georgia Southwestern State University in 2018 with a Batchelor of Science in Geology. After some time away from academia he returned to the field to pursue a Master's of Science in Engineering with an emphasis in Geology at the University of Mississippi where he was a Teaching Assistant for hist first three semesters and Research Assistant for his final semester. Trevor was advised by Dr. Branimir Šegvić from Texas Tech University and Dr. Ron Counts from the Mississippi Mineral Resource Institute.

While at the University of Mississippi Trevor was awarded two grants, one from the Clay Mineral Society and the second from the Society for Sedimentary Geology. Trevor is graduating in August of 2022 with a Master's of Science. After graduation Trevor will begin pursuing his PhD at Northwestern University.